Energy simulation and experimental evaluation of the dynamic properties of a hydraulic rubber bellow

A Labuschagne

orcid.org/ 0009-0005-4840-6936

Dissertation accepted in fulfilment of the requirements for the degree *Master of Engineering in Mechanical Engineering* at the North-West University

Supervisor: Dr JH Kruger
Co-supervisor: Mrs MM van Niekerk

Graduation: May 2026

Abstract

In many industrial systems, a bellow is necessary to minimise the amplitude and/or forces on the structures that are transferred by vibrations. This study focusses on the application of an in-line rubber bellow and how the change in operating conditions affects the dynamic properties. The vibration and fluid energy are also simulated to understand the energy that is transferred to the fluid of the system and not absorbed by the bellow.

Mathematical models were constructed and implemented. These models were used to characterise and evaluate the dynamic properties of an in-line rubber bellow system. The vibration energy and power were evaluated along with the amount of vibration energy that was transferred to the fluid in the system. A single degree-of-freedom mathematical model was implemented and numerically calculated to predict the transient behaviour of the bellow; these predicted calculations were compared to experimental results.

The input values of the numerical model were characterised, where the phase angle of the system was calibrated for a damping-free condition. The acceleration and excitation force of the system were also measured and used as part of the input parameters for the numerical model. This characterisation process was conducted at multiple frequencies between 2.5 Hz and 25 Hz, pressures between -30 kPa and 50 kPa, and excitation forces ranging from 50% to 100% of the unbalance motors' capacity.

The experimental results were evaluated and discussed, where the change in dynamic properties of the system was compared to the change in amplitude, frequency, and pressure difference, respectively. Although the change in stiffness was not definable, the dependence of the damping in the system with respect to the change in amplitude and frequency was significant and evaluated to aid future design selection for the application of in-line rubber bellows. The damping ratio at lower amplitudes (<5 mm) was lower. (<30%) than at higher amplitudes (6-9 mm). The damping ratio also decreased with the increase in frequency. If the operating design criteria are known in

terms of amplitude or operating frequency, the damping ratio of the system can be predicted by using the results in the table below.

Known design criteria	Damping-ratio expectation	Notes
Amplitude <5 mm	0-30%	See frequency dependence
Amplitude 6-9 mm	30-80%	See frequency dependence
Operating frequency	$y = 1.765x^{-1.035}$	y (Damping ratio) x (Frequency [Hz])

The vibration energy was simulated to determine where the vibration energy will be dissipated. Here, the amount of vibration energy transferred to the fluid in the system was also determined, where up to 72% of the vibration energy was transferred to the fluid in certain conditions. The evaluation of the energy transferred to the fluid was significant to understand what effect the vibrations will have on the internal fluid, depending on the system design this could have a positive or negative effect on the system.

Keywords: Rubber bellow, dynamic properties, vibration, characterisation, energy, transient behaviour.

Declaration

I, Abraham Labuschagne, hereby declare that the material used in this study is my own original work, except where specifically referred to by name or in the form of a reference. This work has not been submitted to any other university.

Abraham Labuschagne
Student number:
Identity number:

Acknowledgements

- God almighty, without him none of this would have been possible.
- My wonderful wife Charné for continuously supporting me and encouraging me every step of the way.
- My friends and co-students, J. Bloem, LP. Pretorius and B. Meiring.
- The engineering workshop at the university that assisted in the fabrication of components of my test bench and gave me valuable information.
- All the engineering faculty lecturers who are always willing to give constructive advice and the necessary equipment to complete any experimental setup.
- Dr. CB Nel, whose experience and knowledge played an important factor in the success of this dissertation.
- Prof. Wichers, Prof. Van Eldik, Prof. Den Heijer, and Prof. Coetzee for ensuring the continuity of the study.
- Dr. Kruger and Marné Van Niekerk who has guided my dissertation to submission and willingly took over supervision for the study.

Table of Contents

List of Tables

List of Figures

Nomenclature

Capital letters

A	Area	m^2
A_1	Area of pipe segment 1	m^2
A_2	Area of pipe segment 2	m^2
A_p	Equivalent piston area	m^2
C	Sine function mean	-
D	Diameter	m
D_1	Diameter of pipe segment 1	m
D_2	Diameter of pipe segment 2	m
D_p	Equivalent piston diameter	m
ΔV	Change in volume per cycle	m^3
ΔW_{v}	Work done in one cycle	J
F_e	Excitation force	N
$\mathrm{F_e}$	Excitation force amplitude	N
F_{m_c}	Damper force	N
F_{m_k}	Spring force	N
F_{m_m}	Mass force	N
F_u	Unbalanced motor force	N
L	Applied load	kg
P	Pressure	kPa
P_A	Inlet pressure gauge	kPa
P_B	Internal pressure of bellow	kPa
P_{c_1}	Pressure before one-way valve	Pa

P_{c_2}	Pressure after one-way valve	Pa
P_D	Discharge pressure gauge	kPa
$\mathbb{P}$	Power delivered	W
$\mathbb{P}_E$	Electrical power	W
$\mathbb{P}_{f_1}$	Frictional power loss in pipe segment 1	W
$\mathbb{P}_{f_2}$	Frictional power loss in pipe segment 2	W
$\mathbb{P}_h$	Hydraulic fluid power	W
$\mathbb{P}_{\mathrm{v}}$	Vibration power delivered	W
$\mathbb{P}_{\mathrm{v}_c}$	Vibration power delivered to damper	W
$\mathbb{P}_{\mathrm{v}_\mathrm{k}}$	Power dissipated by the spring	W
$\mathbb{P}_{\mathrm{v}_m}$	Vibration power delivered to mass	W
$\mathbb{P}_{\mathrm{v}_\mathrm{max}}$	Maximum vibration power delivered	W
Q	Flow rate	m^3/s
Q_{max}	Maximum flow rate	m^3/s
Re	Reynolds number	-
Re_1	Reynolds number in pipe segment 1	-
Re_2	Reynolds number in pipe segment 2	-
$S0$	Signal output	V
SP	Signal amplitude	V
W	Work done	J
X	Displacement amplitude	m
$\dot{X}$	Velocity amplitude	m/s
$\ddot{X}$	Acceleration amplitude	$\mathrm{m/s}^2$
Z	Sine function amplitude	-

Lowercase letters

a_1	Fluid acceleration in pipe segment 1	m/s^2
a_2	Fluid acceleration in pipe segment 2	m/s^2
c_c	Critical viscous damping of the bellow	Ns/m
c_m	Bellow damping coefficient	Ns/m
f	Frequency	Hz
f	Friction factor	–
f_1	Friction factor of pipe segment 1	–
f_2	Friction factor of pipe segment 2	–
f_n	Natural frequency	Hz
g	Gravitational acceleration	m/s^2
h_0	Height of the water level of the inlet tank	m
h_A	Height at point A	m
h_B	Height at point B	m
h_C	Height at point C	m
h_D	Height at point D	m
h_{f_1}	Friction head of pipe segment 1	m
h_{f_2}	Friction head of pipe segment 2	m
h_{i1}	Inertia head of pipe segment 1	m
h_{i2}	Inertia head of pipe segment 2	m
h_{in}	Internal pressure head of the bellow	m
h_L	Total head loss of bellow system	m
h_m	Head gain of bellow system	m
h_v	Head loss due to one-way valve	m

k_m	Stiffness of bellow setup	N/m
k_r	Stiffness of rubber bellow	N/m
k_s	Stiffness of steel Springs	N/m
l	Length	m
l_1	Length of pipe segment 1	m
l_2	Length of pipe segment 2	m
m_e	Equivalent unbalance mass	kg
m_m	Equivalent mass on bellow	kg
n	Unbalanced mass percentage	%
r_e	Unbalance radius of gyration	m
t	Time	s
v	Velocity	m/s
v_1	Velocity in pipe segment 1	m/s
$\mathrm{v}_{1_{max}}$	Maximum fluid velocity in pipe segment 1	m/s
v_2	Velocity in pipe segment 2	m/s
$\mathrm{v}_{2_{max}}$	Maximum fluid velocity in pipe segment 2	m/s
x	Displacement of bellow system	m
$\dot{x}$	Velocity of bellow system	m/s
$\ddot{x}$	Acceleration of bellow system	m/s^2
y	Sine/cosine function	-

Greek symbols

$\Delta\phi$	Measured phase angle	rad
ΔW_v	Vibration work in one cycle	J/rev
ϵ	Roughness of the pipe	mm
η_H	Hydraulic efficiency	-
η_m	Fluid energy transfer ratio	-
η_V	Volumetric efficiency	-
μ	Dynamic viscosity	Ns/m^2
ω	Forced frequency	rad/s
ω_n	Natural frequency of bellow system	rad/s
ϕ	Phase angle	rad
ϕ_{eik}	Calibrated phase angle	rad
ρ	Density of water	kg/m^3
ζ	Damping ratio of the bellow system	-

Abbreviations

ATM	Atmospheric
DI	Diagnostic Instrument
DMA	Dynamic Mechanical Analysis
EC	Eddy Current
FFT	Fast Fourier Transform
HEM	Hydraulic Engine Mount
PV	Pressure-Volume
RMSE	Root Mean Squared Error
SSE	Sum of Squared due to Error
VSD	Variable Speed Drive

1 Introduction and Problem Statement

1.1 Introduction

Rubber bellows are widely used in various engineering applications, allowing thermal expansion or movement and isolating vibrations in applications where dynamic forces are induced. Some of the industries where rubber bellows are widely used include automotive, aerospace, manufacturing, and robotics. Understanding their dynamic properties is essential for optimising their performance and ensuring the reliability and longevity of the systems into which they are integrated. Flanged in-line rubber bellows, as illustrated in Figure 1-1 below, are commonly used in fluid pumping systems.

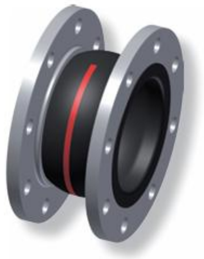

Figure 1-1: Rubber bellow example (Willbrandt-Cummitechnik, n.d.)

An installation of a in-line bellow application is shown in Figure 1-2, that is used to minimise the vibrations transferred from the pump to the discharge piping.

Figure 1-2: In-line rubber bellow application example (ChangYuanFlex, n.d.)

The process of selecting the correct rubber bellow focusses primarily on the material being transported, the temperature, and pressure of the system, as outlined in Appendix A. In-line rubber bellows are usually also subjected to dynamic forces and vibrations. Under these conditions, the bellows must withstand and respond effectively to varying levels of mechanical stress and oscillations. Failure to adequately understand their dynamic behaviour can lead to premature wear, decreased operational efficiency, and potentially catastrophic system failures. Rubber bellows also play a vital role in mitigating the transmission of vibrations and noise within piping systems. By dampening vibrations, bellows help to maintain system stability and reduce noise levels. However, achieving optimal vibration isolation requires a thorough understanding of the bellows' dynamic characteristics, such as stiffness and damping properties, to determine the critical frequencies.

This dissertation aims to better understand the change in dynamic properties of an in-line rubber bellow used in a fluid pumping system under different operating conditions. Understanding the change in dynamic properties of an in-line rubber bellow in this application could assist in recommendations on how to choose the most efficient rubber bellow based on the expected operating conditions in a similar setup.

1.2 Background

In-line rubber bellows are integral components that are used in engineering systems for their ability to mitigate vibrations, offering damping and flexibility to absorb dynamic forces. When installed for vibration reduction purposes, specific criteria must be considered to optimise their dynamic properties, including damping and stiffness, to achieve effective vibration isolation. Vibration isolation is the technique used to reduce unwanted vibrations that results in a reduction in transmitted forces or suppresses the displacement of a device (Yang, 2005).

Critical criteria in the installation of in-line rubber bellows for vibration reduction are the selection of appropriate bellows stiffness and damping characteristics. Stiffness refers to the bellows' resistance to deformation under applied loads, while damping refers to their ability to dissipate energy. Balancing these properties is essential to ensure effective vibration isolation without inducing excessive stiffness or compromising damping capacity. The most suitable rubber bellow should therefore be soft enough to reduce transmitted forces and hard enough to limit the relative displacement, as the process followed during the selection of a hydraulic engine mount (Marzbani et al., 2014).

Consideration must also be given to the operational conditions and environmental factors that may influence the dynamic properties of an in-line rubber bellow installation. Temperature variations, exposure to fluids, and pressure can affect the dynamic properties of the bellows, necessitating appropriate bellow selection (Sjöberg , 2002). However, in general, the datasheet of a typical rubber bellow only states the static properties of the bellow and does not mention the damping coefficient of the bellow.

In order to illustrate this, a section of a rubber bellow specification sheet is shown in Figure 1-3 below, the full specification sheet can be seen in Appendix A. In the specification sheet, no damping properties are provided, along with an indication that these properties can differ by up to 25% under different operating conditions.

WILLBRANDT **Rubber Expansion Joint Type 50**

Axial stiffness rates

DN	Overall length	Stiffness rates (averages value from full way)					
	BL mm	0 bar Nm/mm	2,5 bar Nm/mm	4 bar Nm/mm	6 bar Nm/mm	10 bar Nm/mm	16 bar Nm/mm
20	130	31	68	128	192	243	270
25	130	31	68	128	192	243	270
32	130	31	68	128	192	243	270
40	130	30	66	124	186	236	261
50	130	25	51	98	134	173	192
65	130	24	53	100	150	190	211
80	130	28	58	104	148	185	205
100	130	35	71	116	206	274	304
125	130	36	71	137	214	282	313
150	130	49	102	189	293	390	433
200	130	100	180	365	568	735	816
250	130	105	207	388	609	778	864
300	130	123	248	448	658	883	980
350	200	105	177	349	567	753	836
400	200	154	261	516	535	1090	1210
450	200	167	320	581	903	1162	1290
500	200	196	376	686	1060	1364	1514
600	200	208	292	692	1123	1441	1600
700	*250	140	198	521	714	954	-
800	250	180	270	594	975	1258	-
900	300	200	380	690	1080	1395	-
1000	300	225	420	742	1248	1568	-

* Building length 260 mm

Warning: Deviations (+/- 25 %) in the stiffness rates may occur due to use of different materials and manufacturing processes.

Figure 1-3: Example of rubber bellow properties

The most effective way to determine the dynamic properties of flexible rubber connections is through experimental testing (Yang et al., 2020). In their experimental study to determine the effectiveness of flexible pipes (like in-line rubber bellows) in isolating unwanted vibrations, it was seen that pipes made of assorted rubber types, each offered distinct advantages across different frequency ranges. The dynamic properties (stiffness and damping) were found to be installation dependent and unique, therefore, complicating the bellow selection to achieve sufficient vibration isolation for all operating conditions.

1.3 Problem Statement

In many piping applications, in-line rubber bellows are used to isolate vibrations and accommodate dynamic movements. However, the dynamic properties of the rubber bellows vary with operating conditions such as pressure, frequency, and amplitude. These variations can cause changes in the behaviour of the bellows', potentially leading to the transmission of unwanted vibrations and forces to the piping and surrounding structures.

Currently, manufacturers typically provide rubber bellow specifications based on static conditions, which may not accurately represent their dynamic performance. This discrepancy poses a challenge in selecting the appropriate rubber bellow for applications with varying operating conditions.

Therefore, a critical need exists for an improved understanding of how changes in operational amplitude, frequency, and pressure affect the dynamic properties and vibration energy distribution of in-line rubber bellows under realistic operating ranges.

1.4 Aims and Objectives.

Using the Willbrand Type 50 SP as a representative case study of a typical rubber bellow used in piping systems, this research aims to:

- Understand how the dynamic properties of this specific rubber bellow change under varying operating conditions.
- Develop an improved selection criteria for its application based on these dynamic behaviours.

The insights gained from this study will support a more effective implementation of the Willbrand Type 50 SP bellow and provide guidance applicable to similar rubber bellows and compensators in piping systems with varying operating conditions.

The objectives that will help to achieve the aim of this study are the following:

- Conduct a literature review on the characteristics of rubber bellows and numerical modelling approaches for their dynamic properties and vibration energy.
- Develop a numerical model of the Willbrand Type 50 SP rubber bellow that incorporates its dynamic properties and varying operating conditions.
- Experimentally evaluate the in-line hydraulic rubber bellow's dynamic properties (stiffness and damping) across various frequencies, pressures, and amplitudes.
- Validate the numerical model through comparison with experimental measurements.
- Assess the accuracy of the numerical integration model by validating its predictive capability.
- Simulate the vibration energy and quantify the energy transferred to the fluid within the rubber bellow system.
- Propose a set of dynamic properties for the Willbrand Type 50 SP rubber bellow as a test case to demonstrate the characterisation process. Instrumentation

1.5 Research Methodology

The waterfall graph below illustrates the research methodology used for this study.

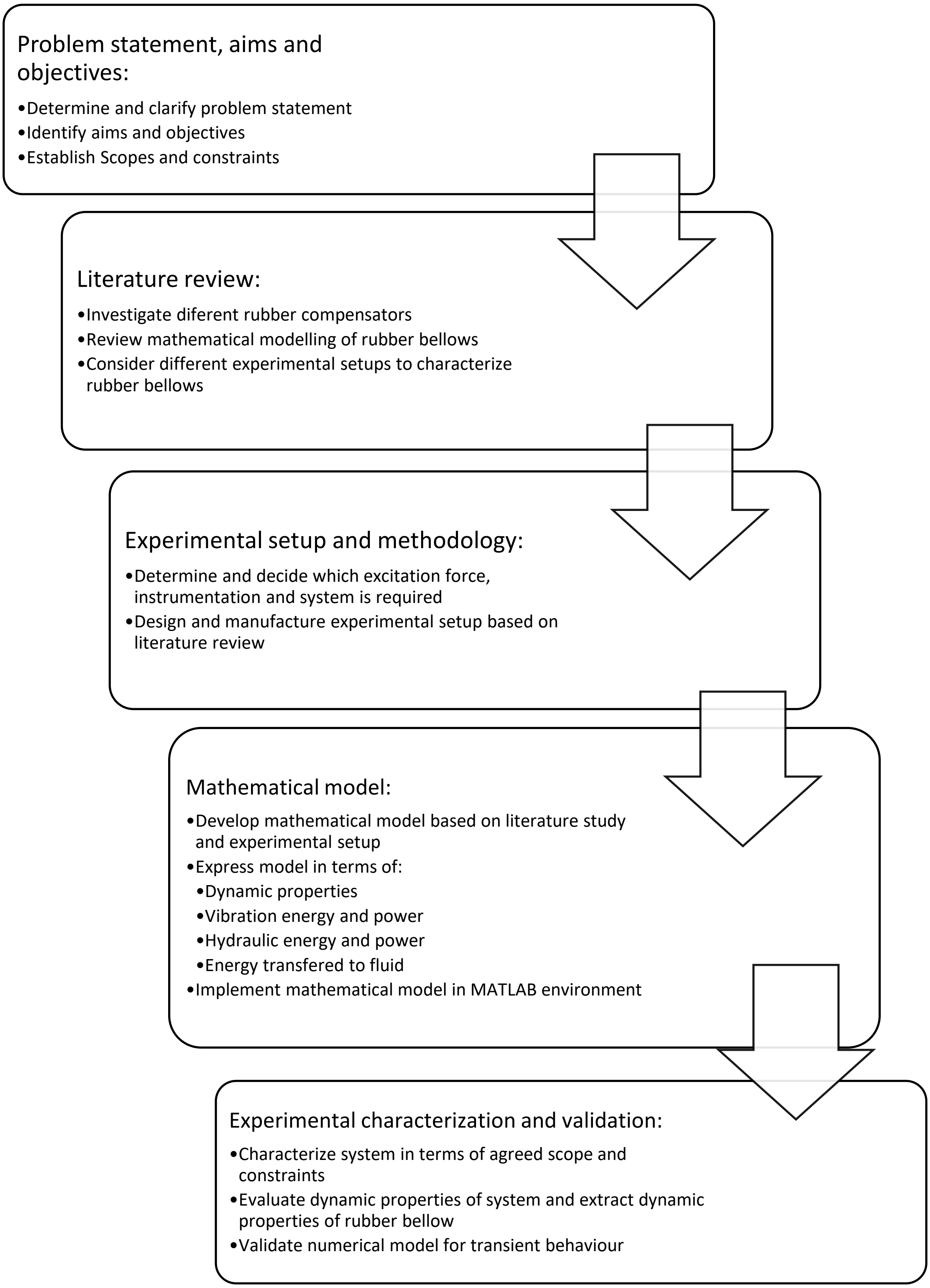

1.6 Scopes and Constraints

The experimental setup was chosen considering the practical constraints, the availability of resources, and the functional requirements of the study.

A Willbrand Type 50 SP bellow was selected as the core component of the experimental system. The decision was based on two primary considerations. Since the focus of the study is to study and evaluate the dynamic properties of the bellow, any fluid will suffice. Therefore, the choice was made to use water as the transport fluid. Since the faculty had a Willbrand Type 50 SP bellow available from a previous study, and the fact that the bellow is designed to operate with water and is a representative example of bellows used in piping systems, this bellow was an appropriate selection for the study.

The dynamic properties of the bellow needs to be determined by oscillating/vibrating the bellow in a controlled manner. Vertical vibrations were a critical element of the experimental procedure. To generate these vibrations, two identical unbalanced motors were used. The decision to use unbalanced motors over an electromagnetic shaker was driven by the fact that there was a concern that the weight of the setup would exceed the recommended capabilities of the available shaker. Unfortunately, the electrodynamic shaker available in the faculty was damaged during a previous study, and it was considered an unacceptable risk that a possible water leak could further damage the shaker. Due to budget constraints with respect to repair or replacement, it was therefore not a realistic option for the current study. The advantage of using unbalanced motors is that these motors are robust and simple to install and operate.

In Chapter 3 the chosen experimental setup is discussed further.

1.7 Chapter Layout

In Chapter 1 the introduction and problem study of the study is given. In this Chapter, the background of the use of rubber bellows and similar setups are explained, which leads to a problem statement that defines the aim and objectives of the study, whereafter the research methodology was defined. The scope and constraints of the study are described.

In Chapter 2, a review of the literature is given. The literature study begins with introducing different, applicable, rubber compensators that relate to the use of a rubber bellow. The applications of these compensators are explained and the advantages of these compensators are discussed. Hydraulic rubber mounts are discussed. With the focus of the study being on the rubber bellow, the rubber bellow is discussed along with some examples of the applications for which these bellows are used.

In Chapter 3 the experimental methodology was developed, starting with the mathematical modelling of rubber bellows. In this Chapter the mathematical modelling of the rubber bellow system was developed in terms of the equation of motion and the vibrational energy and power of the bellow system. To enable the mathematical modelling of the transient behaviour of the system, an iterative numerical calculating software had to be implemented, and the modelling thereof was discussed in this Chapter. Different evaluation methods for rubber bellows were discussed. After considering the different evaluation methods, the experimental setup was developed in terms of the type of excitation force inducer and the vibration instrumentation required. The rubber bellow system was developed and defined.

In Chapter 4 the mathematical models for the rubber bellow system are developed. The mathematical model to calculate the dynamic properties and response of the system was developed. The vibration energy and the power of the system were mathematically modelled along with the fluid energy to determine the portion of energy transferred from the mechanical elements of the system to the fluid.

In Chapter 5 the MATLAB scripts used to implement the mathematical models for this study are explained and illustrated. The process flow diagrams of the MATLAB implementation are illustrated for each mathematical model developed. Process flow diagrams are illustrated for the calculation of phase angle, dynamic properties, vibration energy and power, fluid flow power, and fluid energy transfer ratio, respectively.

In Chapter 6, the experimental results of the bellow system are listed and discussed. The experimental results were divided into two tests, high frequency and low frequency tests. At the end of the chapter the conclusions of the results are discussed.

In Chapter 7 the transient numerical model is validated, and the experimental results are evaluated. In this Chapter the transient numerical integration (MATLAB implemented) model is evaluated and discussed. The dynamic properties, vibration energy and power, and the portion of energy transferred to the fluid of the bellow system are evaluated in terms of amplitude, frequency, and pressure dependency, respectively. At the end of the Chapter the summary of the experimental evaluation results is discussed.

In Chapter 8 the conclusions of the study are discussed, with possible recommendations for future studies in similar systems.

2 Literature Review

2.1 Introduction

This literature review reviews different rubber compensators used in the engineering industry with a focus on rubber bellows. The mathematical equations required to model a rubber compensator in terms of vibration are reviewed along with the experimental methodologies designed to characterise the dynamic properties of rubber bellows.

From the literature study, the rubber bellow application, mathematical model, and experimental setup was chosen for this study.

2.2 Rubber Compensators

In this Section, different rubber compensators are briefly discussed. The main concept regarding each compensator is discussed in terms of appearance, application, advantages, and frequency range.

2.2.1 Cylindrical Mounts

These rubber mounts are used mainly to dampen the noise and vibration of stationary machinery at a frequency greater than 20 Hz (IAC-Acoustics, 2018), such as pumps and gearboxes. It is used to absorb compression in the axial direction; however, it cannot handle high shear forces. These rubber mounts usually have two galvanised plates (one at each end) with a central thread on each plate (IAC-Acoustics, 2018). From a catalogue obtained from IAC-Acoustics, it is seen that these mounts can handle a maximum load of 5 kg up to 1000 kg per mount and a static deflection of up to 11.5 mm (IAC-Acoustics, 2018). Figure 2-1 shows an example of a cylindrical rubber mount where the arrows illustrate the usual direction of amplitude.

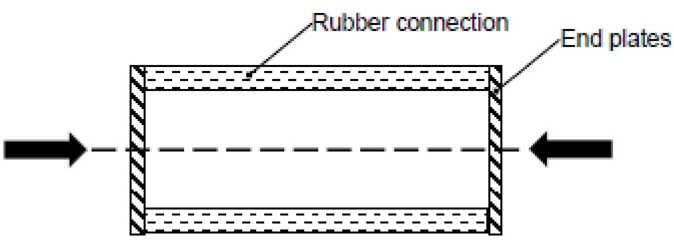

Figure 2-1: Example of a cylindrical rubber mount

Since the study focusses on the change in dynamic properties due to pressure changes in a process, this rubber mount will not be suitable for the study since it is not fluid filled or internally pressurised.

2.2.2 Rubber Turret Mounts

These rubber mounts are used mainly to protect smaller machinery against noise and vibration (IAC-Acoustics, 2018). These mounts help with isolation, which indicates that the mount is advantageous at high frequencies (Rao, 2011). These mounts provide relatively high deflection and can withstand high loads in multiple directions (IAC-Acoustics, 2018). From a catalogue obtained from IAC-Acoustics, it is seen that these mounts can handle a maximum load of 3.5 kg up to 3400 kg with a deflection range of 2.5 mm up to 45 mm depending on the type used (IAC-Acoustics, 2018). These mounts are similar to a cylindrical rubber mount, but with a small change in design to give a larger diameter base that tapers towards the smaller diameter top plate. Figure 2-2 shows an example of a rubber turret mount.

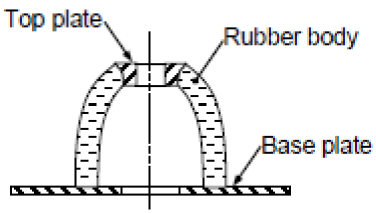

Figure 2-2: Example of a Turret Rubber Mount

Since the study is focussed on the change in dynamic properties due to pressure changes in a process, this rubber mount won’t be suitable for the study since it’s not fluid filled or internally pressurized.

2.2.3 Hydraulic Rubber Mounts

Hydraulic rubber mounts, also known as hydro mounts, are used in many applications. Hydro mounts consist of a spring and a hydraulic shock absorber in a single compact mount. The hydraulic aspect implemented in these mounts enables the mounts to be highly shock resistant (IAC-Acoustics, 2018). These mounts are mainly designed to provide isolation, reducing the forces transferred from an engine to the chassis of a vehicle (Wang *et al.*, 2014), this will then provide isolation when driving and shock absorbance when there is a sudden impact. From an IAC-Acoustics catalogue, it is seen that these mounts can handle a maximum load from 30 kg up to 410 kg with a deflection capability of up to 8 mm depending on the type selected (IAC-Acoustics, 2018). Hydraulic rubber mounts can provide more damping at lower frequencies; however, they are usually amplitude dependent in properties (Chai et al., 2014). There are many designs for hydraulic rubber mount. One of the most sophisticated and widely used hydraulic rubber mounts is the engine mount.

2.2.3.1 Hydraulic Engine Mounting (HEM).

Used as a vibration isolation part in a vehicle (Steyn, 2011), HEMs are highly valuable in the design of a vehicle assembly. These mounts reduce the vibration transferred from the engine to the chassis of a vehicle (Hosseini and Marzbanrad, 2017). Figure 2-3 below shows a typical HEM listing the main components.

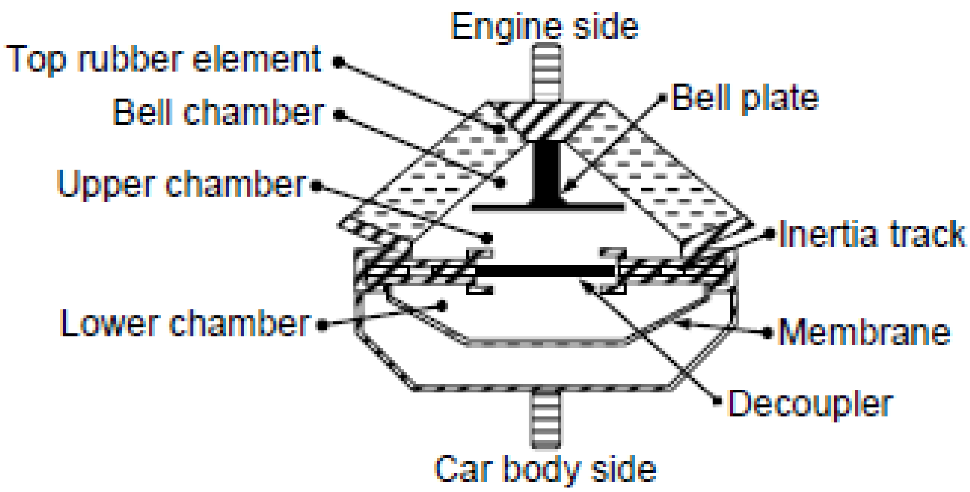

Figure 2-3: Schematic representation of a typical HEM (Hosseini and Marzbanrad, 2017) (Mansour, 2010)

The chambers in Figure 2-3, are filled with fluid, where vibrations from the engine increase the pressure in the upper chamber, forcing the fluid to the lower chamber, however if the pressure is increased too quickly the decoupler will restrict the fluid passing to the lower chamber that will make the mount more rigid to avoid excessive amplitudes. This enables the mount to have different dynamic properties under different conditions.

With HEMs, the change in dynamic properties is included in the design of the mount to manipulate these properties to ensure that optimal vibration isolation occurs at multiple amplitudes. From the review of the HEM internal fluid and pressure influence the dynamic properties of a rubber mount. However, the HEM as such is not designed to allow fluid moving in piping applications, which leads to the need for the next type of component, namely rubber bellows.

2.2.4 Rubber Bellow

A rubber bellow, also known as a rubber compensator, is an elastomer that is usually used to absorb unwanted vibrations in a vibrating system. In a piping system, the bellow works as an elastic flexible connection between two rigid pipes. The rubber bellow dampens and isolates the vibrations generated by the surrounding equipment such as pumps and other machinery. This damping protects the equipment and piping from damage as a result of unwanted vibrations. The flexibility in the rubber of a bellow absorbs the energy/vibrations that would normally be transferred in the pipeline. By isolating vibrations in the pipeline, the noise in the operating environment is also reduced.

The benefits of having a well selected rubber bellow is that more than 90% of unwanted vibrations could be absorbed and that not only the axial vibration/movement can be countered, but the lateral, tortional and angular movement as well (ORIA, n.d.). Normally the axial movement is used to absorb unwanted vibrations whereas the angular, lateral and tortional movement accommodates misalignment and thermal expansion. This study is focussed on the axial vibration of the in-line rubber bellow. In many studies on rubber bellows the study focusses on the axial vibration as it is the main direction of absorption (Mendia-Garcia et al., 2023) (Zheng et al., 2025).

Figure 2-4 illustrates a schematic example of an in-line rubber bellow application of a pump, where both the vibrations of surrounding equipment and the vibrations of the pump acting on the bellow. The deformation of the rubber bellow is also illustrated.

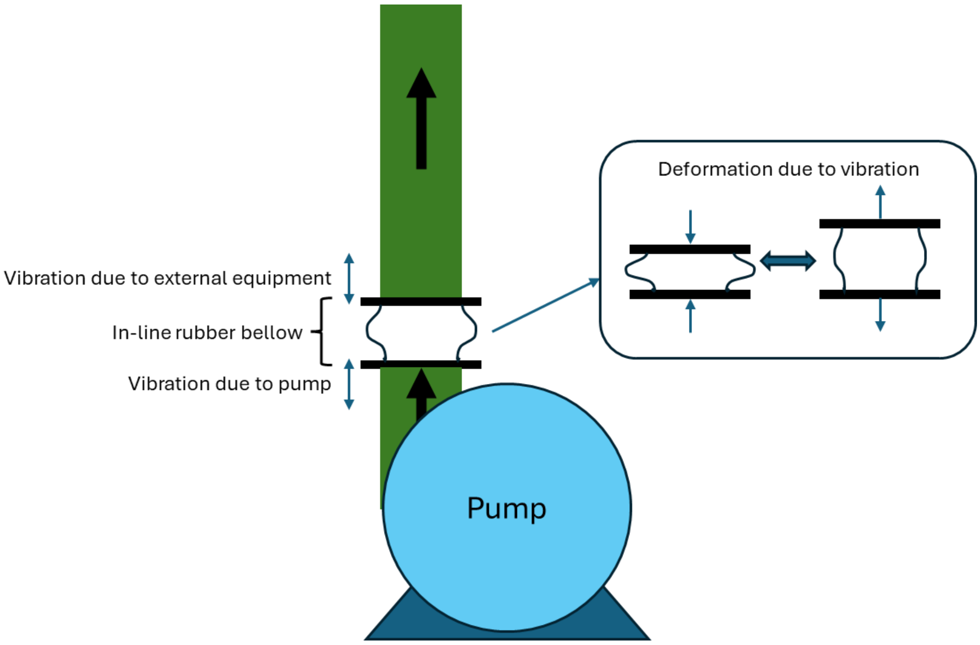

Figure 2-4: In-line rubber bellow schematic example

Because the bellow is made of an elastomer, there are a few factors regarding the material that plays a role in the dynamics of the bellow.

The stiffness of a rubber bellow or elastomer under static conditions differs from that under dynamic conditions and has been proven by numerous researchers (Nel & Wyngaardt, 2014). Elastomers provide a higher damping coefficient than steel, which is favourable when operating at or near resonance (Bloem, 2015). The dynamic stiffness of a rubber bellow was seen to depend on the amplitude of the dynamic vibration, with the dynamic stiffness and damping decreasing as the amplitude increased (Nel & Wyngaardt, 2014).

The rubber bellow is widely used in the industry for various applications, with a typical example shown in Figure 2-5. With multiple different types of rubber bellows available, it is mandatory to choose a rubber bellow that is most suitable for your application. Some bellows can withstand extreme temperatures, while others are made of an elastomer that can withstand aggressive chemicals.

Figure 2-5: Typical in-line rubber bellow (Willbrandt-Cummitechnik, n.d.)

In many applications of these bellows, the process conditions change significantly in pressure, amplitude, and frequency. Some applications are in-line where different fluids are transferred through. Some of these bellows can also withstand extreme high vibrating forces. For this study a Willbrandt Type 50 bellow was selected since these bellows are widely used in the industrial environment and because this bellow was used in a previous study at the University, making it available. According to Willbrantd's catalogue, the maximum repetitive axial deflection that a type 50 red DN 65 rubber compensator can withstand is 30 mm. From a study conducted on the properties of a type 50 red DN 65 Willbrandt bellow, the static stiffness was found to be 25 N/mm (Kent, 2015). This was determined at atmospheric pressure, where the stiffness of this bellow is seen to increase with an increase in pressure, as seen in Appendix A. With a maximum deflection of 30 mm and a stiffness of 25 N/mm the maximum static force that could be applied to the bellow is 750 N. However, this does not represent the forces that could be applied to the bellow dynamically.

In the following section, the modelling techniques that can be applied to a rubber below are described in terms of its appropriate system representations and relevant laws of motion. This is followed by an overview of typical experimental approaches with which to characterise this kind of dynamic system.

2.3 Mathematical Modelling of Rubber Bellows

A single degree-of-freedom forced excitation could be used to model a rubber bellow. Using this equation of motion, the equation could be derived to determine the work done by the system and, ultimately, the vibration power or energy. This Section gives a high-level explanation of the modelling of a rubber mount by using a single degree-of-freedom system.

2.3.1 Single Degree-of-Freedom System

An equation of motion for a vibrating or mechanical system is a differential equation that determines the change in position, with respect to time, of a vibrational system (Cai, 2016). Newton's second law of motion, also known as the equation of motion ($F = ma$), governs the motion of a physical system (Cai, 2016). From Newton's second law, the equations of motions for a dynamic vibrational system can be derived. Vibrational systems are usually categorised into four groups. These groups are undamped, underdamped, critically damped, and overdamped (Cai, 2016). Figure 2-6 is an example of an undamped single degree-of-freedom system, where k is the stiffness, m is the mass and x is the position of the mass (Rao, 2011).

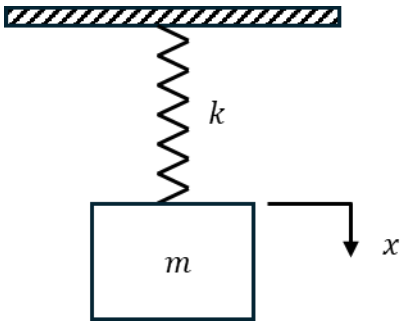

Figure 2-6: Undamped single-degree-of-freedom system

Without an external force applied to the mass, the equation of motion is as follows.

$$kx + m\ddot{x} = 0$$

If a vibrating system consists of some form of damping, the equation of motion could be derived and illustrated in Figure 2-7, where c is the damping coefficient of the system.

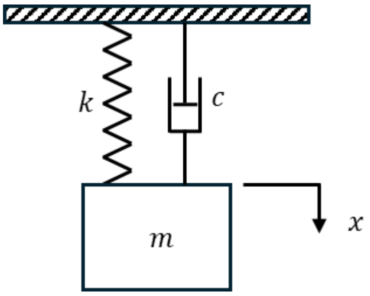

Figure 2-7: Damped single-degree-of-freedom system

Without an external force applied to the mass, the equation of motion is now:

$$kx + c\dot{x} + m\ddot{x} = 0$$

Where x is a function of time written as:

$$x = Xsin(\omega t)$$ (Rao, 2011)

Where X is the maximum amplitude of the displacement, x. The velocity and acceleration can be written as:

$$\dot{x} = dx/dt$$

$$\ddot{x} = d\dot{x}/dt$$

2.3.1.1 Forced excitation steady state

Steady-state vibration refers to a harmonic and persistent vibrational response of a system (Cai, 2016). Figure 2-8 illustrates a schematic representation of a forced excitation system with a single degree-of-freedom.

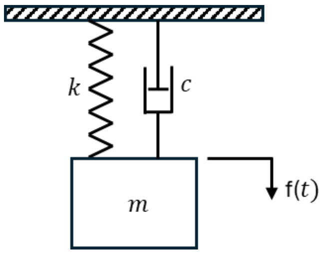

Figure 2-8: Forced excitation, damped single-degree-of-freedom system

From the equation of motion (Newton's second law), a steady-state equation of motion could be derived where an external harmonic force is applied:

$$F(t) = kx + c\dot{x} + m\ddot{x}$$

Here, $F(t)$ is the external harmonically force applied to the mass as a function of time.

2.3.1.2 Forced excitation transient state

Transient-state vibration refers to a system response due to external forced excitations directly after the start of the excitation until the response reaches a steady-state response, as mentioned in Section 2.5.1.1 (Cai, 2016). The equation of motion remains the same as a function of time. Figure 2-9 illustrates a typical transient response when a harmonic excitation is applied to a damped system.

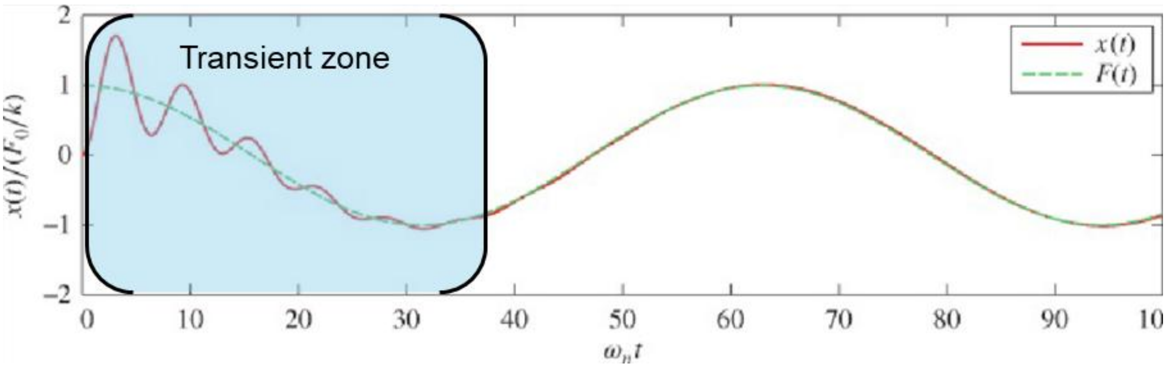

Figure 2-9: Response example of transient behaviour, adapted from (Cai, 2016)

Here, the red line is the displacement of the mass, and the green line is the forced excitation.

The mathematical modelling of a single degree-of-freedom system is further explained and utilised in Chapter 4.

2.3.2 Vibrational Energy and Power

From the equation of motion derived from Newton's second law of motion, the work (U) done by the bellow system, between two points, x_1 and x_0, could be expressed as:

$$U = \int_{x_0}^{x_1} F(t)\,.\,dx$$ (Gross et al., 2014)

The work done over a period of time is known as the power and can be further derived where the power, $\mathbb{P}$, used by the system due to the force, F, at a velocity, v, is:

$$\mathbb{P} = F\ v$$ (Gross et al., 2014)

By applying the power equation above to the steady state equation of motion, where an external harmonic force is applied as a function of time, the vibrational power could be expressed as:

$$\mathbb{P} = F(t)\dot{x}$$

From the above equation, the vibrational power could be modelled mathematically and implemented in a MATLAB environment, as discussed in Section 5.4.

Since the study and setup are based on a hydraulic filled rubber bellow, it is important to determine the amount of energy transferred from the bellow movement to the fluid to determine the degree to which the fluid complements the damping force of the rubber material itself to recognise how much the fluid acts as a damper in a fluid filled scenario. Section 2.3.2.1 reviews the hydraulic energy transfer in a fluid filled system.

2.3.2.1 Hydraulic Energy Transfer

The two main energy transfers that occur in a hydraulic machine is the contact of the fluid with the moving solid surfaces that produces a boundary layer, producing frictional losses, and the fluid that changes direction and separates, causing shock losses (Douglas et al., 1985).

For the application of an in-line rubber bellow, the vibration energy transferred from the bellow to the fluid is a portion of damping provided by the fluid itself. Similar to any pumping system, the energy transferred from the mechanical (vibrational) energy to the fluid can be calculated by determining the flow and pressure of the fluid caused by the oscillation/rotation of the pump, using Bernoulli's equation (Douglas et al., 1985). The mathematical calculation of the energy transferred to the fluid is further discussed in Chapter 4.

2.3.3 Iterative Numerical Calculating Software

To model the vibration energy of a rubber bellow, a numerical calculating programming language is required. Although there are many different software available such as Python, GNU Octave and R that has built in numerical solvers capable of modulating a numerical model, MATLAB has been used in many studies (Bloem, 2015) (Nel and Steyn, 2012) and vibration handbooks (Cai, 2016) (Rao, 2011) to simulate, calculate, and validate vibration experimental studies. Therefore, it is better to implement the mathematical model in a MATLAB environment since the implementation can be referenced to previous studies. In a study to optimise the design of a vibrating screen, ode23 was used to predict the transient response of a rubber mount, Figure 2-10 illustrates the predicted startup (top graph) and stop (bottom graph) response of a rubber mount as calculated by using ode23 in a MATLAB environment.

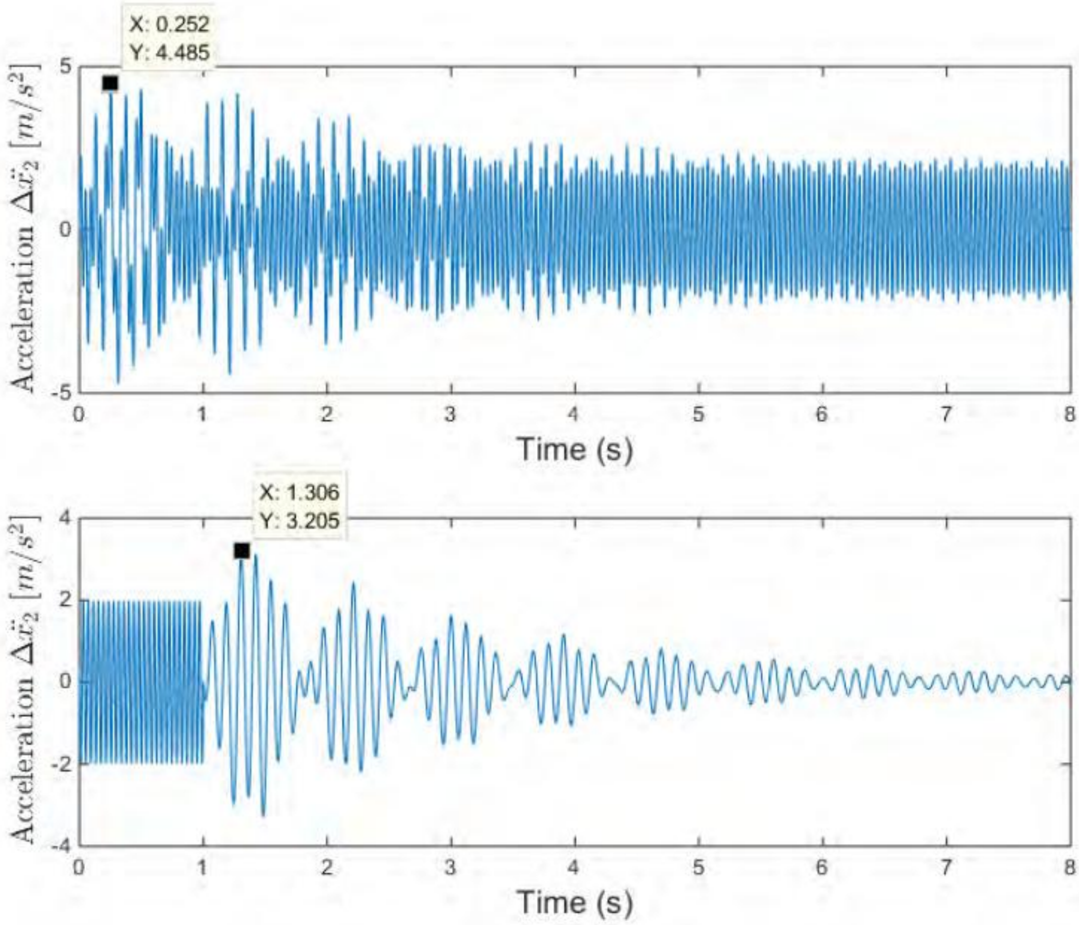

Figure 2-10: $\mathrm{ode23}$ transient implementation example (Bloem, 2015)

From previous studies, (Bloem, 2015) and (Steyn, 2011), using the build in MATLAB script ode23, delivered a good correlation between the predicted and experimental results.

2.4 Experimental Evaluation of Rubber Bellows

A well-controlled setup and analyser(s) are required to enable the experimental evaluation of the mathematical modelling as discussed in Section 2.3. By evaluating the equation of motion, the variables are force, stiffness, damping, mass, and motion (displacement velocity and acceleration) as a function of time. Where the displacement in a harmonic vibrating system could be seen as (Rao, 2011):

$$x(t) = Xsin(\omega t - \phi)$$

$$\dot{x}(t) = \dot{X}\cos(\omega t - \phi)$$

$$\ddot{x}(t) = \ddot{X}\sin(\omega t - \phi)$$

Where x, $\dot{x}$ and $\ddot{x}$ is the displacement, velocity and acceleration, respectively, as a function of time, t. X, $\dot{X}$ and $\ddot{X}$ is the displacement-, velocity- and acceleration amplitudes, respectively. ω and ϕ is the frequency and phase angle. The phase angle can be seen as the 'lag' between the applied force and the motion of the mass, which is caused by the damping in the system (Rao, 2011). Figure 2-11 illustrates the difference in displacement motion and applied force, also known as phase angle (Marscher, 2020).

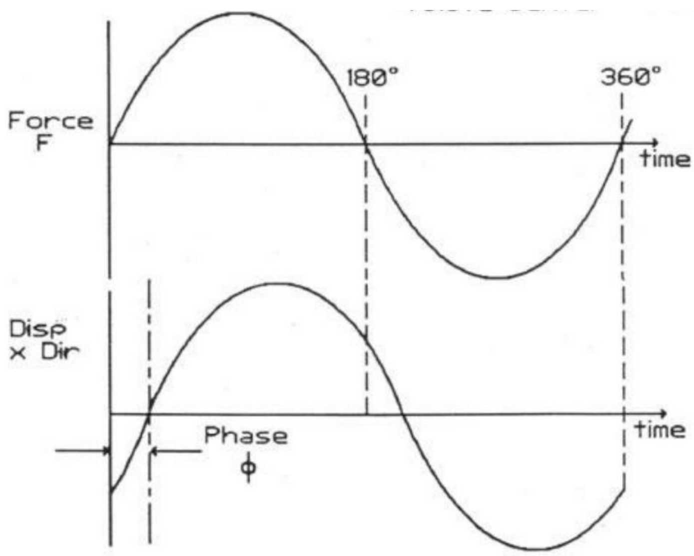

Figure 2-11: Phase angle illustration

The phase angle can be calculated by (Rao, 2011):

$$\phi = tan^{-1}\left[\frac{c\omega}{k - m\omega^2}\right]$$

This Section will review different experimental setups used to characterise rubber bellows.

2.4.1 Dynamic Mechanical Analyser

Dynamic Mechanical Analysis (DMA) is a method used to characterise the viscoelastic properties of materials such as polymers, by applying an oscillating load to the material. The stress and strain of the sample are measured to determine the properties of the material (NETZSCH, 2025). Figure 2-12 illustrates a DMA system, this specific model has a built-in oven where the material that is tested can be heated up to the desired experimental temperature.

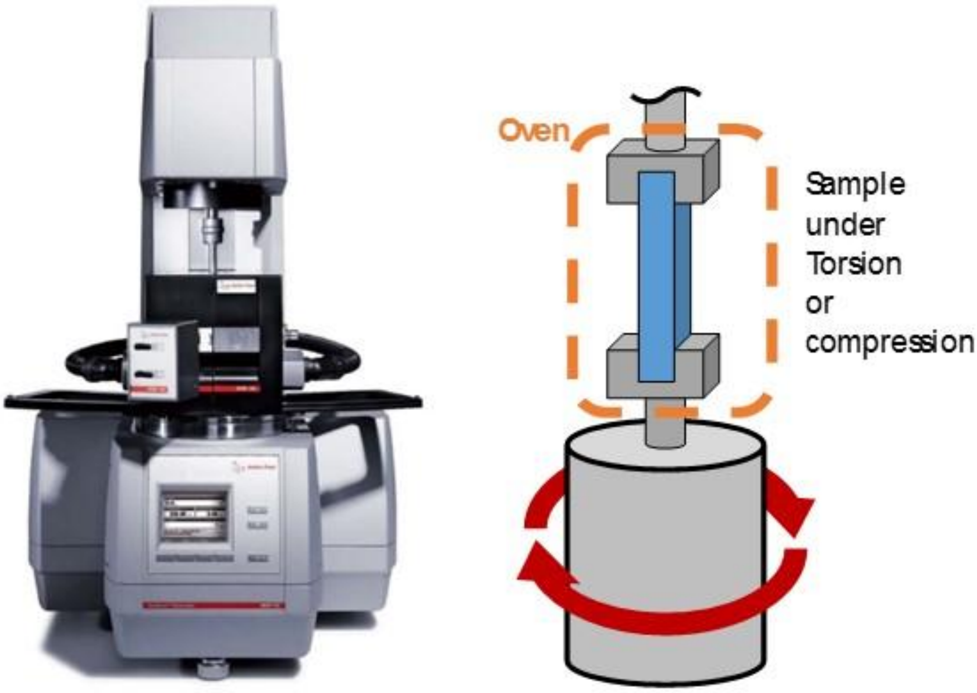

Figure 2-12: Example of a Dynamic Mechanical Analyser (Lubomirsky, 2025)

Although these setups are used mainly for stress and strain tests, it could be implemented to characterise the properties of a rubber bellow by determining the force required to oscillate the bellow at a certain frequency.

2.4.2 Electrodynamic Shaker

A commonly used excitation source to evaluate the properties of a rubber mount is an electromagnetic shaker, also known as a vibration shaker. These shakers are usually air cooled and create a forced frequency by means of electromagnetic oscillation. Figure 2-13 shows a typical experimental setup of electromagnetic shakers.

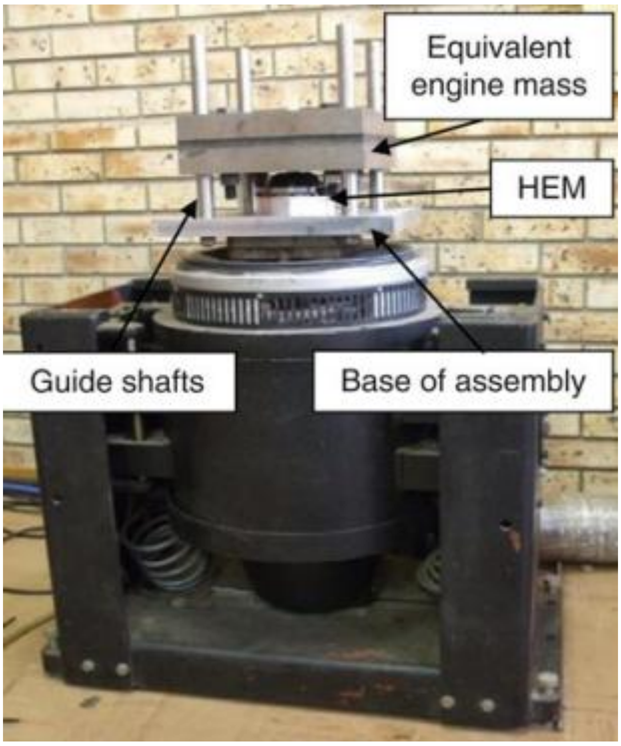

Figure 2-13: Electromagnetic shaker engine mount setup (Nel and Steyn, 2012)

By attaching accelerometers to the base and the mass, the two acceleration responses can be taken and processed by an FFT analyser.

2.4.3 Impact Hammer Modal Testing

An impact hammer is a setup that is used to apply a short force to a structure or system. To evaluate the properties of a rubber bellow with an impact hammer, an FFT analyser with accelerometers or a force transducer is required. Some modern impact hammers have built in sensor analysers, where the setup can be more consequent than your conventional impact hammer.

Figure 2-14: Modern impact hammer (GmbH, n.d.)

In a study to evaluate the stiffness and damping of a frequency-dependent rubber mount an impact hammer setup was used. The method of experimental setup was then validated by comparing the results with a mechanical shaker test. The results were that the impact hammer test was a quick and easy way to evaluate the rubber mount, although some adjustments had to be made in terms of the weight of the impact and how hard the hammer should be (Lin et al., 2004).

Since the impact hammer cannot create a steady state forced frequency, this setup will not be advisable to determine the dynamic properties of a fluid filled rubber bellow.

2.4.4 Experimental Setup Excitation Source with Unbalanced Motors

As mentioned in Section 1.6, the excitation source was chosen as two unbalanced motors. These unbalanced motors are commonly used to excite vibrating screens (Bloem, 2015).

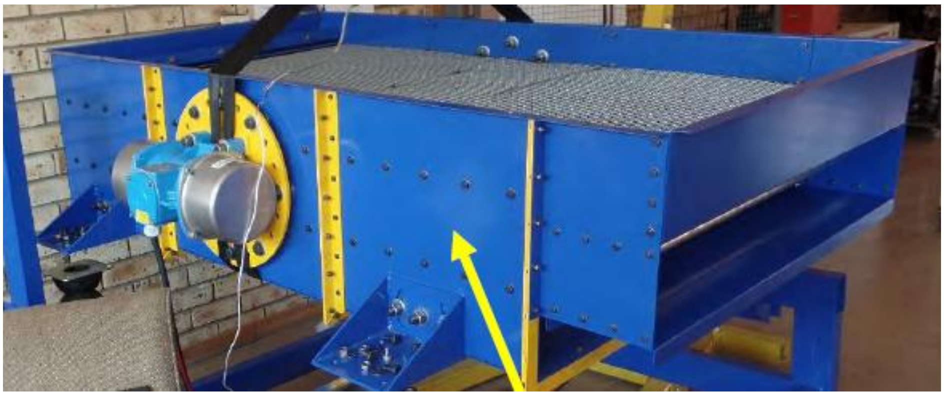

Figure 2-15: Example of unbalanced motor used in a screening application (Bloem, 2015)

In Section 3.3, examples of accelerometers and FFT analysers are shown. These responses can be downloaded to a PC and uploaded to a programming language, such as MATLAB, where the frequency, amplitude, and phase angle can be determined. Using these values, the equation of motion can be determined.

2.5 Conclusions

The literature study reviews different rubber compensators and the application of these compensators. The properties of these compensators were briefly discussed along with the advantages of these compensators. For this study a rubber bellow was selected and the modelling of a typical rubber bellow was reviewed, this included the modelling of the equation of motion, the vibrational energy and power, and the iterative numerical integration software to evaluate the transient behaviour of the bellow. Different experimental evaluation methods of a rubber bellow were reviewed. From the literature review, the experimental methodology and setup were determined and discussed in Chapter 3, the mathematical models were developed in Chapter 4 and the implementation of the models were determined in Chapter 5.

3 Experimental Methodology

By combining relevant concepts from previous literature, a test rig was designed and constructed to investigate the dynamic properties of a rubber bellow. In this Chapter the experimental setup is discussed and illustrated along with the instrumentation required to characterise the rubber bellow.

Figure 3-1 illustrates the schematical representation of the experimental setup that will be discussed in this Chapter.

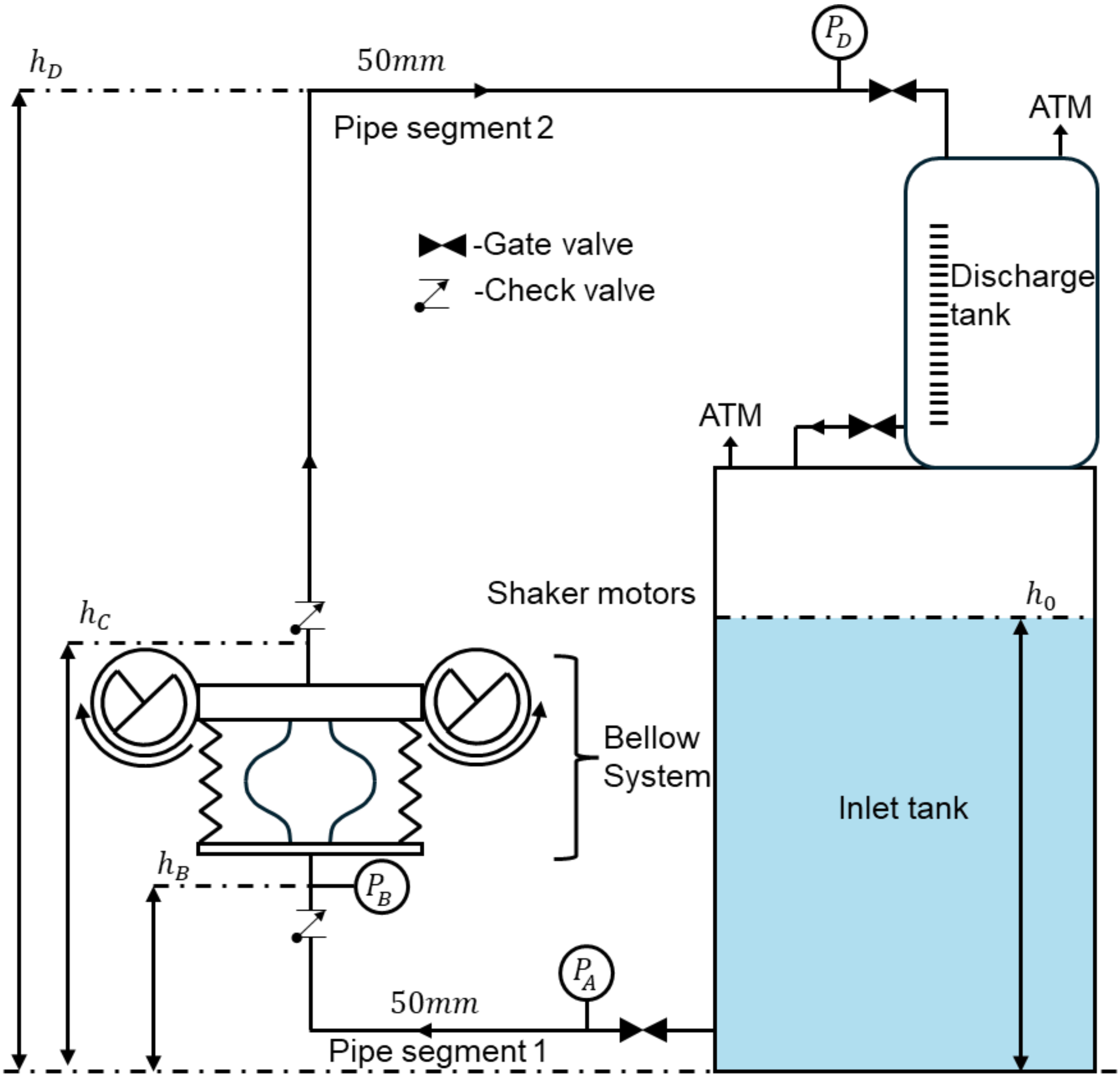

Figure 3-1: In-line rubber bellow schematic experimental setup

Vibration was induced by two electrical shakers for higher frequencies, and at lower frequencies a camshaft driven by an electrical motor gearbox was used. Vacuum and pressure gauges were used to determine the pressure differential in the rubber bellow. In order to determine the amount of energy transferred to the fluid of the system, two one-way valves were installed, as seen in the Figure, before and after the bellow. This requirement and mathematical approach are explained further in Chapter 4.To measure the flow rate, a 25 litre container that is transparent and marked in increments of 0,25 litres was used along with a stopwatch. To measure vibrations, an accelerometer with a Fast Fourier Transform (FFT) analyser was used, and an eddy current probe was used to calibrate the phase angles of the vibration system. In the lower-frequency tests, a load cell was used to measure the forces transferred to the rubber compensator by the camshaft and gear reduction gearbox.

The experimental evaluation was conducted at frequencies ranging from 2.5 Hz to 25 Hz. Where the high frequency test ranged from 12,5 to 25 Hz and the low frequency tests ranged from 2,5 to 5 Hz. At each frequency the inlet and outlet valves were used to manipulate the pressure in the system to test each steady state condition at a differential pressure range from -30 kPa (vacuum) to 50 kPa, unless the fluid flow was unstable at one of these operating conditions, where the results were neglected as they aren't deemed as accurate.

For frequencies between 12.5 and 25 Hz, the unbalance mass of the electromotor shakers was adjusted to manipulate the amplitude of the condition by changing the unbalance mass, where the low frequency test was conducted with one camshaft with a fixed offset distance (amplitude).). The unbalance percentage ranged from 50% to 100%.

Table 3-1 and Table 3-2 illustrates the measuring points or matrix of the experimental evaluation for the low frequency and high frequency tests, respectively. Where 6 measuring points were completed for each frequency for the low frequency tests, one test for each pressure differential at each frequency, and 12 measuring points were completed for each frequency at the high frequency tests, one test for each pressure differential, at 50% and 100% unbalance mass, at each frequency.

Table 3-1: Low frequency experimental matrix

f [Hz]	P_D [kPa]
2,5 [Hz]	-30
	-20
	0
	20
	35
	50
3,5 [Hz]	-30
	-20
	0
	20
	35
	50
5 [Hz]	-30
	-20
	0
	20
	35
	50

Table 3-2: High Frequency experimental matrix

f [Hz]	Unbalance percentage [η]	P_D [kPa]
12,5 [Hz]	50%	-30
		-20
		0
		20
		35
		50
	100%	-30
		-20
		0
		20
		35
		50
18,75 [Hz]	50%	-30
		-20
		0
		20
		35
		50
	100%	-30
		-20
		0
		20
		35
		50
25 [Hz]	50%	-30
		-20
		0
		20
		35
		50
	100%	-30
		-20
		0
		20
		35
		50

3.1 Calibration and Calculation of Phase Angle

A reference phase angle of “zero” degrees was determined to determine the phase angle of the bellow in each condition. If there was no damping in the bellow system, c_p, is zero, the phase angle would also be zero as determined by Equation (4-12). Steel springs have a very low damping ratio approximately ζ=0.005 (Hutchinson, 2018), therefor the phase angle can be simplified to zero if the system only consists of springs for the phase angle calibration process. The bellow’s rigid mass and unbalance motors were mounted upon the 8 steel springs without the bellow rubber to eliminate as much damping as possible. The equivalent stiffness, k_s, of the 8 steel springs was 24 N/mm and the weight of the mass, m, used for the calibration was 45 kg. Thus the natural frequency, f_n, of the calibration system was calculated as 3.68 Hz ($f_n = \sqrt{\frac{k_s}{m}}\left(\frac{1}{2\pi}\right)$) (Rao, 2011). The calibration was done at a frequency of 25 Hz, which was more than 6 times the natural frequency. With a frequency ratio of three or more and a low damping coefficient, ζ, of 0.005, the phase angle, ϕ, could be assumed to be 180 degrees (Rao, 2011). Thus, the damping present in the phase angle calibration setup could be neglected.

The EC displacement sensor was attached to the shell of the unbalance motor on the bottom side of the unbalance motor facing a vertical upward direction, as shown in Figure 3-2.

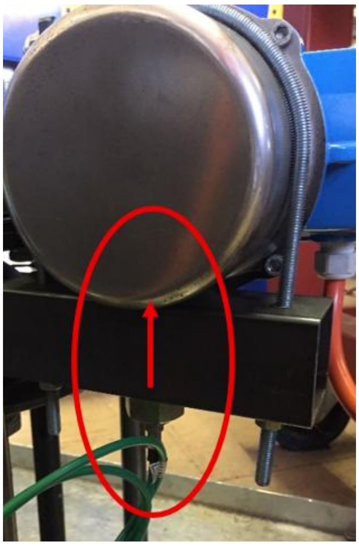

Figure 3-2: EC displacement sensor mounted to motor

By placing the PCB accelerometer on the rigid body mass and neglecting damping as described, the excitation force, F_e, of the motor was in sync with the acceleration of the body. The EC sensor only read the distance between the unbalance weight and the sensor, where the reference calibration phase angle ϕ_{eik} was measured from the FFT signals. Figure 3-3 and Figure 3-4 show the schematic representation of the calibration setup for 100% and 50% unbalance. A similar process was followed to calibrate other unbalance settings.

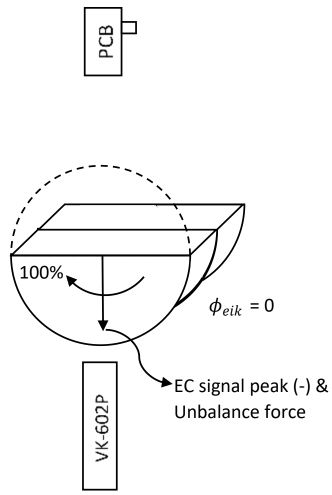

Figure 3-3: 100% phase angle representation

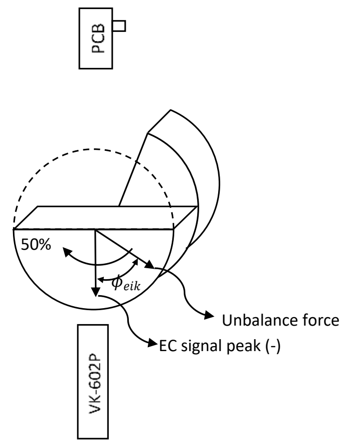

Figure 3-4: 50% phase angle representation

3.2 Excitation Force

Two Venanzetti VV10B/4 electric shaker motors were attached to opposite sides of the top plate of the bellow system, as shown in Figure 3-5.

Figure 3-5: Unbalance motor attachment

The rotating direction of the motors should be opposite as described in the user manual (VENANZETTI-VIBRAZIONI-MILANO, 2003) and as seen in Figure 4-2, to ensure a vertical induced vibration (motors stays in phase).

The angular speed of the shaker motors was controlled with a Variable Speed Drive (VSD). The shaker motors have a maximum rotating speed of 25 Hz and deliver a maximum vibration force of 2.1 kN at this frequency. The unbalanced mass of the motors is variable and can be adjusted to a percentage of the total unbalanced mass-radius given by the manufacturer as 0.087 kgm (Vipro, n.d.).

Figure 3-6 shows the specifications of the unbalance vibration motors used.

4 poles Three-phase electric vibrators - 1500/1800 rpm

DESCRIPTION			MECHANICAL SPECIFICATIONS						ELECTRICAL SPEC.						
			STATIC MOMENT		CENTRIFUGAL FORCE				MAX. INPUT POWER (W)		MAX. INPUT CURRENT (A)		Weight (kg.)		
Code	Type	Size	kgmm		kg.f		kN				400V	460V			Ref
			50Hz	60Hz	50Hz	60Hz	50Hz	60Hz	50Hz	60Hz	50Hz	60Hz	50Hz	60Hz	
V4000	VV03B/4	BA	14,0	11,6	35	42	0,343	0,412	80	90	0,20	0,19	6,0	6,0	2
V4001	VV05B/4	BA	32,0	22,1	80	80	0,785	0,785	80	90	0,20	0,19	6,6	6,4	2
V4002	VV10B/4	CA	87,0	60,8	220	220	2,16	2,16	160	160	0,38	0,38	12,5	11,5	2
V4003	VV20B/4	DA	167	116	420	420	4,12	4,12	280	330	0,57	0,57	19	18	2
V4004	VV30B/4	EA	298	215	750	780	7,36	7,65	500	620	0,88	0,93	28	26	2
V4005	VV35B/4	GA	437	276	1100	1000	10,8	9,81	520	640	0,90	0,90	45,5	41	2
V4006	VV38B/4	HA	556	387	1400	1400	13,7	13,7	850	1000	1,37	1,43	55	52	2
V4007	VV40B/4	IA	714	483	1800	1750	17.7	17.2	1100	1200	1,91	1,83	61	57	2
V4016	VV41B/4	IA	833	566	2100	2050	20.6	20.1	1300	1400	2,40	2,20	72	70	2
V4008	VV50B/4	LA	992	691	2500	2500	24.5	24.5	1500	1600	3,00	2,90	85	79	2
V4017	VV53B/4	LA	1250	870	3150	3150	30.9	30.9	1800	1900	3,60	3,30	95	92	2
V4009	VV55B/4	MA	1508	1050	3800	3800	37.3	37.3	2100	2400	3,80	3,70	118	113	2
V4018	VV57B/4	MA	1746	1188	4400	4300	43.2	42.2	2400	2700	4,60	4,40	125	120	2
V4010	VV60B/4	NA	1984	1367	5000	4950	49.1	48.6	3400	3200	5,70	4,80	174	166	2
V4011	VV67B/4	OA	2619	1823	6600	6600	64.7	64.7	5700	5700	10,0	8,60	212	200	2
V4012	VV71B/4	PA	3175	2210	8200	8200	80.4	80.4	6600	7600	11,0	10,9	228	213	2
V4013	VV81B/4	QA	3373	2486	8500	9000	83.4	88.3	7100	8000	11,5	11,3	319	305	3

	DIMENSIONAL SPECIFICATIONS														
	Fixing distances					Fixing holes									
Code	A	B	C	D	E	ØF	N°	G	H	I	L	M	N	O	Cable gland
V4000	62-74	106	216	125	30,5	9	4	24	23	93	154	129	64	50	PG13,5
V4001	62-74	106	216	125	30,5	9	4	24	23	93	154	129	64	50	PG13,5
V4002	90	125	295	152	28,5	13	4	28	30	93	178	144	73	80	PG13,5
V4003	105	140	340	167	32	13	4	28,5	30	111	204	163	80	96	PG16
V4004	120	170	376	205	38	17	4	40	33	111	214,5	191	91,5	97	PG16
V4005	120	170	436	210	60	17	4	22	47,5	111	243	223	115,5	118	PG16
V4006	140	190	438	230	72	17	4	25	45	111	257	241	124,5	103	PG16
V4007	140	190	486	230	72	17	4	25	45	111	257	241	124,5	127	PG16
V4016	140	190	557	230	72	17	4	25	45	111	257	241	124,5	162,5	PG16
V4008	155	225	522	275	79.5	22	4	28	55	111	283	271	140	129.5	PG16
V4017	155	225	600	275	79.5	22	4	28	55	111	283	271	140	168.5	PG16
V4009	155	255	590	310	103.5	23.5	4	30	60	155	335	309	160	140	PG16
V4018	155	255	658	310	103.5	23.5	4	30	60	155	335	309	160	174	PG21
V4010	180	280	638	340	106	26	4	30	65	155	369	336	173	154	PG21
V4011	200	320	662	390	111	28	4	32	75	155	381	384	189	151	PG21
V4012	200	320	624	392	111	28	4	35	75	155	403	402	199.5	132	PG21
V4013	125	380	862	460	70	39	6	35	95	170	434.5	439	215	230	PG21

Figure 3-6: Unbalance motor specification sheet (Vipro, n.d.)

The unbalance percentage n was adjusted for each condition of the characterisation scope. Figure 3-7 shows the changeable unbalance mass-radius of the motor. The unbalance force was solved by Equation (4-2) for each characterisation measurement.

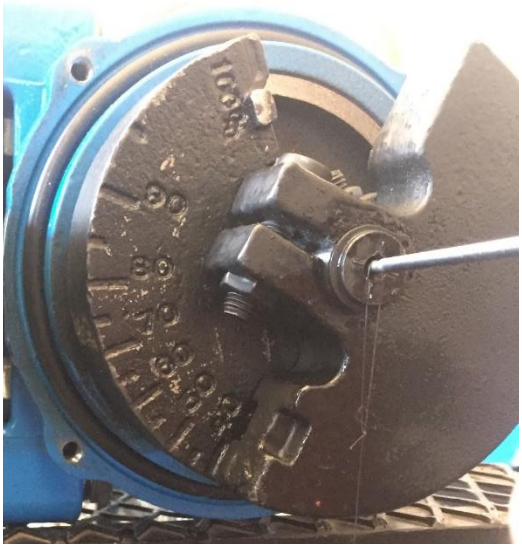

Figure 3-7: Adjustable unbalanced mass-radius

3.3 Vibration Instrumentation

Some vibration instruments were required to successfully characterise the bellow. Characterisation was performed by implementation of an accelerometer and an eddy current (EC) probe.

A 100 mV/g PCB accelerometer was used with a cable that was connected to a two-channel Diagnostic Instruments (DI) 2200 FFT Analyser. Figure 3-8 shows the accelerometer that was used during the experimental characterisation of the system.

Figure 3-8: Accelerometer

A non-contact EC displacement sensor was used to measure where the unbalance mass was in relation to the acceleration of the bellow, as explained in Section 3.1. The

Shinkawa model VK-602P EC sensor with transducer was used, the transducer supplied a voltage that is proportional to the distance between the unbalance weight and the sensor and was attached to the second available channel of the DI. Figure 3-9 shows the EC sensor transducer box.

Figure 3-9: Transducer box

Figure 3-10 shows the DI FFT analyser that was used to analyse the signal that was received from the accelerometer and the eddy current probe.

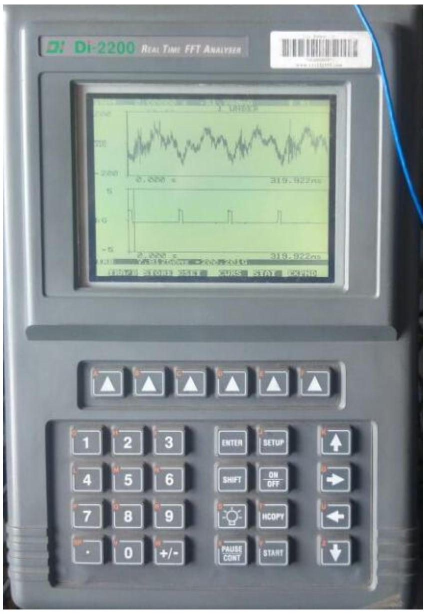

Figure 3-10: FFT Analyser

The signal received from the accelerometer and the EC probe that was recorded by the analyser was downloaded to a personal computer. The data obtained from the analyser were used to calibrate the phase angle and to characterise the dynamic properties of the bellow system.

3.4 Bellow System

The setup shown in Figure 3-11 consisted of the rubber bellow, additional springs, top mass which comprises of the top plate, motors with brackets, discharge pipes and the water inside the discharge pipes, two excitation motors and two one-way valves on each end of the bellow. A small section of the discharge pipe is also seen.

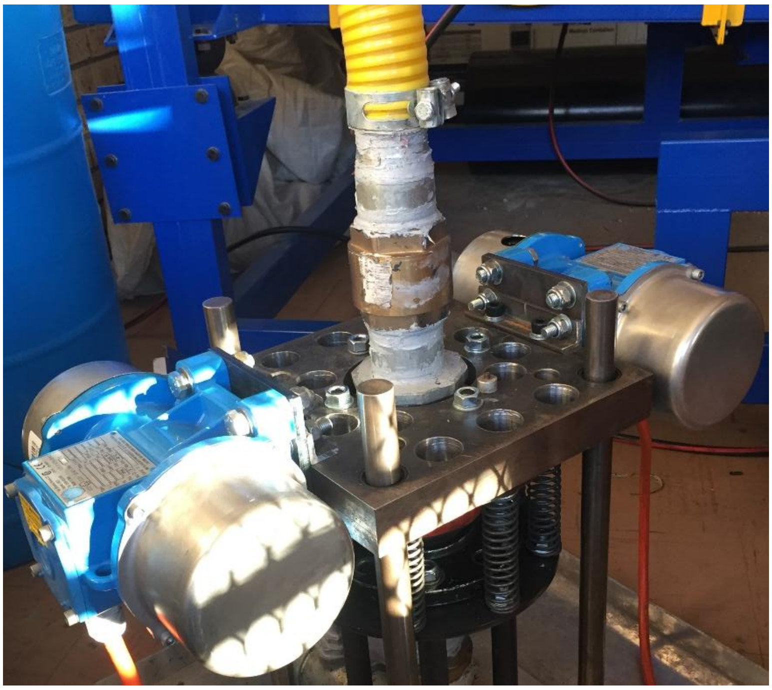

Figure 3-11: Bellow system rigid body mass and discharge one-way valve

The discharge pipe section consisted of a set of 2-inch galvanised steel pipes with a gate valve, pressure gauge and one-way valve along with a helical plastic pipe with a diameter of 50 mm, as seen in Figure 3-12. Two tanks were used in the system, also seen in Figure 3-12, with a valve between the two tanks. The top tank, also referred to as the discharge tank was transparent with markings on, where the inlet tank was a 200-litre tank that is blue of colour and was used as the main reservoir for the system.

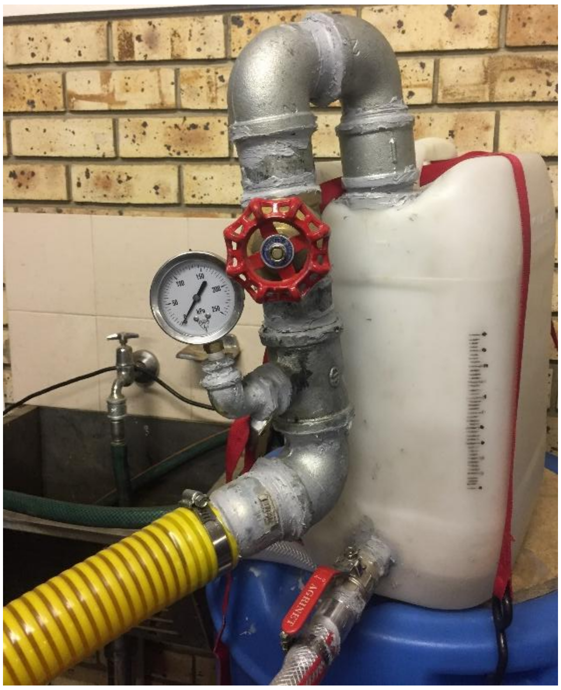

Figure 3-12: Discharge pressure gauge, gate valve, and two tanks

The inlet pipe section consisted of a set of 2-inch galvanised steel pipes with a gate valve, vacuum gauge, and one-way valve with a diameter of 50 mm.

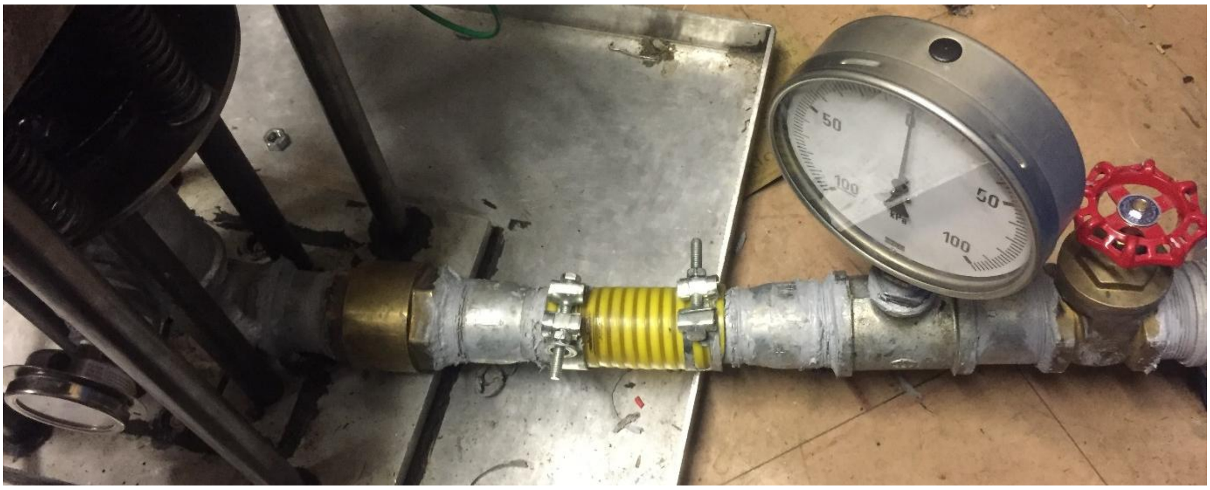

Figure 3-13: Inlet/suction pressure gauge, one-way valve, and gate valve

The piping consisted of an inlet pipe segment, shown in Figure 3-13, and discharge pipe segment, shown in Figure 3-12. These segments consisted of gate valves on each pipe segment along with three pressure gauges. These pressure gauges were at the inlet of the system, shown in Figure 3-13, the bellow itself, shown in Figure 3-14 and one at the discharge pipe shown in Figure 3-12.

Figure 3-14: Pressure gauge P_B, situated at the inlet of the bellow

A summary of all the measured dimensions and required parameters in terms of the characterisation used in the mathematical model, are indicated in Table 3-3.

Table 3-3: Characterisation Parameters

Parameter	Magnitude
m_m	58 kg
l_1	1080 mm
l_2	1120 mm
h_0	550 mm
h_A	395 mm
h_B	175 mm
h_C	590 mm
h_D	1280 mm
D_1	50 mm
D_2	50 mm
ρ	1000 kg/m^3
g	9.81 m/s^2
μ	1.002e-3 Ns/m^2
P_{atm}	86 kPa

The density and dynamic viscosity (Munson *et al.*, 2010) of the fluid ρ and μ was chosen as 1000 and 1.002e-3 respectively and the gravitational constant is 9.81 (Halliday *et al.*, 2014).

Chapter 4 provides more detail on the specific mathematical models used.

4 Mathematical Models

4.1 Introduction

For this study, four mathematical models were developed. From the literature review, the mathematical model was developed by implementing the parameters to the experimental setup as discussed in Chapter 3. The first model was developed to characterise the dynamic properties of the bellow. The second model was developed to describe the vibration energy. The third model was developed to describe the water flow energy of the bellow, determining the energy transferred by the bellow, and the fourth model was developed to describe the fluid energy transfer ratio of the bellow system.

4.2 Dynamic Properties of Bellow

A single degree-of-freedom model was developed to characterise the dynamic properties of the bellow. The bellow was idealized as a spring, that consisted of the stiffness of the rubber k_r and the steel springs k_s and a viscous damper c_m attached to a rigid foundation with a rigid body on top of the spring with a mass m_m and two non-return valves as shown in Figure 4-1. The 8 steel springs were added to the system to assist with the deflection caused by the equivalent mass m_m, these springs are shown in Figure 3-11 as two springs where k_s is the equivalent stiffness of all 8 steel springs. The one-way valves before and after the bellow were considered part of the bellow system because they restrict flow in the opposite direction and are shown in Figure 4-1 as two square blocks with a cross through them. The translational mode for movement in the vertical direction was considered. The equivalent vertical stiffness of the bellow is

$$k_m = k_r + k_s \tag{4-1}$$

A viscous damping model was used to describe the damping characteristics of the bellow. The vertical viscous damping coefficient of the bellow is c_m. Note that the above was applicable regardless of whether the bellow is full of fluid or air.

The mass on top of the spring was subjected to oscillating forces produced by two identical exciter motors, fastened to opposite sides of the body mass to achieve linear oscillation (Venanzetti, 2013). These two electrical motors rotated in opposite directions relative to each other. The resulting force was produced only in the vertical direction (Venanzetti, 2013). The two motors were placed equally apart from the centre of gravity of the bellow to maintain a balanced system. The excitation force produced by the exciter motors F_e caused linear vertical movement of the mass.

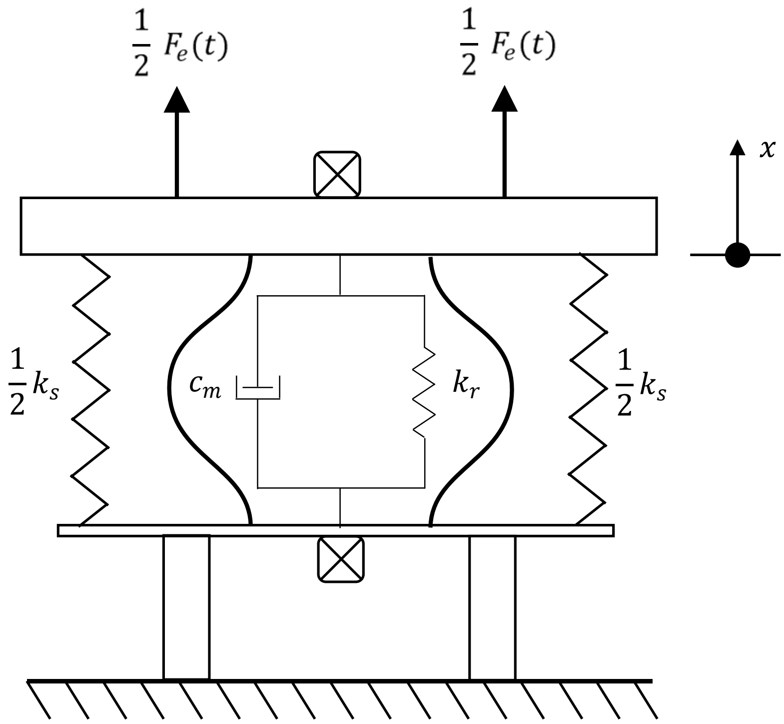

Figure 4-1: Bellow in single degree of freedom

One excitation motor produces an unbalance force F_u that consists of the equivalent unbalance product of the motor $m_e r_e$

$$F_u = \frac{n}{100} m_e r_e \omega^2 sin(\omega t) \tag{4-2}$$

where ω is the rotational speed of the motor and n is the percentage of unbalance that the motor is set to (varies from 0 to 100). The resultant force produced by the two exciter motors can be described as an excitation force F_e. The magnitude of the resultant shaking force as a function of time t is

$$F_e = 2\frac{n}{100} m_e r_e \omega^2 sin(\omega t) \tag{4-3}$$

where the equivalent unbalance product of the exciter motors $m_e r_e$ is related to the unbalance mass m_e of the motor with its respective radius of gyration r_e, thus the force magnitude can be described as

$$F_e = 2\frac{n}{100}m_e r_e \omega^2 \tag{4-4}$$

From Figure 4-1 and Newton's second law (Rao, 2011), for the equilibrium of dynamic forces, the differential equation of motion is

$$F_e(t) = k_m x + c_m \dot{x} + m_m \ddot{x} \tag{4-5}$$

where x, $\dot{x}$ and $\ddot{x}$ are the displacement, velocity and acceleration in the vertical direction respectively. The vertical displacement x at time t can also be expressed in terms of the corresponding displacement amplitude X as

$$x(t) = Xsin(\omega t - \phi) \tag{4-6}$$

where ϕ is the phase angle and can be calculated as

$$\phi = \Delta\phi - \phi_{eik} \tag{4-7}$$

where $\Delta\phi$ is the measured phase angle and ϕ_{eik} is the calibrated phase angle as described in Chapter 3. Similarly, the vertical velocity $\dot{x}$ at time t can also be expressed in terms of corresponding velocity amplitude $\dot{X}$ as

$$\dot{x}(t) = \dot{X}cos(\omega t - \phi) \tag{4-8}$$

Similarly, the vertical acceleration $\ddot{x}$ at time t can also be expressed in terms of corresponding acceleration amplitude $\ddot{X}$ as

$$\ddot{x}(t) = \ddot{X}sin(\omega t - \phi) \tag{4-9}$$

The natural frequency (Rao, 2011) of the bellow is

$$\omega_n^2 = \frac{k_m}{m_m} \tag{4-10}$$

This natural frequency can also be expressed as

$$f_n = \frac{\omega_n}{2\pi} \tag{4-11}$$

4.2.1 Dynamic Displacement and Forces

The phase angle ϕ of the bellow as described in the equation below:

$$\phi = tan^{-1}\left[\frac{c_m\omega}{k_m - m_m\omega^2}\right] \tag{4-12}$$

with damping ratio

$$\zeta = \frac{c_m}{c_c} \tag{4-13}$$

and critical viscous damping

$$c_c = 2\sqrt{k_m\, m_m} \tag{4-14}$$

If there is no damping in the system, the phase angle, ϕ, will be 0 degrees if the system is operated below its natural frequency, and 180 degrees if the system is operated above its natural frequency (Rao, 2011). However, there is always damping in a system, and therefore we conclude that the phase angle will be between 0 and 180 degrees, and the system will not be perfectly in or out of phase. This was brought into consideration in the characterisation of the bellow to ensure that all the dissipated energies are accounted for. Where $F_e \cos{(\omega t)}$, in the operational environment of the bellow, can represent the force applied by an oscillating member in the wind, a crank shaft that is driven by a motor or any other mechanical/electrical mechanism.

From Equation (4-5) the force experienced/delivered by each component of the bellow can be seen where the force that the bellow spring component F_{m_k} experiences is

$$F_{m_k} = k_m x \tag{4-15}$$

and the force that the damper component F_{m_c} experiences is

$$F_{m_c} = c_m \dot{x} \tag{4-16}$$

and the force that the mass component F_{m_m} experiences is

$$F_{m_m} = m_m \ddot{x} \tag{4-17}$$

These forces ultimately contribute to the energy that is experienced by the bellow due to the excitation force F_e. The displacement amplitude (Rao, 2011) of the bellow for steady-state conditions is

$$X = \frac{\mathrm{F}_e}{\sqrt{(k_m - m_m\omega^2)^2 + (c_m\omega)^2}} \tag{4-18}$$

4.3 Vibration Energy and Power

An external force will exert work on an object when the object displaces in the direction of the force, therefor from the forces described in Section 2.3.1, the work done by the bellow is (Hibbeler, 2010)

$$dW = F_e dx \tag{4-19}$$

By differentiation over time and integration of dW, from (Rao, 2011) the vibration work done by the bellow in one cycle ΔW_v is

$$\Delta W_\mathrm{v} = \int_0^{\frac{2\pi}{\omega}} F_e \dot{x} \, dt \tag{4-20}$$

By substitution of (4-18) and integration, the vibration work done by the bellow for steady state conditions in one cycle ΔW_v is

$$\Delta W_\mathrm{v} = 0 + c_m \omega X^2 \pi + 0 \tag{4-21}$$

The three terms on the right-hand side of Equation (4-21) represent the work done by the spring component, the damper component, and the mass component of the bellow, respectively. The work done in Equation (4-21) is in Joules per cycle where the power dissipated by the damper is in Joules per second. By calculation of the product of the work done by the damper in one cycle and the frequency, f, of the bellow, the vibration power dissipated by the bellow for steady-state conditions is

$$\mathbb{P}_\mathrm{v} = \frac{1}{2} c_m \omega^2 X^2 \tag{4-22}$$

The power delivered to the bellow is (Hibbeler, 2010)

$$\mathbb{P}(t) = \frac{dW}{dt} \tag{4-23}$$

By substitution of Equation (4-21) into (4-23) and by differentiation of dx/dt (Steward, 2009) the instantaneous power (Hibbeler, 2010) is calculated as

$$\mathbb{P}(t) = F_e \dot{x} \tag{4-24}$$

From Equation (4-5) F_e can be divided into three components such as the spring force, damping force and the mass component. The maximum power delivered by the exciter motors $\mathbb{P}_{\mathrm{v}_{max}}$ is the peak value of $\mathbb{P}$. That means that from (Rao, 2011), $\mathbb{P}$ can also be divided into the spring power $\mathbb{P}_{\mathrm{v}_k}$

$$\mathbb{P}_{\mathrm{v}_k}(t) = F_{m_k}\dot{x} \tag{4-25}$$

and damping power $\mathbb{P}_{\mathrm{v}_c}$

$$\mathbb{P}_{\mathrm{v}_c}(t) = F_{m_c}\dot{x} \tag{4-26}$$

with the mass component $\mathbb{P}_{\mathrm{v}_m}$

$$\mathbb{P}_{\mathrm{v}_m}(t) = F_{m_m}\dot{x} \tag{4-27}$$

A standard sine wave function (Steward, 2009) is described as

$$y(t) = Zsin(t) + C \tag{4-28}$$

and a standard cosine wave function (Steward, 2009) is described as

$$y(t) = Zcos(t) + C \tag{4-29}$$

where Z is the amplitude and C is the mean. The power delivered to the bellow for steady state conditions from Equation (4-25) for the spring power $\mathbb{P}_{\mathrm{v}_k}$ can then be determined in a cyclic manner by

$$\mathbb{P}_{\mathrm{v}_k}(t) = \frac{1}{2}k_m\omega X^2 sin(2\omega t - 2\phi) \tag{4-30}$$

and the damper power $\mathbb{P}_{\mathrm{v}_c}$

$$\mathbb{P}_{\mathrm{v}_c}(t) = \frac{1}{2}c_m\omega^2 X^2 \cos(2\omega t - 2\phi) + \frac{1}{2}c_m\omega^2 X^2 \tag{4-31}$$

and the mass power $\mathbb{P}_{v_m}$

$$\mathbb{P}_{\mathrm{v}_m}(t) = -\frac{1}{2}m_m\omega^3 X^2 \sin(2\omega t - 2\phi) \tag{4-32}$$

From the equations above it is clear that the amplitude values of the power delivered to the spring, damper and mass are $(1/2)\omega X^2 k_m$, $(1/2)c_m\omega^2 X^2$ and $(1/2)m_m\omega^3 X^2$ respectively with the damper power that is the only component that consist of an average power of $(1/2)c_m\omega^2 X^2$. This average power correlates with the vibration power dissipated by the bellow $\mathbb{P}_{\mathrm{v}}$ calculated in Equation (4-22), thus it can be concluded that the only component of the bellow that dissipates energy is the damper.

4.4 Hydraulic Energy Transfer

This hydraulic energy model was used to evaluate the power of the fluid that was transported. The model consists of two water tanks (inlet and discharge) that is inter-connected with a gate valve that closes the circuit to measure the flow rate the system delivers in the discharge tank, three pressure gauges to measure the inlet pressure P_A, discharge pressure P_D and pressure inside the bellow P_B, two gate valves to manipulate the pressure of the pressure gauges along with the bellow shown in Figure 4-2. The model is considered between points A and D, where h_A is the height of the inlet pressure gauge, h_B is the height of the pressure gauge inside the bellow P_B, h_C is the height of the outlet of the bellow and h_D is the height of the outlet pressure gauge. The height of the inlet tank's water level is h_0. The model consists of two in-line spring-type check valves, one at the inlet of the bellow and the other at the outlet of the bellow, as shown in Figure 4-2. Two pipe segments were used for the model, pipe segment 1 with a length l_1 and a diameter D_1 and pipe segment 2 with a length l_2 and a diameter D_2.

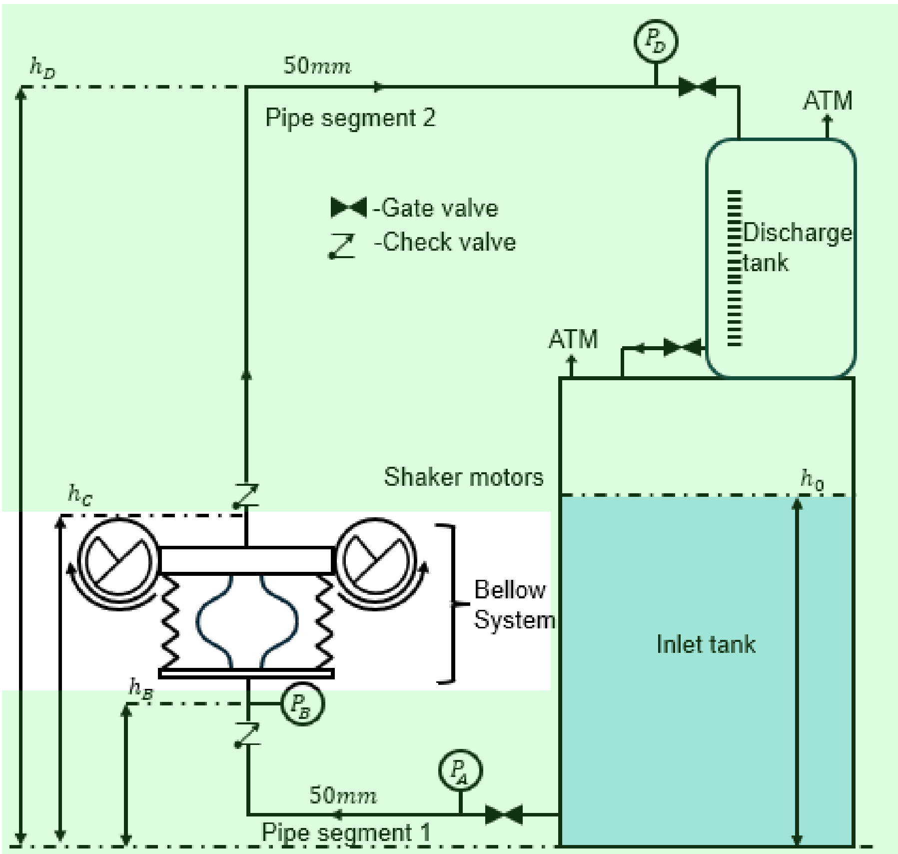

Figure 4-2: In-line rubber bellow schematical experimental setup (Hydraulic energy system highlighted green)

4.4.1 Equivalent Piston Pump

In the current industry, some manufacturers produce a bellow pumping system that acts on a positive displacement principle, similar to a piston pump, for metered pumping. One of these metering pumps are manufactured by GRI pumps and works on a positive displacement principle, where the inlet and outlet to the bellow are separate and installed with poppet valves to ensure that the flow is in one direction (GRI-Pumps, n.d.). From this design, similar to the experimental setup for this study, a flexible, volume changing component with two one-way valves are used to induce flow, where the working principle of flow creation is based on positive displacement pumps.

The system was modelled as a reciprocating piston pump to simplify the calculations,. This is an accurate assumption due to the change in volume that the bellow has in each cycle and the one-way valves that ensure that the flow is limited to one direction. An equivalent piston model of the bellow was developed by determining the volume change per cycle of the bellow.

$$\Delta V = \frac{Q}{f} \tag{4-33}$$

where ΔV is the volume displaced by the bellow per cycle, Q is the average flow rate delivered by the bellow and f is the frequency of the bellow.
From Equation (4-33), the cross-sectional area of the equivalent piston, A_p, can be determined as

$$\mathrm{A_p} = \frac{\Delta V}{2X} \tag{4-34}$$

where the stroke length of the piston is $2X$, two times the displacement amplitude of the bellow. The equivalent piston diameter D_p is

$$D_p = \sqrt{\frac{4A_p}{\pi}} \tag{4-35}$$

By means of the law of continuity (Douglas *et al.*, 1985), the velocity of the fluid in the delivery and suction pipes can be determined as

$$\mathrm{v}_1 = \frac{A_p}{A_1}\dot{x} \quad (4\text{-}36)$$

$$\mathrm{v}_2 = \frac{A_p}{A_2}\dot{x} \quad (4\text{-}37)$$

where v_1 and v_2 is the velocity of the fluid in the suction and delivery pipe respectively, where the cross-sectional area of the suction A_1 and discharge A_2 pipes are

$$A_1 = \frac{\pi D_1^2}{4} \quad (4\text{-}38)$$

$$A_2 = \frac{\pi D_2^2}{4} \quad (4\text{-}39)$$

with D_1 and D_2 the diameters of the suction and delivery pipes respectively. Thus, the acceleration of the fluid in the suction a_1 and delivery a_2 pipes are

$$a_1 = \frac{A_p}{A_1}\ddot{x} \quad (4\text{-}40)$$

$$a_2 = \frac{A_p}{A_2}\ddot{x} \quad (4\text{-}41)$$

4.4.2 Hydraulic Energy Losses

4.4.2.1 Inertia

During each cycle, the fluid comes to a complete standstill twice, once with the suction stroke and once with the delivery stroke. At the beginning of the stroke, an additional head is required to accelerate the fluid that is at a standstill, and an equal opposite head is required to stop the fluid at the end of the stroke (Douglas & Matthews, 1996). The inertia of the fluid does not contribute to the losses in the system because the harmonic motion of the bellow, where the inertia required at the beginning of the stroke being equal to the inertia supplied at the end of the stroke. Although the inertia of the fluid does not contribute to losses, it is, however, important when the suction capabilities of the bellow is evaluated and can give a rating on the maximum reciprocating speed of the bellow before cavitation. The additional head required to overcome the stationary fluid in the suction pipe h_{i_1} and stop the moving fluid in the delivery pipe h_{i_2} are

$$h_{i_1} = -\frac{l_1}{g} a_1 \qquad (4\text{-}42)$$

$$h_{i_2} = -\frac{l_2}{g} a_2 \qquad (4\text{-}43)$$

where l_1 and l_2 are the length of the suction and delivery pipes respectively.

4.4.2.2 Friction

In a reciprocating pumping system, the frictional loss in a pump is a function of the velocity of the fluid, Figure 4-3 shows a simple PV (pressure vs velocity) diagram where the head is illustrated for a single cycle.

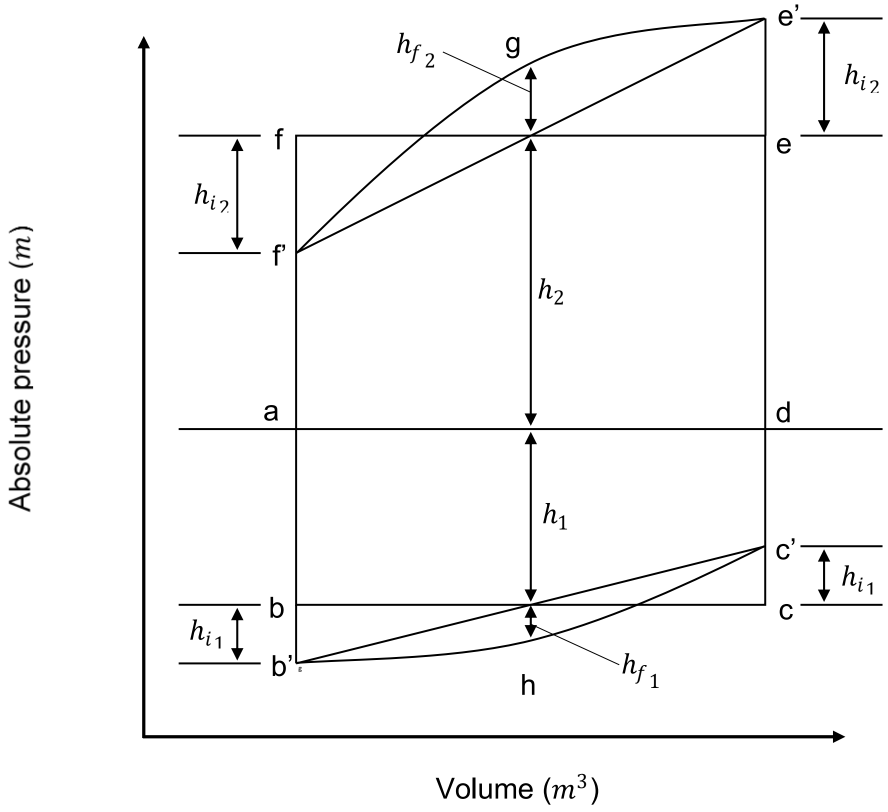

Figure 4-3: Typical PV diagram of a piston reciprocating pump (Douglas & Matthews, 1996)

Where abcd represents the suction stage of the cycle and defa represents the delivery stage. However, the diagram changes with the addition of the inertia head (h_{i_1}, h_{i_2}) and the frictional head loss (h_{f_1}, h_{f_2}) as shown in the figure above. The head loss due to pipe friction at any point in the cycle is calculated from the Darcy equation and depends on the velocity of the fluid (Douglas & Matthews, 1996). The friction head in the suction h_{f_1} and delivery h_{f_2} is

$$h_{f_1} = \frac{4 f_1 l_1 \mathrm{v}_1^2}{D_1 2g} \tag{4-44}$$

$$h_{f_2} = \frac{4 f_2 l_2 \mathrm{v}_2^2}{D_2 2g} \tag{4-45}$$

where f_1 and f_2 is the frictional factors of the suction and delivery pipe respectively. Friction factors can be calculated as in (Douglas et al., 1985).

for $Re_1 < 2100$

$$\mathrm{f}_1 = 16/Re_1 \tag{4-46}$$

for $Re_1 > 2100$

$$\frac{1}{\sqrt{\mathrm{f}_1}} = -1.8 \log\left[\left(\frac{\epsilon/D_1}{3.7}\right)^{1.11} + \frac{6.9}{Re_1}\right] \tag{4-47}$$

for $Re_2 < 2100$

$$\mathrm{f}_2 = 16/Re_2 \tag{4-48}$$

for $Re_2 > 2100$

$$\frac{1}{\sqrt{\mathrm{f}_2}} = -1.8 \log\left[\left(\frac{\epsilon/D_2}{3.7}\right)^{1.11} + \frac{6.9}{Re_2}\right] \tag{4-49}$$

where ϵ is the roughness of the pipe and the Reynolds number for the suction pipe Re_1 and the delivery pipe Re_2 can be determined as

$$Re_1 = \frac{\rho \mathrm{v}_1 D_1}{\mu} \tag{4-50}$$

$$Re_2 = \frac{\rho \mathrm{v}_2 D_2}{\mu} \tag{4-51}$$

where μ is the dynamic viscosity of the fluid transferred and ρ is the density of the fluid. From the Darcy equation it is clear that the frictional head loss is a parabola, the work done against friction is two thirds of the maximum frictional loss (Douglas & Matthews, 1996), thus the power loss due to pipe friction for the suction $\mathbb{P}_{f_1}$ and delivery $\mathbb{P}_{f_2}$ are

$$\mathbb{P}_{f1} = \left(\frac{2}{3}\right)\left(\left(\frac{4f_1 l_1}{2gD_1}\right)\left(\mathrm{v}_{1_{\max}}\right)^2\right)\rho g Q \tag{4-52}$$

$$\mathbb{P}_{f2} = \left(\frac{2}{3}\right)\left(\left(\frac{4f_2 l_2}{2gD_2}\right)\left(\mathrm{v}_{2_{\max}}\right)^2\right)\rho g Q \tag{4-53}$$

where $\mathrm{v}_{1_{max}}$ and $\mathrm{v}_{2_{max}}$ is the maximum fluid velocity in the suction and delivery pipes respectively.

4.4.2.3 One-way valves

To ensure that the energy transferred to the fluid can be determined, two one-way valves are required to ensure that the flow of the fluid is in one direction, this is crucial to accurately determine the energy delivered to the fluid of the system.

In an article on cavitation in reciprocating pumps, valve characteristics are said to have little effect at speeds lower than 100 rpm (Sahoo, 2006). The volumetric efficiency of the reciprocating pump will be higher at a lower operating speed with a higher valve spring constant (Sahoo, 2006). The head required to lift the valve must be determined to take into account the friction head required to open the valve. To measure this head loss, the difference in pressure over the valve should be taken into account.
To determine this loss, the flow rate should be zero and the gate valve at point D, as seen in Figure 4-2 should be fully closed. Figure 4-4 shows a simple example of valve geometry.

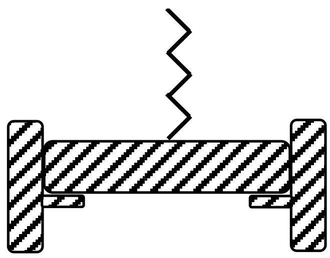

Figure 4-4: One-way valve representation

When the flow is brought to a standstill, it is taken that the fluid has no velocity, which eliminates the friction loss and the inertia head required by the system in relation to the fluid in the pipe system. Thus, the only loss due to head required to lift the valve h_v by analysing the discharge valve is

$$h_v = \frac{P_{C_1} - P_{C_2}}{\rho g} \tag{4-54}$$

where $P_{C_1}$and P_{C_2} is the pressure right before and after the one-way valve at point C as seen in Figure 4-2 and is determined by

$$P_{C_1} = \rho g \left((h_B - h_C) + \left(\frac{P_B}{\rho g} \right) \right) \tag{4-55}$$

$$P_{C_2} = \rho g \left((h_D - h_C) + \left(\frac{P_D}{\rho g} \right) \right) \tag{4-56}$$

4.4.3 Head Delivered by the Bellow System

The internal head delivered by the bellow is a function of all the pressures in the system at a certain time instance and is expressed as (Douglas *et al.*, 1985).

$$h_{in} = h_p + h_{i_1} + h_{i_2} + h_{f_1} + h_{f_2} \tag{4-57}$$

where h_m is the head delivered by the bellow and is

$$h_m = (h_D - h_A) + \left(\frac{P_D - P_A}{\rho g} \right) + \left(\frac{v_2^2 - v_1^2}{2g} \right) + h_v \tag{4-58}$$

4.4.4 Hydraulic Power

The hydraulic power $\mathbb{P}_h$ can be calculated as (Douglas *et al.*, 1985)

$$\mathbb{P}_h = \rho g Q h_m + \mathbb{P}_{f1} + \mathbb{P}_{f2} \tag{4-59}$$

4.5 Vibration Energy Transferred to Fluid

The vibration power delivered by the excitation motors, denoted as $\mathbb{P}_v$, represents the effective mechanical power transmitted to the system after accounting for the electrical and mechanical losses within the motors. This power is determined from the measured displacement amplitudes of the rigid body mass m_m.

The hydraulic power $\mathbb{P}_h$, calculated in Equation (4-59), corresponds to the power imparted to the fluid by the bellows and is obtained from the product of the system's head gain and the volumetric flow rate. In other words, $\mathbb{P}_h$ represents the portion of mechanical energy effectively transferred from the vibrating bellows to the fluid.

The difference between $\mathbb{P}_v$ and $\mathbb{P}_h$ therefore accounts for the mechanical and volumetric losses within the bellows, which define its efficiency. Considering $\mathbb{P}_v$ as the input power and $\mathbb{P}_h$ as the output (transferred) power, the fraction of vibration energy transferred to the fluid, also referred to as the transfer ratio in this study, η_m is given by (Sayers, 1990):

$$\eta_m = \frac{\mathbb{P}_h}{\mathbb{P}_\mathrm{v}} \tag{4-60}$$

4.6 Conclusions

Four mathematical models were constructed to characterise the bellow in terms of the dynamic properties, vibration energy and power, fluid flow power, and fluid energy transfer ratio of the bellow. These mathematical models were computerised and implemented in a MATLAB environment. The implementation of these models is described in Chapter 5.

5 MATLAB Implementation

5.1 Introduction

The four mathematical models described in Chapter 4 were implemented as scrips in a MATLAB environment. The first script was implemented to calibrate and determine the phase angle of the bellow, the second script was to retrieve and plot the data points from the FFT analyser, the third script was implemented to determine the dynamic properties of the bellow. The fourth script was implemented to determine the vibration energy and power of the bellow for steady state, as well as the transient behaviour of the bellow. The fifth script was implemented to determine the flow properties of the bellow, and the sixth script was used to determine the amount of energy transferred to the fluid. These scripts are listed in Appendix B.

5.2 Phase-Angle Calibration of the Bellow System

The flow chart shown in Figure 5-1 describes the script used to determine the phase angle, ϕ, of the bellow. The input data consists of the calibration signals measured by the DI, and the signals measured for each characterisation condition. From the signals, FFT calculations are done, and Equation (4-7) is solved in a MATLAB environment. The MATLAB program is included in Appendix B.

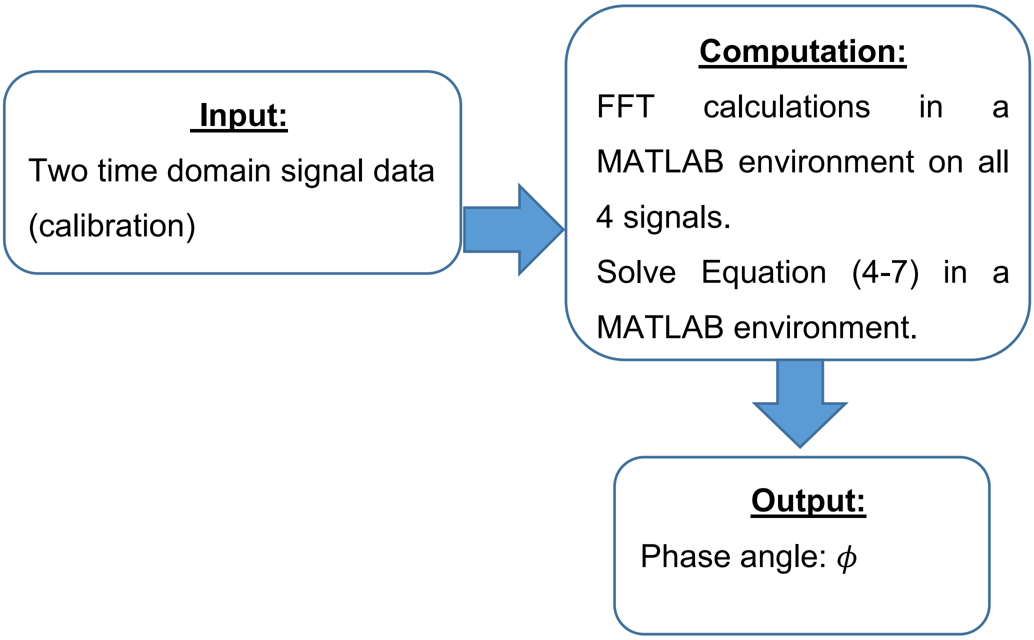

Figure 5-1: Phase angle flow chart

5.3 Dynamic Properties of the Bellow

The flow chart shown in Figure 5-2 describes the MATLAB script based on the mathematical model described in Section 4.2. The input data consists of the equivalent mass m_m that is on top of the bellow, frequency f, phase angle ϕ, the displacement peak X of the vibration and unbalance properties $m_e r_e$ and n. From the input values given, Equations (4-12) and (4-18) were solved simultaneously to determine the dynamic properties k_m and ζ. The MATLAB program is included in Appendix B.

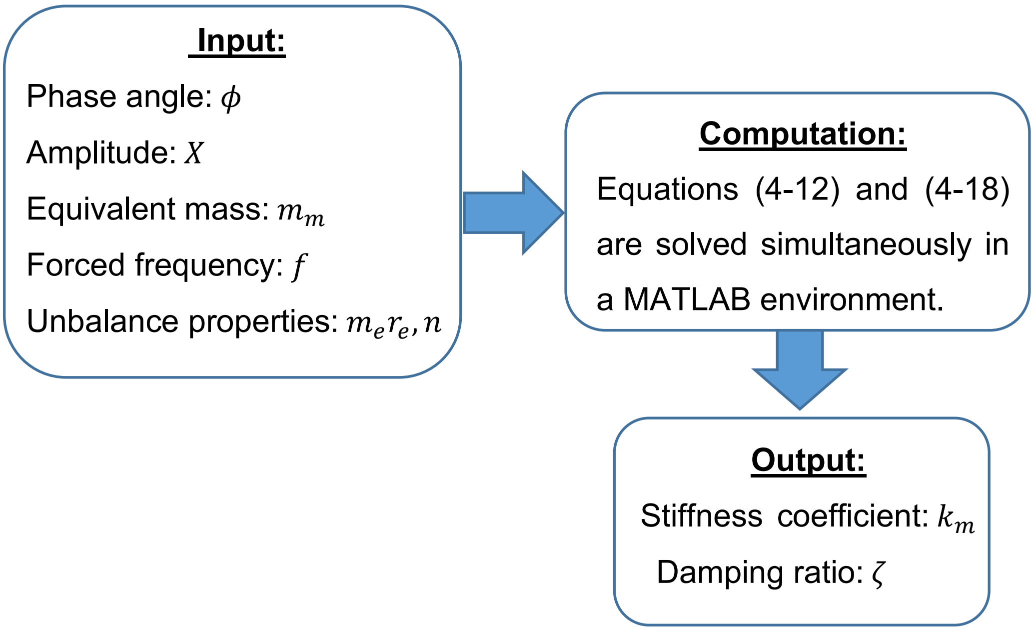

Figure 5-2: Dynamic Properties Flow Chart

5.4 Vibration Energy and Power

5.4.1 Steady State

The flow chart shown in Figure 5-3 describes the MATLAB implementation based on the mathematical model described in Section 4.3 for steady state behaviour of the bellow. The input data consists of the dynamic properties of the bellow, k_m and ζ, the equivalent mass m_m, forced frequency f and unbalance properties $m_e r_e$ and n. Equations (4-21), (4-22), (4-24), (4-25), (4-26) and (4-27) were solved in a MATLAB environment. The MATLAB program is included in Appendix B.

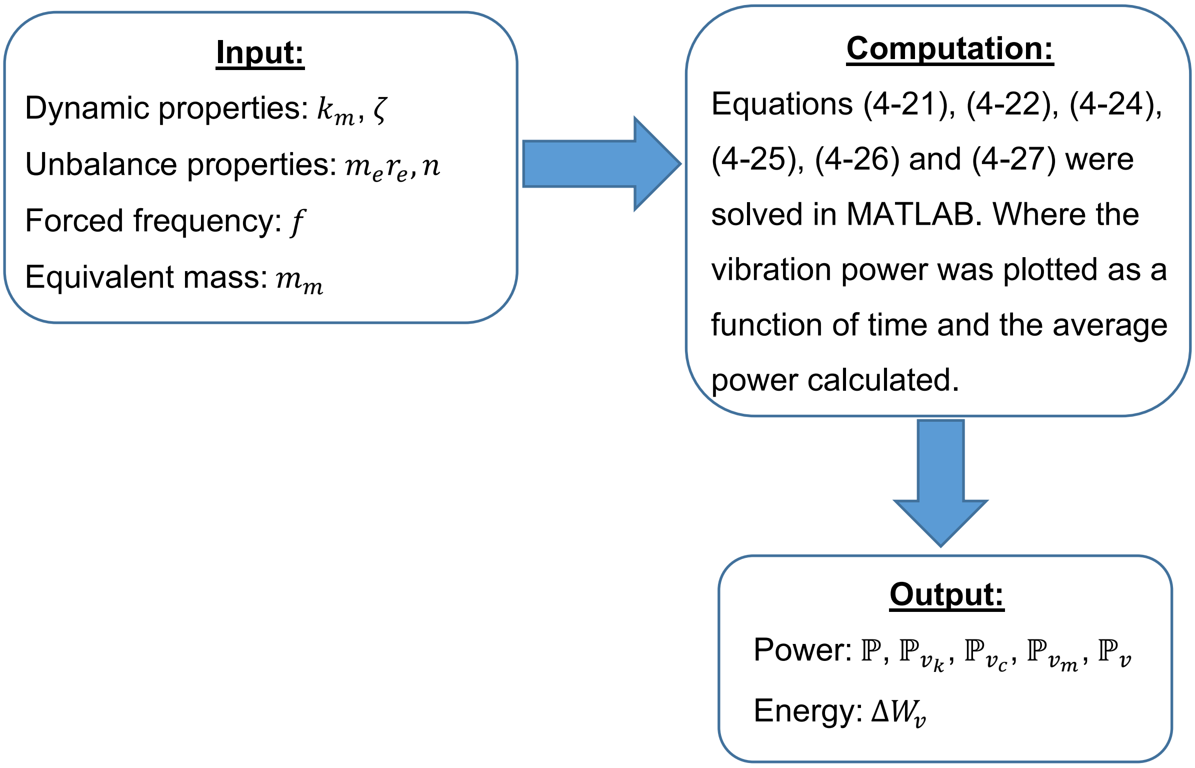

Figure 5-3: Dynamic energy and power flow chart

5.4.2 Start-up Transient Prediction

The flow chart shown in Figure 5-4 describes the MATLAB implementation based on the mathematical model described in Section 4.2, for the transient behaviour of the bellow. The input parameters consist of the rigid body mass m_m, frequency f, unbalance properties $m_e r_e$ and n, bellow stiffness k_m and damping ratio ζ. This computation is done to ultimately determine what the required power is to start up the bellow system. Second-order differential Equation (4-5) is converted to two first-order differential equations. These equations were then solved in a MATLAB environment by numerical integration with $ode23.m$. From this predicted response, the required power to start the bellow system can be solved. Further Equation (4-25), (4-26) and (4-27) were solved to plot the power of each component as described in Chapter 4. The MATLAB program is included in Appendix B.

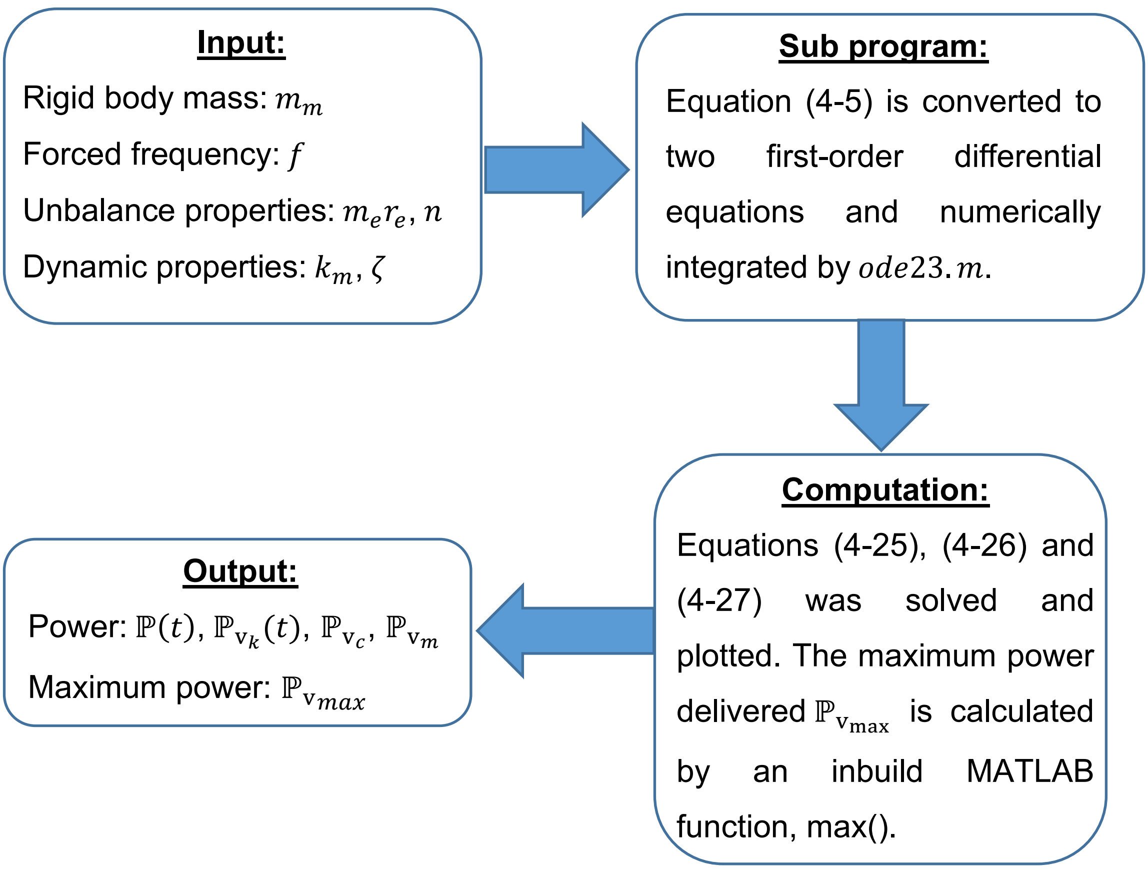

Figure 5-4: Transient prediction flow chart for start-up conditions

5.5 Fluid Flow Power

The flow chart shown in Figure 5-5 describes the MATLAB script based on the mathematical model described in Section 4.4. The input data consists of the flow rate delivered by the bellow, Q, the inlet and outlet pressure gauge values P_A and P_D, fluid density and dynamic viscosity ρ and μ, gravitational constant g, heights of each point in the system as shown in Figure 4-2, h_0, h_A, h_B, h_C and h_D. The length and diameter of suction pipe l_1 and D_1 and the delivery pipe l_2 and D_2. The equations (4-44), (4-45), (4-52), (4-53), (4-54), (4-57), (4-58), and (4-59) were solved in a MATLAB environment to calculate the hydraulic power $\mathbb{P}_h$. The MATLAB program is included in Appendix B.

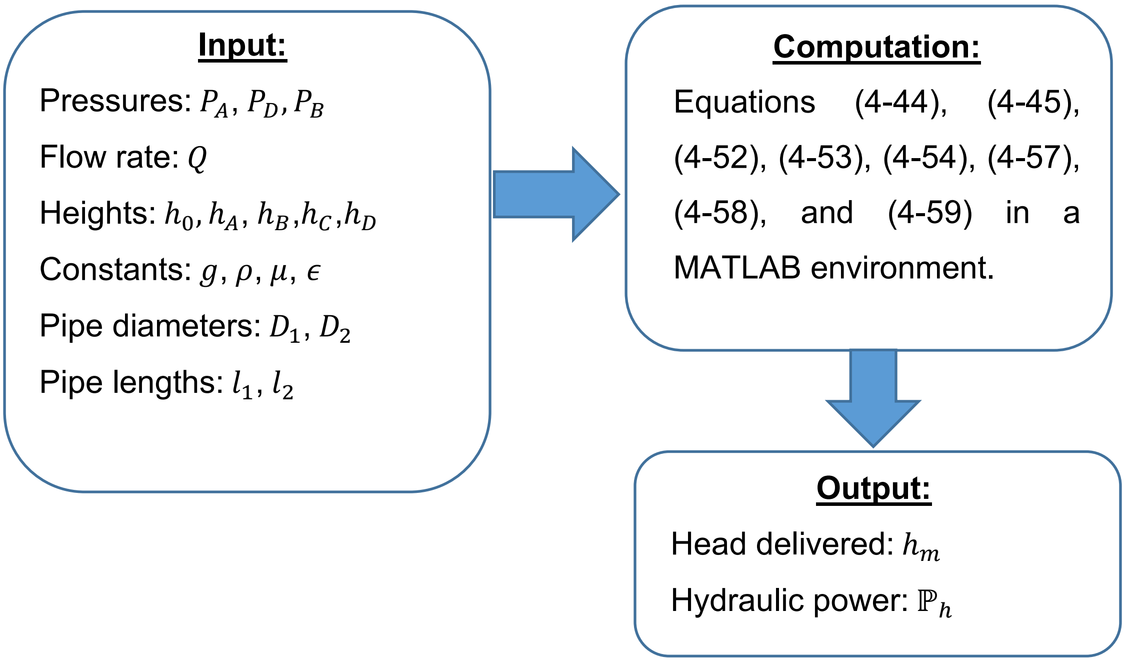

Figure 5-5: Fluid power flow chart

5.6 Energy Transferred to fluid

The flow chart shown in Figure 5-6 describes the MATLAB script based on the mathematical model described in Section 4.5.The input data consists of the hydraulic power delivered by the bellow, $\mathbb{P}_h$, and the vibration power delivered by the excitation motors $\mathbb{P}_v$ for steady state conditions. Equation (4-60) is solved in a MATLAB environment. The MATLAB script is included in Appendix B.

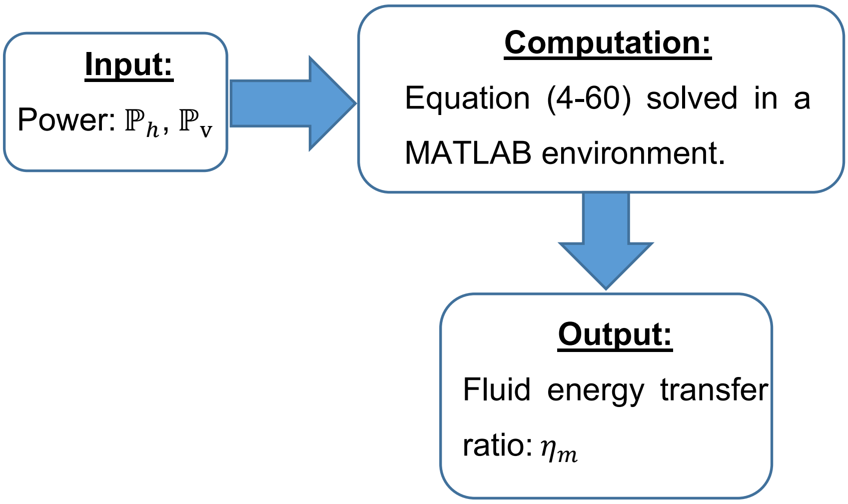

Figure 5-6: Fluid energy transfer ratio flow chart

5.7 Conclusions

The mathematical models described in Chapter 4 were implemented in a MATLAB environment, and the flow charts of these MATLAB scripts were described in Chapter 5. These MATLAB scripts are used to characterise the bellow system that is discussed in Chapter 6.

6 Experimental Results

6.1 Introduction

The dynamic properties of the bellow can be characterized by examining the power and energy that are delivered by the excitation motors to the bellow and the portion of power delivered to the fluid by the bellow. The fluid power transfer was experimentally determined and formed an important characteristic to determine the portion of energy transferred to the fluid, compared to the vibrational energy absorbed by the bellow material and structure. To ensure that the results are consistent and accurate, the flow and pressure had to be stable for two readings in the FFT analyser, where the 3rd reading was used.

Table 6-1 indicates the phase angle calibration results at 100% unbalance, 50% unbalance, and 20% unbalance as described in Section 3.1.

Table 6-1: Phase angle calibration results

n [%]	ϕ_{eik} [Deg]
100	-0.33
50	60.63
20	86.22

6.2 High Frequency Test

6.2.1 Bellow System Dynamic Properties

The dynamic properties of the bellow was primarily characterised by processing the acceleration time response signals measured at each test point. The EC sensor is connected to the transducer that is connected to the Diagnostic Instrument (DI) that plots the signal that represents the distance between the EC sensor and the unbalance mass. The DI plots the acceleration signal, and the EC sensor signal simultaneously. The signals are then analysed in a MATLAB environment to determine the phase angle and dynamic properties. A response signals are shown in Figure 6-1.

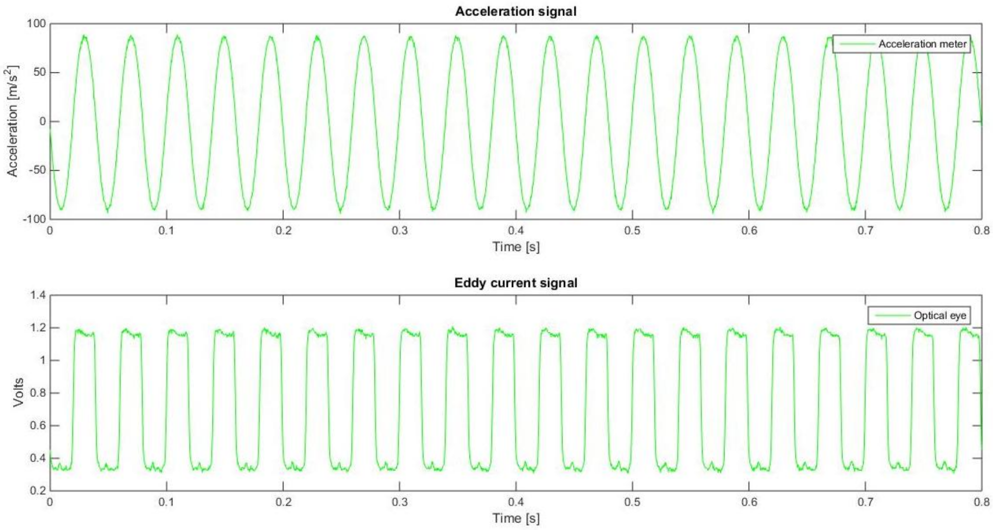

Figure 6-1: Response signals from DI (25 $[Hz]$)

Table 6-2 illustrates the phase angle (ϕ), excitation amplitude (X), stiffness (k_m) and damping ratio (ζ) of the bellow system for each condition of the experimental characterisation at a frequency, f, of 12.5 Hz.

Table 6-2: Bellow dynamic properties @ 12.5 Hz

n		50%				100%			
P_A [kPa]	P_D [kPa]	ϕ [Deg]	X [mm]	k_m [N/mm]	ζ [-]	ϕ [Deg]	X [mm]	k_m [N/mm]	ζ [-]
0	0	-19.52	1.9	84.5	0.28	-10.69	4.7	132.3	0.098
0	20	-22.88	2.6	170.8	0.16	-20.59	4.6	138.9	0.18
0	35	-19.33	2.8	174.8	0.13	-17.83	4.9	147.7	0.15
0	50	-19.45	2.9	182.0	0.12	-16.29	5.0	151.8	0.13
-20	0	-17.94	2.6	164.8	0.13	-18.49	4.5	134.0	0.17
-30	0	-17.98	2.6	164.7	0.13	Cavitation			

Table 6-3 illustrates the phase angle, excitation amplitude, stiffness and damping ratio of the bellow system for each condition of the experimental characterisation at a frequency, f, of 18.75 $[Hz]$.

Table 6-3: Bellow dynamic properties @ 18.75 Hz

n		50%				100%			
P_A [kPa]	P_D [kPa]	ϕ [Deg]	X [mm]	k_m [N/mm]	ζ [-]	ϕ [Deg]	X [mm]	k_m [N/mm]	ζ [-]
0	0	-10.23	1.8	128.7	0.19	-6.88	3.7	163.7	0.11
0	20	-6.22	1.9	169.3	0.094	-7.78	3.8	170.8	0.12
0	35	No flow				-6.10	3.8	172.9	0.09
0	50	No flow				-6.32	3.8	177.4	0.092
-20	0	Cavitation				-6.21	3.7	153.5	0.10
-30	0	Cavitation				-6.20	3.7	159.6	0.098

Table 6-4 illustrates the phase angle, excitation amplitude, stiffness and damping ratio of the bellow system for each condition of the experimental characterisation at a frequency, f, of 25 $[Hz]$.

Table 6-4: Bellow dynamic properties @ 25 Hz

n		50%				100%			
P_A [kPa]	P_D [kPa]	ϕ [Deg]	X [mm]	k_m [N/mm]	ζ [-]	ϕ [Deg]	X [mm]	k_m [N/mm]	ζ [-]
0	0	-4.73	1.6	133.2	0.12	-7.25	3.3	789.3	0.04
0	20	-4.98	1.7	141.5	0.13	-5.79	3.3	790.7	0.03
0	35	No flow				-5.01	3.3	789.8	0.026
0	50	No flow				-5.47	3.4	794.0	0.027
-20	0	Cavitation				-5.98	3.3	793.4	0.03
-40	0	Cavitation				-9.2	3.3	782.8	0.05

The MATLAB script used to determine the dynamic properties is included in Appendix B.

6.2.2 Vibration Energy and Power

The power and energy elements of the bellow was calculated to illustrate the vibrational energy distribution as it is dissipated in the bellow system. Note that this section only describes the mechanical vibrational aspect of the energy and that the energy transferred to the fluid was handled separately. All computations were done in a MATLAB environment, included in Appendix B.

The power of the below system was calculated using Equations (4-24), (4-25), (4-26) and (4-27) with the instantaneous power of each vibration system element plotted over time and is shown in Figure 6-2. The red line represents the damping power of the system, the light blue line represents the mass component of the vibration power, the dark blue line represents the spring component of the vibration power, and the green line represents the overall vibration power. The averages of each power curve are also plotted, where the light blue and dark blue lines have an average of zero, indicating that the average power of the spring and mass is zero. The green and red lines had the same average, indicating that the average damping power equals the average overall vibrational power, which was higher than zero.

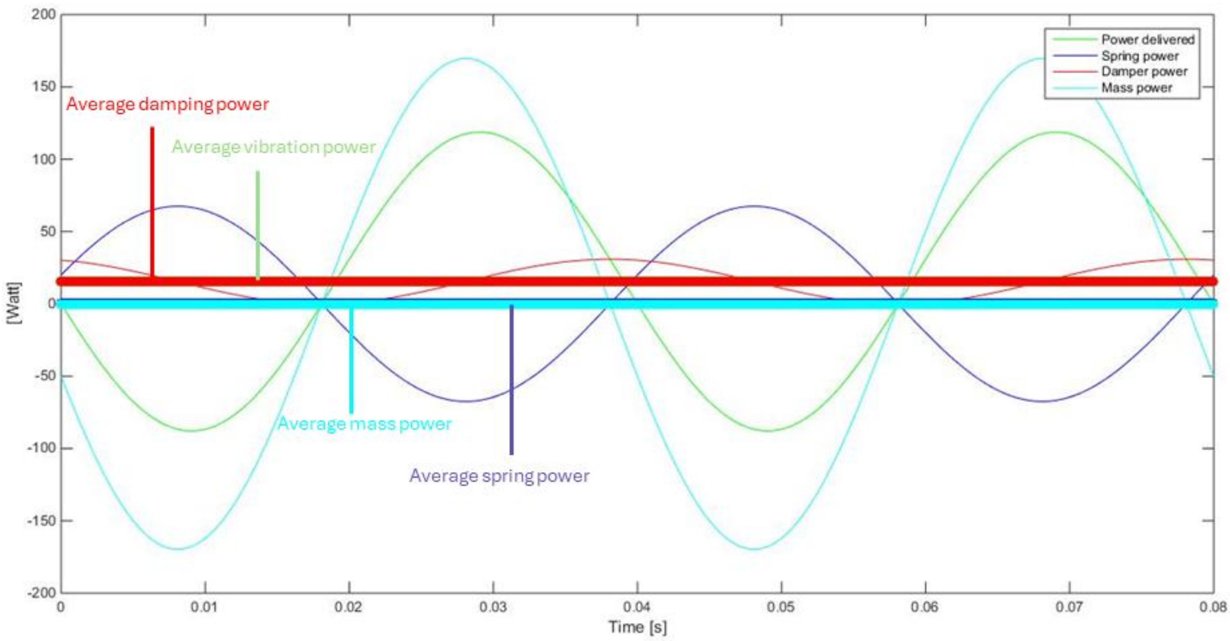

Figure 6-2: Power plot

From Figure 6-2, the nett power delivered to the spring component and the mass component is zero, where the average power dissipated by the damping component and the average power delivered is equal, at a value greater than zero. The MATLAB script used to determine and plot the vibration power is included in Appendix B.

6.2.2.1 Steady state

The vibration energy that was delivered to the bellow for a complete cycle and the vibration power under steady state conditions were calculated. Table 6-5 illustrates the vibration energy and power of the bellow system for each condition of the experimental characterisation at a frequency, f, of 12.5 $[Hz]$.

Table 6-5: Bellow system energy and power @ 12.5 Hz

n		50%		100%	
P_A [kPa]	P_D [kPa]	ΔW_v [J]	$\mathbb{P}_v$ [W]	ΔW_v [J]	$\mathbb{P}_v$ [W]
0	0	1.04	13.04	2.93	36.57
0	20	1.73	21.67	5.44	68.04
0	35	1.54	19.31	5.02	62.77
0	50	1.62	20.20	4.73	59.12
-20	0	1.37	17.18	4.87	60.82
-30	0	1.38	17.20	Cavitation	

Table 6-6 illustrates the vibration energy and power of the bellow for each condition of the experimental characterisation at a frequency, f, of 18.75 [Hz].

Table 6-6: Bellow system energy and power @ 18.75 Hz

n		50%		100%	
P_A [kPa]	P_D [kPa]	ΔW_v [J]	$\mathbb{P}_v$ [W]	ΔW_v [J]	$\mathbb{P}_v$ [W]
0	0	1.18	22.20	3.40	63.74
0	20	0.78	14.55	3.88	72.66
0	35	No flow		3.06	57.45
0	50	No flow		3.19	59.86
-20	0	Cavitation		3.02	56.69
-30	0	Cavitation		3.05	57.13

Table 6-7 illustrates the vibration energy and power of the bellow for each condition of the experimental characterisation at a frequency, f, of 25 [Hz].

Table 6-7: Bellow system energy and power @ 25 Hz

n		50%		100%	
P_A [kPa]	P_D [kPa]	ΔW_v [J]	$\mathbb{P}_v$ [W]	ΔW_v [J]	$\mathbb{P}_v$ [W]
0	0	0.92	22.94	5.65	141.15
0	20	0.97	24.28	4.53	113.36
0	35	No flow		3.93	98.18
0	50	No flow		4.04	100.96
-20	0	Cavitation		4.71	117.64
-40	0	Cavitation		7.05	176.26

6.2.2.2 Transient behaviour

For the transient behaviour, an operating condition was characterised experimentally to compare the results with that of the numerical integration in a MATLAB environment. This allowed the determination of the dynamic properties of the bellow during transient conditions. Figure 6-3 shows the experimental acceleration signal of the bellow during transient behaviour. The acceleration amplitude of the system starts at zero and increases with each cycle. After 4 cycles the maximum acceleration was achieved.

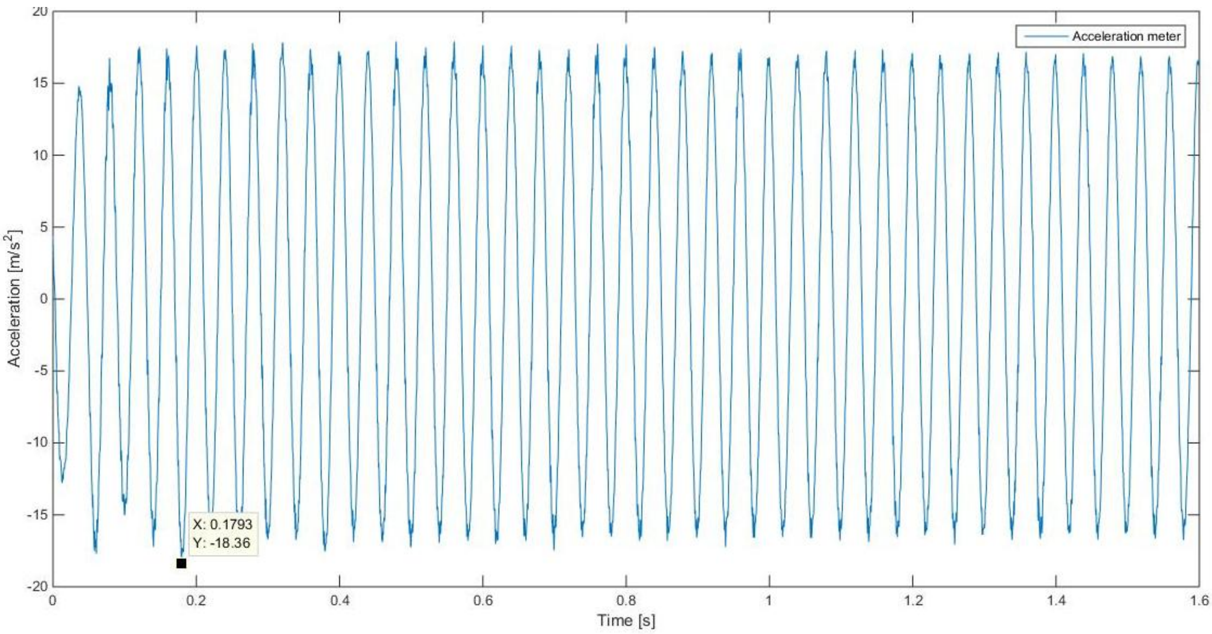

Figure 6-3: Transient acceleration signal (experimental)

Figure 6-4 shows the predicted transient acceleration, calculated by the numerical integration model in MATLAB.

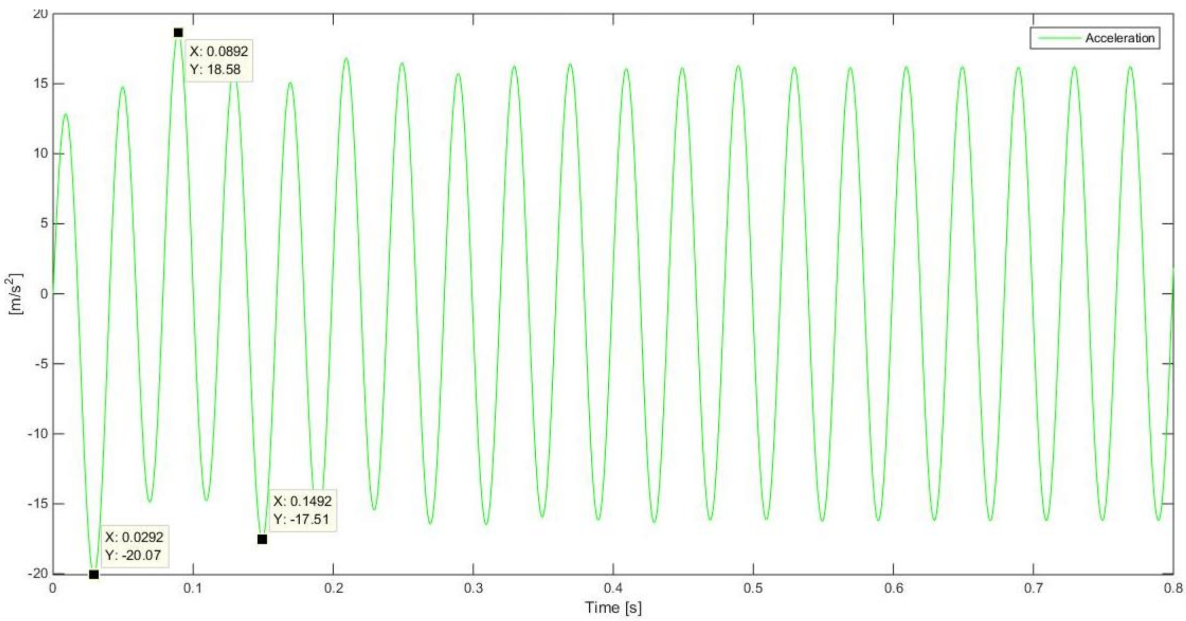

Figure 6-4: Numerical integration acceleration signal

Figure 6-5 shows the predicted transient vibration power, calculated by the numerical integration model in MATLAB.

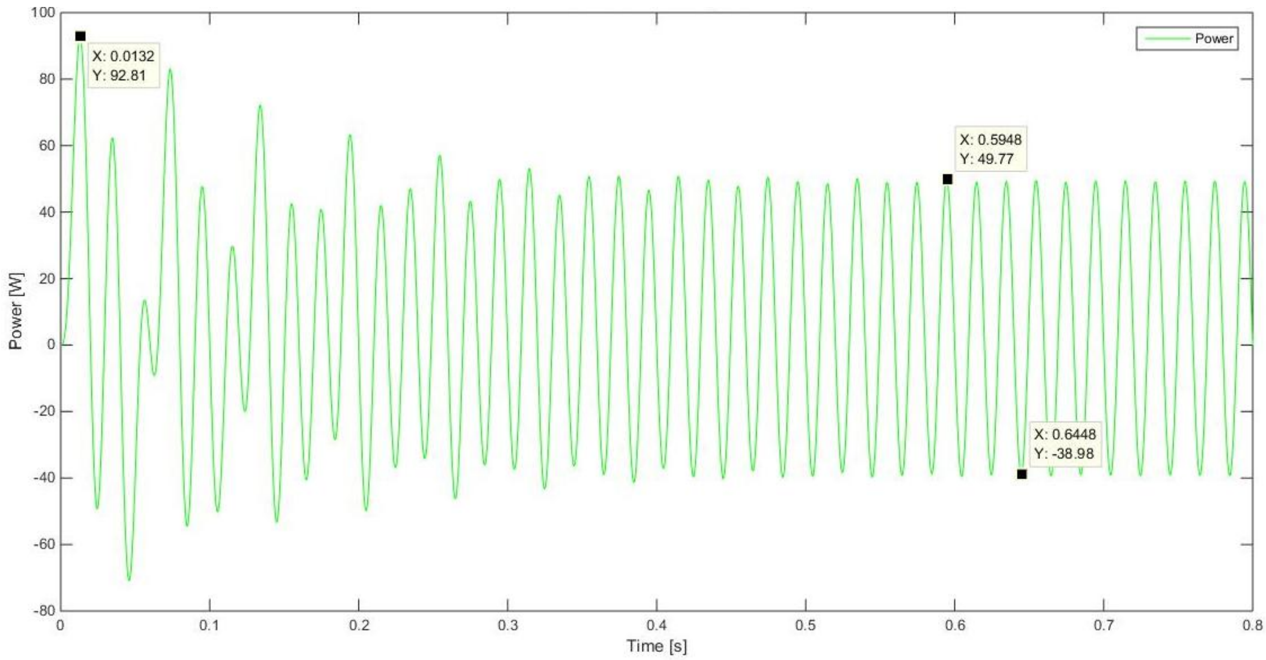

Figure 6-5: Numerical integration vibration power signal

Figure 6-6 shows the predicted transient vibration power for each component of the system, calculated by the numerical integration model in MATLAB. The equivalent power, spring power, damping power and mass power signals are shown.

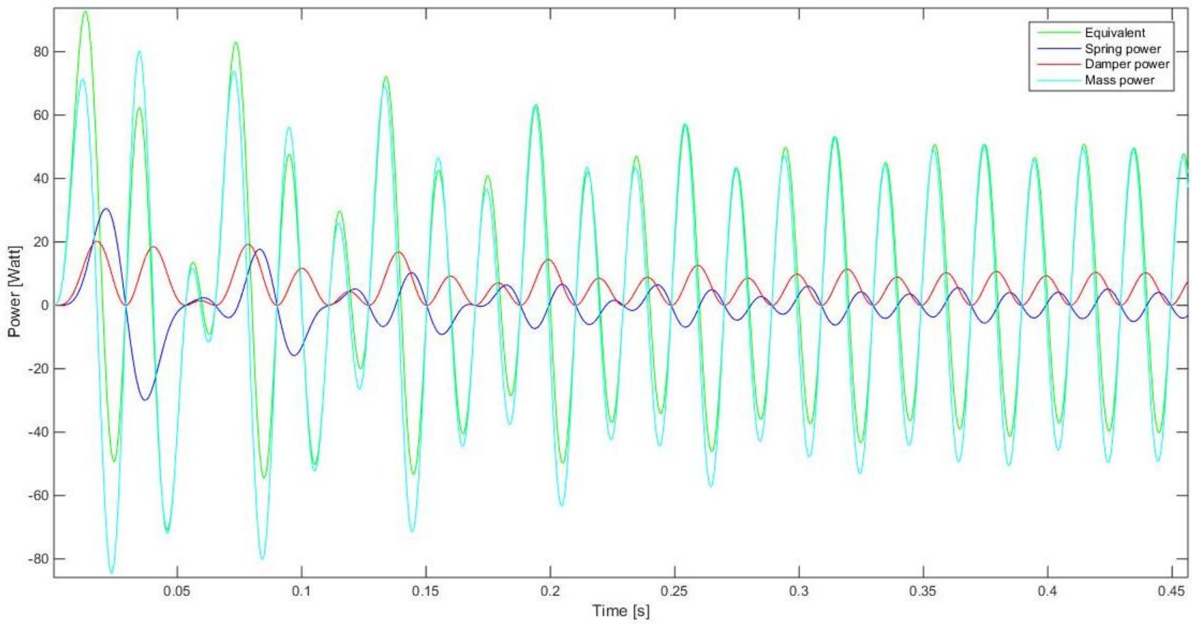

Figure 6-6: Numerical integration vibration power signals for each component

Table 6-8 illustrates the dynamic properties, steady state vibration energy and power and the transient properties of the bellow at 20% unbalance and 25 Hz.

Table 6-8: Dynamic properties, energy, power, and transient properties @ 25 Hz

n		20%								
P_A [kPa]	P_D [kPa]	ϕ [Deg]	X [mm]	k_p [N/mm]	ζ [-]	ΔW_v [J]	$\mathbb{P}_v$ [W]	$\ddot{x}_{actual}$ [m/s^2]	$\ddot{x}_{predict}$ [m/s^2]	$\mathbb{P}_{max}$ [W]
0	0	-6.53	0.66	131.81	0.17	0.20	5.04	18.36	20.07	92.80

The transient behaviour is important since the largest amount of vibrational energy is transferred during start-up and stop conditions. From the table above it is seen that the predicted value, 20.07 m/s^2, of the transient behaviour correlates well with the measured response, 18.36 m/s^2.

6.2.3 Flow Properties

The layout of the flow system of the bellow is shown in Figure 4-2. The values of the vacuum gauge, P_A, and pressure gauge, P_D, was taken along with the maximum pressure reading of the bellow pressure gauge, P_B, and the flow rate of the fluid was determined by means of a stopwatch and the reading the volume of water displaced in that time. The discharge tank consists of a volume indicator that was graded in 250 ml intervals. To ensure that the readings are accurate and repeatable, the minimum required volume of water pumped to determine the flow rate was at least 7 litres. The stopwatch used to time the fluid flow rate is shown in Figure 6-7.

Figure 6-7: Stopwatch timer

Table 6-9 illustrate the flow properties of the bellow for each condition of the experimental characterisation at a frequency, f, of 12.5 Hz.

Table 6-9: Flow properties @ 12.5 Hz

n		50%			100%		
P_A [kPa]	P_D [kPa]	Q [l/s]	h_m [m]	$\mathbb{P}_h$ [W]	Q [l/s]	h_m [m]	$\mathbb{P}_h$ [W]
0	0	0.35	1.06	3.66	0.42	6.47	26.53
0	20	0.12	3.09	3.54	0.34	8.50	27.99
0	35	0.07	4.62	3.05	0.17	10.02	17.15
0	50	0.03	6.15	1.72	0.14	11.55	15.36
-20	0	0.04	3.25	1.13	0.20	8.65	16.89
-30	0	0.03	4.27	1.44	Cavitation		

Table 6-10 illustrate the flow properties of the bellow for each condition of the experimental characterisation at a frequency, f, of 18.75 Hz.

Table 6-10: Flow Properties @ 18.75 Hz

n		50%			100%		
P_A [kPa]	P_D [kPa]	Q [l/s]	h_m [m]	$\mathbb{P}_h$ [W]	Q [l/s]	h_m [m]	$\mathbb{P}_h$ [W]
0	0	0.17	4.21	6.92	0.16	6.46	10.29
0	20	0.04	6.25	2.75	0.09	8.50	7.32
0	35	No flow			0.06	10.02	6.28
0	50	No flow			0.04	11.55	4.75
-20	0	Cavitation			0.14	8.65	11.74
-30	0	Cavitation			0.03	9.67	2.45

Table 6-11 illustrate the flow properties of the bellow for each condition of the experimental characterisation at a frequency, f, of 25 Hz.

Table 6-11: Flow properties @ 25 Hz

n		50%			100%		
P_A [kPa]	P_D [kPa]	Q [l/s]	h_m [m]	$\mathbb{P}_h$ [W]	Q [l/s]	h_m [m]	$\mathbb{P}_h$ [W]
0	0	0.08	3.70	3.05	0.23	4.73	10.83
0	20	0.07	5.74	3.72	0.03	6.76	2.06
0	35	No flow			0.01	8.29	0.95
0	50	No flow			0.002	9.82	0.24
-20	0	Cavitation			0.15	6.92	10.01
-40	0	Cavitation			0.22	8.95	19.35

6.2.4 Fluid Energy Transfer Ratio of the Bellow System

The fluid energy transfer ratio η_m of the bellow in terms of hydraulic power delivered, was calculated at a frequency of 12.5, 18.75, and 25 Hz and resulting values are illustrated in Table 6-12, Table 6-13, and Table 6-14 respectively.

Table 6-12: Fluid energy transfer ratio @ 12.5 Hz

n		50%	100%
P_A [kPa]	P_D [kPa]	η_m [%]	η_m [%]
0	0	28.07	72.55
0	20	16.34	41.14
0	35	15.79	27.32
0	50	8.51	25.98
-20	0	6.58	27.77
-30	0	8.37	Cavitation

Table 6-13: Fluid energy transfer ratio @ 18.75 Hz

n		50%	100%
P_A [kPa]	P_D [kPa]	η_m [%]	η_m [%]
0	0	31.17	16.14
0	20	18.90	10.07
0	35	No flow	10.93
0	50	No flow	7.94
-20	0	Cavitation	20.71
-30	0	Cavitation	4.29

Table 6-14: Fluid energy transfer ratio @25 Hz

n		50%	100%
P_A [kPa]	P_D [kPa]	η_m [%]	η_m [%]
0	0	13.30	7.67
0	20	15.32	1.82
0	35	No flow	0.97
0	50	No flow	0.24
-20	0	Cavitation	8.51
-30	0	Cavitation	10.98

From the results obtained it was clear that the fluid energy transfer ratio was greater at lower frequencies, and the vibration power was smaller at lower frequencies. The damping coefficient of the vibration rubber bellow was also higher at lower frequencies. Thus, the need to characterise the bellow system at lower frequencies than what can be generated by the unbalance motors arose.

Subsequently, the bellow system was also tested at lower frequencies with a higher amplitude by using an alternative excitation setup as is now discussed in Section 6.3.

6.3 Low Frequency Test

6.3.1 Introduction

The experimental setup was modified to be able to characterise the bellow system at lower frequencies. By changing the excitation force source to a crank shaft that was driven through a reduction gearbox, the desired low frequency was obtained. Figure 6-8 shows the modified experimental setup.

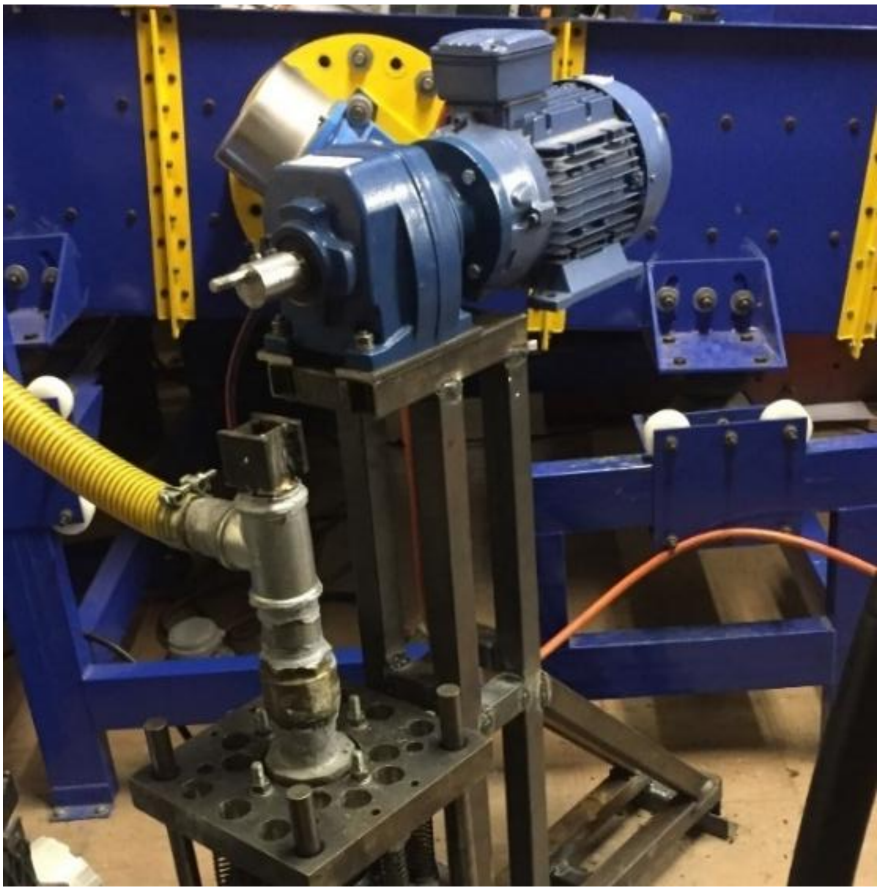

Figure 6-8: Motor-gearbox-crankshaft experimental setup

A HBM U2A tension/compression load cell with a full bridge strain-gauge 6-wire configuration (HBM, 2017) was used to measure the force that was transferred to the bellow system. Figure 6-9 shows the load cell connection between the crankshaft and the bellow system. The top mass was still guided by the linear bearings and guide shafts as used in the previous setup to ensure that the vibration of the system remains vertical.

Figure 6-9: Load cell connection

As seen in Figure 6-10 the only difference when compared with the high frequency mathematical models discussed in Chapter 4, was that the excitation force $F_e(t)$ comprised of one source. Thus, the existing mathematical models were still applicable.

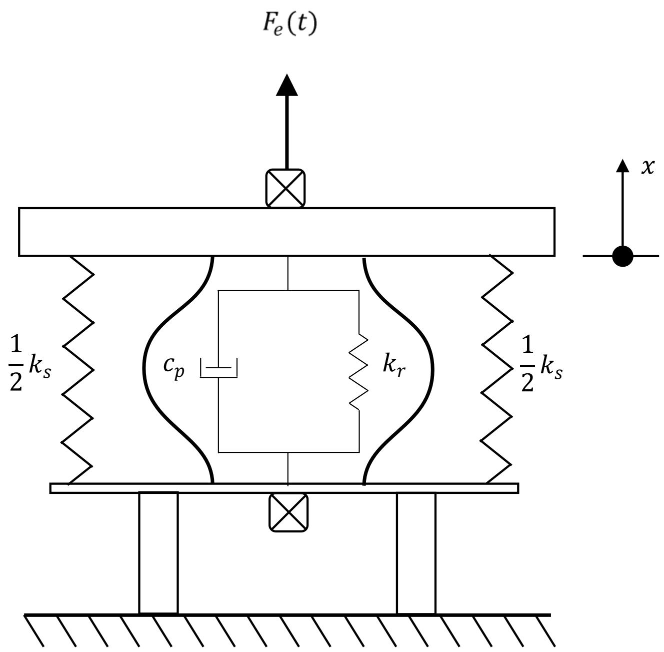

Figure 6-10: Low frequency single degree of freedom model

Section 6.3.2 describes how the load cell's read-out is calibrated to allow accurate measurements of the force transferred to the bellow system.

6.3.2 Excitation Force Calibration

The voltage signal supplied by the load cell is too low for the FFT Analyser to accurately measure a signal. To amplify the signal, a load cell read-out, as seen in Figure 6-11, was used. The analogue signal was then connected to one of the channels of the FFT Analyser.

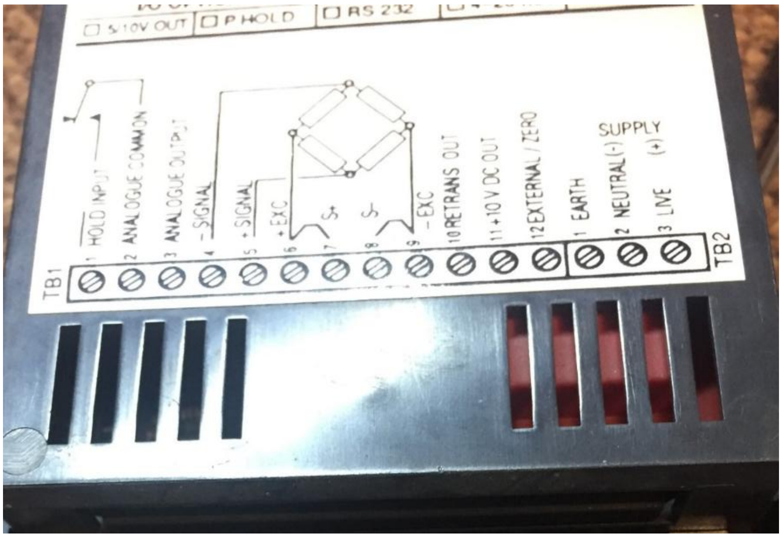

Figure 6-11: Load cell read-out

To calibrate the load cell, the difference in voltage of the signal supplied to the FFT analyser due to the change in load applied was determined. Therefore, five different loads were applied to the load cell and the difference in signal voltage was determined. Figure 6-12 shows the mass of the steel blocks used for the load cell calibration.

Figure 6-12: Mass measurements of weights

Figure 6-13 shows the zero-load condition of the load cell calibration where the only mass on the load cell was that of the strap used with a shackle.

Figure 6-13: Zero load condition

Figure 6-14 shows how the calibration of the load cell was done at different loads.

Figure 6-14: Calibration of load cell at 21.50 kg

Table 6-15 illustrates the signal voltage at different loads.

Table 6-15: Load-cell calibration results

Load kg	Signal output mV
"Zero"	43.39
21.50	47.80
24.50	50.30
43.02	54.47
46.02	55.11

The linear correlation between the load and the signal output, as illustrated in Table 6-15, was determined by means of a MATLAB build in correlation evaluator. Table 6-16 illustrates the correlation calculation results.

Table 6-16: Load-cell correlation results

Correlation variable	Result
SSE	1,557
R^2	0,9835
R^2 adjusted	0,978
RMSE	0,7205
Linear model	$f(x) = p1x + p2$
$p1$	0,2582
$p2$	43,23

.

From the results it is clear that the coefficient of determination, R^2, and the adjusted R^2 is a good fit for this linear curve where the Sum of Squares due to Error (SSE) and the Root Mean Squared Error (RMSE) is a low value relative to the magnitude of the voltage output (less than 4%). Thus, the linear fit is assumed to be accurate and correct. As seen in Table 6-16, the straight-line equation from the curvature fit is

$$SO = 0.2582L + 43.23 \tag{6-1}$$

Where SO and L is the signal output voltage and applied load respectively. The gradient is 0.2582, this value is used to determine the excitation force that the crank shaft will transfer to the bellow system. From Equation (6-1), the excitation force can be determined as

$$F_e = \left(\frac{SP}{0.2582} \times 9.81\right) \sin{(\omega t)} \tag{6-2}$$

Where SP is the amplitude of the signal obtained from the load cell read-out. The force amplitude, F_e, can be determined as

$$\mathrm{F}_e = \frac{SP}{0.2582} \times 9.81 \tag{6-3}$$

Thus, the remaining mathematical models are still applicable.

The excitation force amplitude (F_e) of the bellow system was calculated at the different pressure differentials at 2.5, 3.5 and 5 Hz and are illustrated in Table 6-17, Table 6-18 and Table 6-19 respectively.

Table 6-17: Low frequency excitation force @ 2.5 Hz

P_A [kPa]	P_D [kPa]	F_e [N]
0	20	1412.5
0	35	1529.6
0	50	1457.8
-20	0	1306.4
-30	0	1379.4

Table 6-18: Low frequency excitation force @ 3.5 Hz

P_A [kPa]	P_D [kPa]	F_e [N]
0	0	961.36
0	20	1137.3
0	50	1181.5
-30	0	1012.1

Table 6-19: Low frequency excitation force @ 5 Hz

P_A [kPa]	P_D [kPa]	F_e [N]
0	0	757.92
0	20	853.58

6.3.3 Dynamic Properties (Low Frequency)

The rubber bellow was investigated in terms of the dynamic properties present at each measurement taken. The load cell was connected to the bellow as shown in Figure 6-9, the signal delivered by the load cell was then sent to a load cell readout to amplify the signal that delivered an analogue voltage signal to the FFT Analyser. The analyser plotted the acceleration signal and the load cell signal simultaneously. The signals were then analysed in a MATLAB environment to determine the phase angle and dynamic properties. An example of the response signals is shown in Figure 6-15.

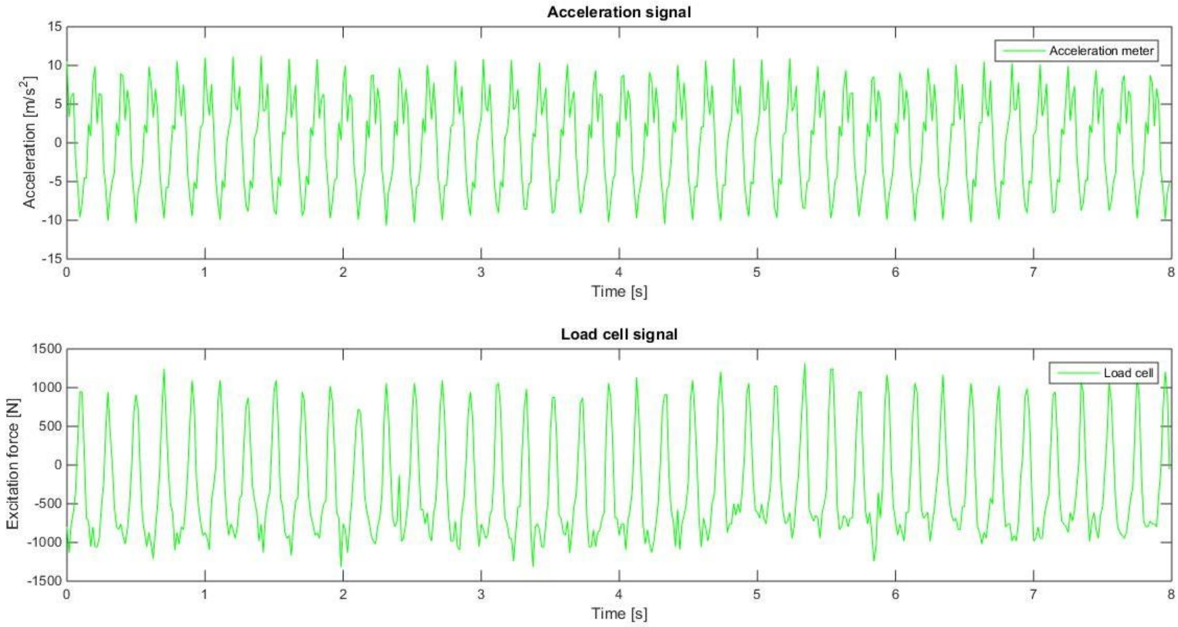

Figure 6-15: Response signal example from Analyser

Table 6-20 illustrates the dynamic properties of the bellow for each condition of the low frequency experimental characterisation at a frequency, f, of 2.5 Hz.

Table 6-20: Dynamic Properties @ 2.5 Hz

P_A [kPa]	P_D [kPa]	ϕ [Deg]	X [mm]	k_p [N/mm]	ζ [-]
0	20	17.80	7.3	191.7	0.82
0	35	15.61	6.9	220.5	0.77
0	50	14.89	7.1	205.1	0.70
-20	0	19.29	7.5	170.5	0.84
-30	0	17.09	7.7	177.09	0.75

Table 6-21 illustrates the dynamic properties of the bellow for each condition of the low frequency experimental characterisation at a frequency, f, of 3.5 Hz.

Table 6-21: Dynamic properties @ 3.5 Hz

P_A [kPa]	P_D [kPa]	ϕ [Deg]	X [mm]	k_p [N/mm]	ζ [-]
0	0	13.83	7.8	132.98	0.35
0	20	11.44	8.2	149.33	0.31
0	50	10.37	6.5	193.02	0.32
-30	0	12.22	8.5	130.41	0.30

Table 6-22 illustrates the dynamic properties of the bellow for each condition of the low frequency experimental characterisation at a frequency, f, of 5 Hz.

Table 6-22: Dynamic properties @ 5 Hz

P_A [kPa]	P_D [kPa]	ϕ [Deg]	X [mm]	k_p [N/mm]	ζ [-]
0	0	14.85	7.0	132.44	0.23
0	20	18.60	6.2	156.79	0.33

6.3.4 Energy and Power (Low Frequency)

Table 6-23 illustrates the vibration energy and power of the bellow for each condition of the experimental characterisation at a frequency, f, of 2.5, 3.5 and 5 Hz.

Table 6-23: Vibration energy and power @ 2.5 Hz

P_A [kPa]	P_D [kPa]	ΔW_v [J]	$\mathbb{P}_v$ [W]
0	20	9.87	24.67
0	35	8.92	22.29
0	50	8.36	20.90
-20	0	10.21	25.53
-30	0	9.86	24.66

Table 6-24 illustrates the vibration energy and power of the bellow for each condition of the experimental characterisation at a frequency, f, of 3.5 Hz.

Table 6-24: Vibration energy and power @ 3.5 Hz

P_A [kPa]	P_D [kPa]	ΔW_v [J]	$\mathbb{P}_v$ [W]
0	0	5.63	19.72
0	20	5.81	20.34
0	50	4.32	15.12
-30	0	5.69	19.90

Table 6-25 illustrates the vibration energy and power of the bellow for each condition of the experimental characterisation at a frequency, f, of 5 Hz.

Table 6-25: Vibration energy and power @ 5 Hz

P_A [kPa]	P_D [kPa]	ΔW_v [J]	$\mathbb{P}_v$ [W]
0	0	4.25	21.26
0	20	5.34	26.72

6.3.5 Flow Properties (Low Frequency)

The fluid model has not changed, and the same mathematical model used in Chapter 4 was applicable. The bellow system remains unchanged. Table 6-26 illustrates the flow properties of the bellow system for each condition of the experimental characterisation at a frequency, f, of 2.5, 3.5 and 5 Hz.

Table 6-26: Flow properties @ 2.5 Hz

P_A [kPa]	P_D [kPa]	Q [l/s]	h_p [m]	$\mathbb{P}_h$ [W]
0	20	0.149	2.80	4.09
0	35	0.089	4.33	3.76
0	50	0.082	5.86	4.69
-20	0	0.210	2.92	6.03
-30	0	0.020	3.94	7.93

Table 6-27 illustrates the flow properties of the bellow system for each condition of the experimental characterisation at a frequency, f, of 3.5 Hz.

Table 6-27: Flow properties @ 3.5 Hz

P_A [kPa]	P_D [kPa]	Q [l/s]	h_p [m]	$\mathbb{P}_h$ [W]
0	0	0.352	0.77	2.70
0	20	0.194	2.80	5.34
0	50	0.120	5.86	5.88
-30	0	0.339	3.94	13.15

Table 6-28 illustrates the flow properties of the bellow system for each condition of the experimental characterisation at a frequency, f, of 5 Hz.

Table 6-28: Flow properties @ 5 Hz

P_A [kPa]	P_D [kPa]	Q [l/s]	h_p [m]	$\mathbb{P}_h$ [W]
0	0	0.541	0.78	4.29
0	20	0.423	2.81	11.74

6.3.6 Fluid Energy Transfer Ratio (Low Frequency)

Table 6-29 illustrates the fluid energy transfer ratio of the bellow for each condition of the experimental characterisation at a frequency, f, of 2.5, 3.5 and 5 Hz.

Table 6-29: Fluid energy transfer ratio @ 2.5 Hz

P_A [kPa]	P_D [kPa]	η [%]
0	20	16.59
0	35	16.87
0	50	22.43
-20	0	23.63
-30	0	32.16

Table 6-30 illustrates the fluid energy transfer ratio of the bellow for each condition of the experimental characterisation at a frequency, f, of 3.5 Hz.

Table 6-30: Fluid energy transfer ratio @ 3.5 Hz

P_A [kPa]	P_D [kPa]	η [%]
0	0	13.68
0	20	26.25
0	50	38.88
-30	0	66.05

Table 6-31 illustrates the fluid energy transfer ratio of the bellow for each condition of the experimental characterisation at a frequency, f, of 5 Hz.

Table 6-31: Fluid energy transfer ratio @ 5 Hz

P_A [kPa]	P_D [kPa]	η [%]
0	0	20.16
0	20	43.95

6.4 Conclusions

The phase angle was successfully experimentally calibrated for each condition. The dynamic properties of the bellow were successfully experimentally characterised for each condition. The vibration energy and power of the bellow were successfully experimentally determined for each operating condition along with the power required at transient behaviour at one operating condition. The flow properties were also experimentally characterised for each operating condition. The fluid energy transfer ratio of the bellow was also successfully experimentally determined for each operating condition.

In Chapter 7 the numerical integration model is validated, and the experimental results are evaluated in more detail.

7 Validation of Numerical Model and Experimental Evaluation

7.1 Introduction

In this Chapter, the measured transient response is compared to the predicted values calculated to validate the numerical integration model. The bellow was evaluated in terms of dampening properties, vibrational mechanical energy and power transferred to the bellow and the fluid power transferred from the bellow. These properties were evaluated against the amplitude, frequency and pressure dependence of the operating condition. Note that all the results are given during the evaluation, where anomalies and grouping of results were explained where necessary.

7.2 Transient Validation

The transient responses were measured for a condition during start-up of the bellow system as described in Section 6.2.2.2. As seen in Figure 6-3 and Figure 6-4 the predicted acceleration and the experimentally obtained signals were plotted. Table 7-1illustrates the predicted and actual acceleration amplitude of the transient condition of the bellow system at 20% unbalance.

Table 7-1: Predicted and measurable responses for transient condition

n		20%						
P_A [kPa]	P_D [kPa]	ϕ [Deg]	X [mm]	k_p [N/mm]	ζ [-]	$\ddot{x}_{actual}$ [m/s^2]	$\ddot{x}_{predict}$ [m/s^2]	Deviation [%]
0	0	-6.53	0.66	131.81	0.17	18.36	20.07	9.3

There is a difference between the actual acceleration and predicted acceleration of 9,3%. The small difference could be due to the change in dynamic properties such as stiffness and damping with a change in amplitude during start-up.

7.3 Dynamic Properties Evaluation

The dynamic properties of the rubber bellow system were evaluated in terms of the change in amplitude, frequency and pressure respectively, with the findings discussed accordingly.

7.3.1 Amplitude Dependency

Figure 7-1 shows the amplitude dependency of all the test results of the stiffness coefficient for the bellow system, with most results were in the range of 80-200 N/mm, where 220 N/mm is indicated in orange and 80 N/mm in grey. It was noted that the stiffness evaluated for the bellow system at a frequency of 25 Hz and 100% unbalance mass, were much larger than the other results, grouped at roughly 780 N/mm. This group of results could be due to the increase of frequency at 100% unbalance mass operating conditions. From the results below it is clear that the stiffness of the bellow isn't constant with a change in amplitude, although the values don't seem to have a correlation with the change in amplitude.

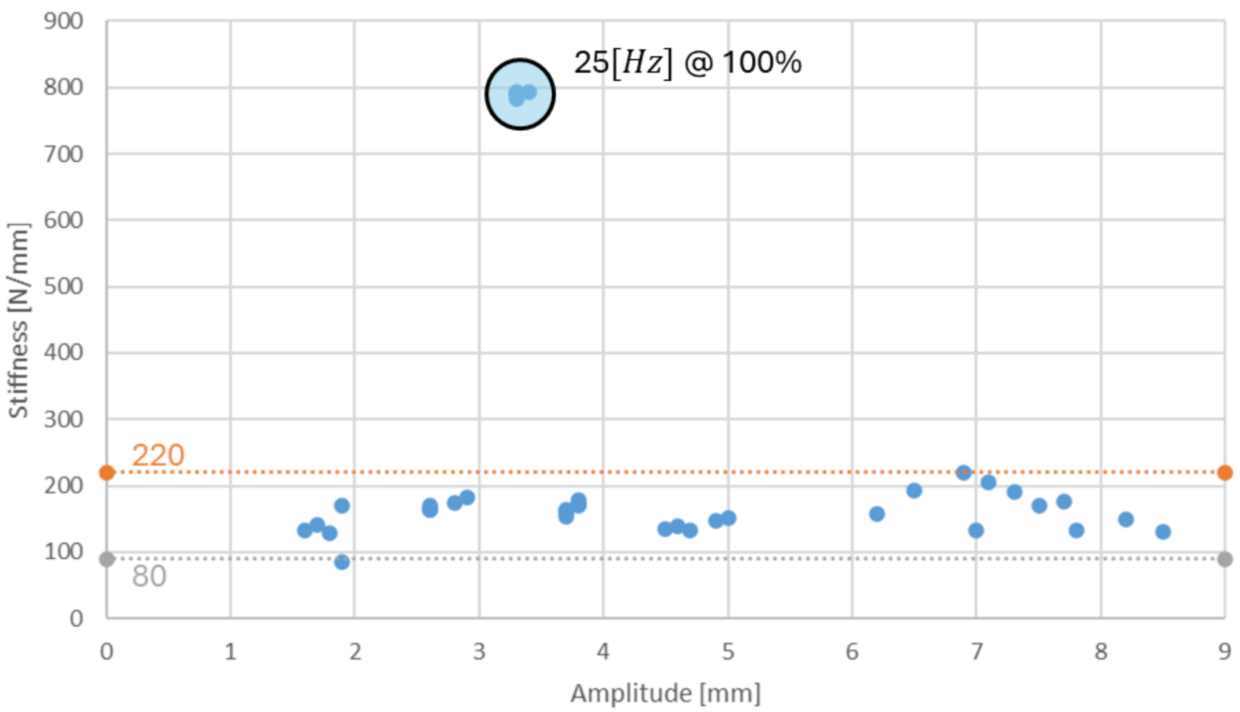

Figure 7-1: Stiffness coefficient vs. amplitude (experimental), results at 100% unbalance and 25 Hz highlighted

Figure 7-2 shows the amplitude dependency of the damping ratio for the bellow system. From the plot below it is visible that at lower amplitudes (<5 mm) the damping ratio is less than 30%, where the damping ratio varies more and could be as great as 84% at higher amplitudes (6-9 mm). This could be due to the frictional damping caused by the increase in material deformation of the rubber bellow.

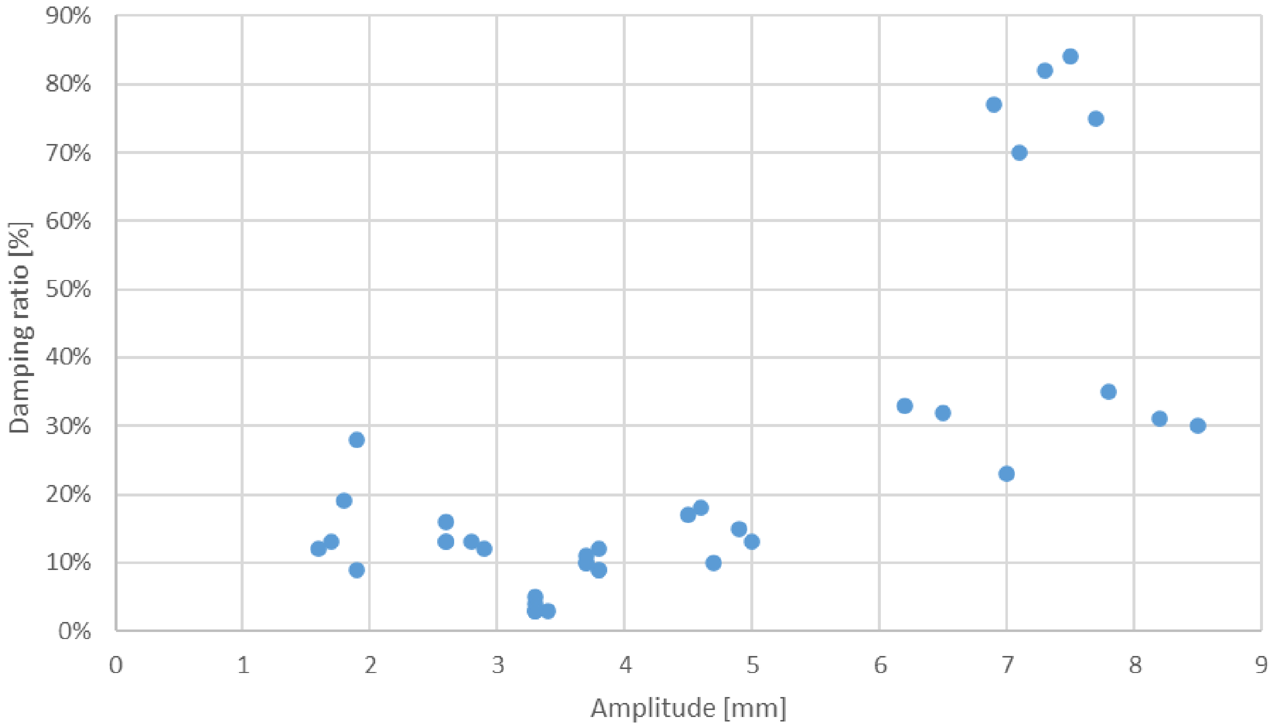

Figure 7-2: Damping ratio vs. amplitude (experimental)

7.3.2 Frequency Dependency

In Chapter 3 the bellow system's dynamic properties were experimentally characterised. Although most results varied from 80 to 200 N/mm, it was noted that the stiffness evaluated for the bellow system at a frequency of 25 Hz and 100% unbalance mass, were much larger than the other results, grouped at ≈790 N/mm. A further study at higher frequencies could supply some clarity on the effect of higher frequencies at higher excitation forces.

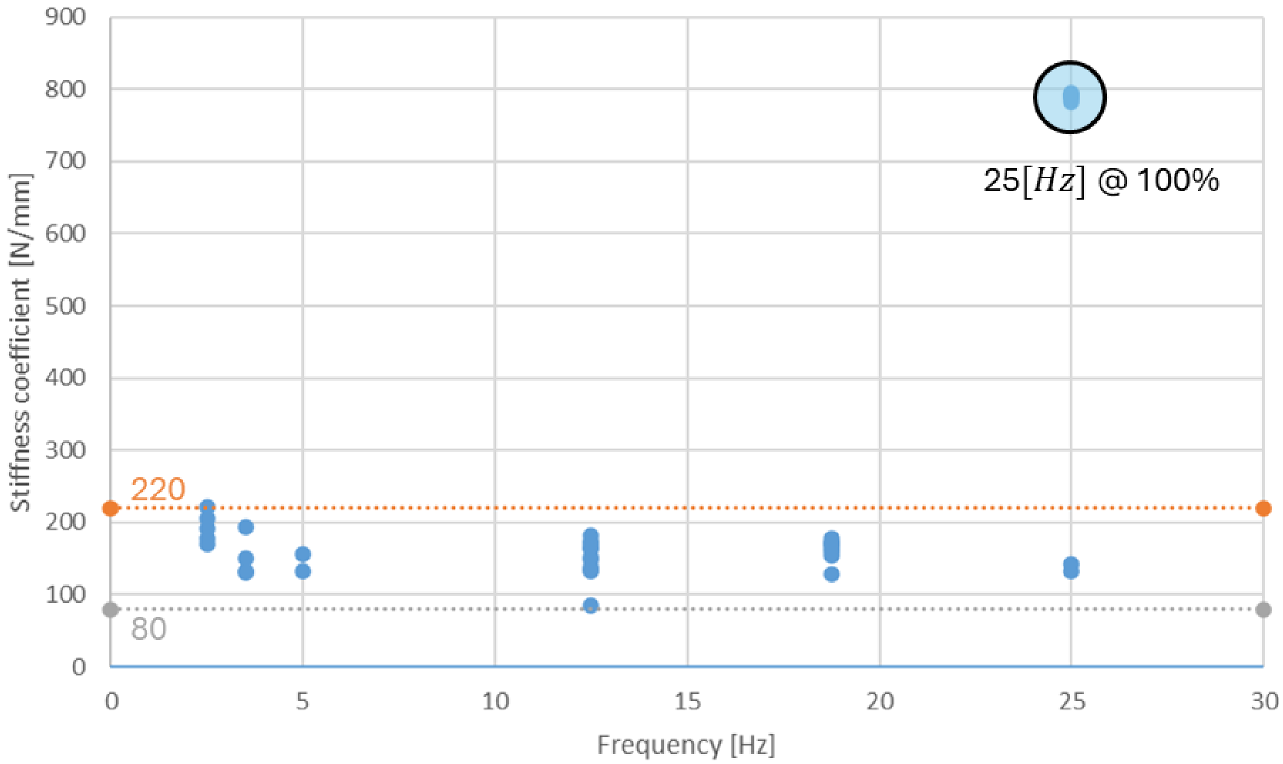

Figure 7-3: Stiffness coefficient vs. frequency (experimental)

Figure 7-4 shows the damping ratio vs the frequency of the rubber bellow system. From the figure below it is clear that there is a decrease in damping ratio with an increase in frequency.

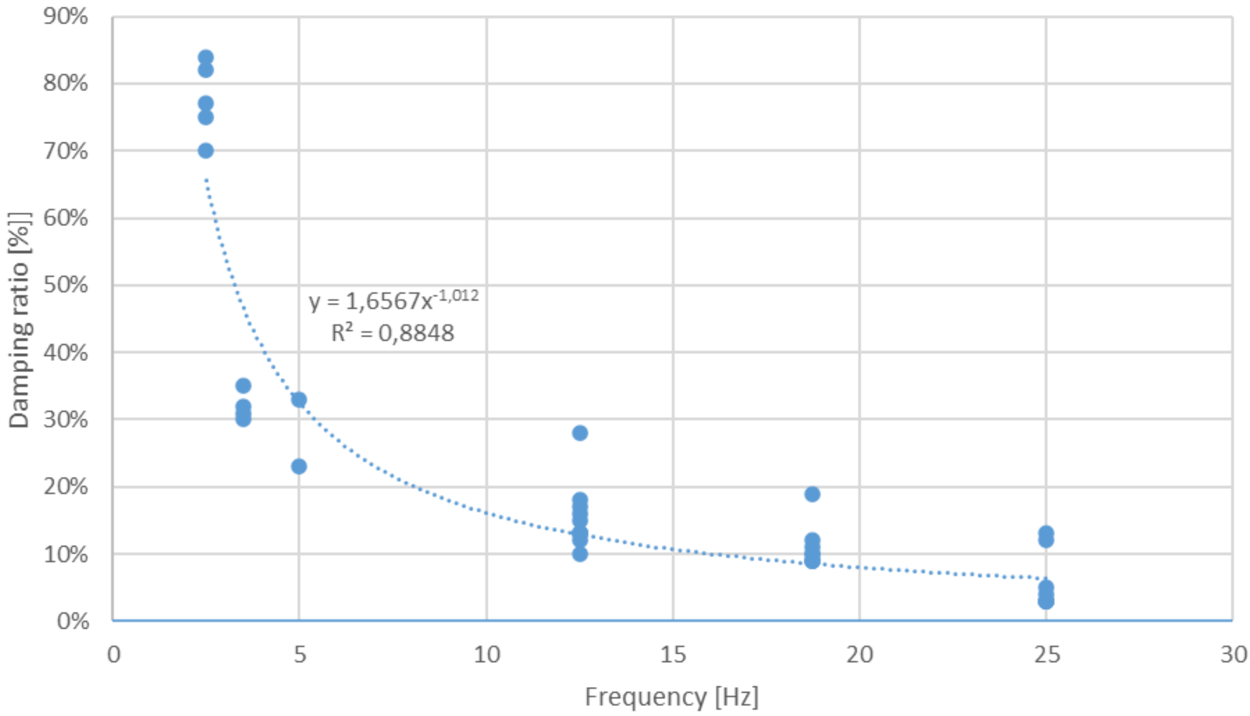

Figure 7-4: Damping ratio vs. frequency (experimental)

7.3.3 Pressure Dependency

Figure 7-5 shows the stiffness coefficient vs the pressure difference over the bellow system. Although the most results varied from 80 to 200 N/mm, it was noted that the stiffness evaluated for the bellow system at a frequency of 25 Hz and 100% unbalance mass, were much larger than the other results, with an average of 790 N/mm. Excluding the results that were around 790 N/mm, it seems that there is an inclining trend with the increase of pressure. By characterizing the bellow system at higher pressures will enable sufficient evaluation of this possible trend.

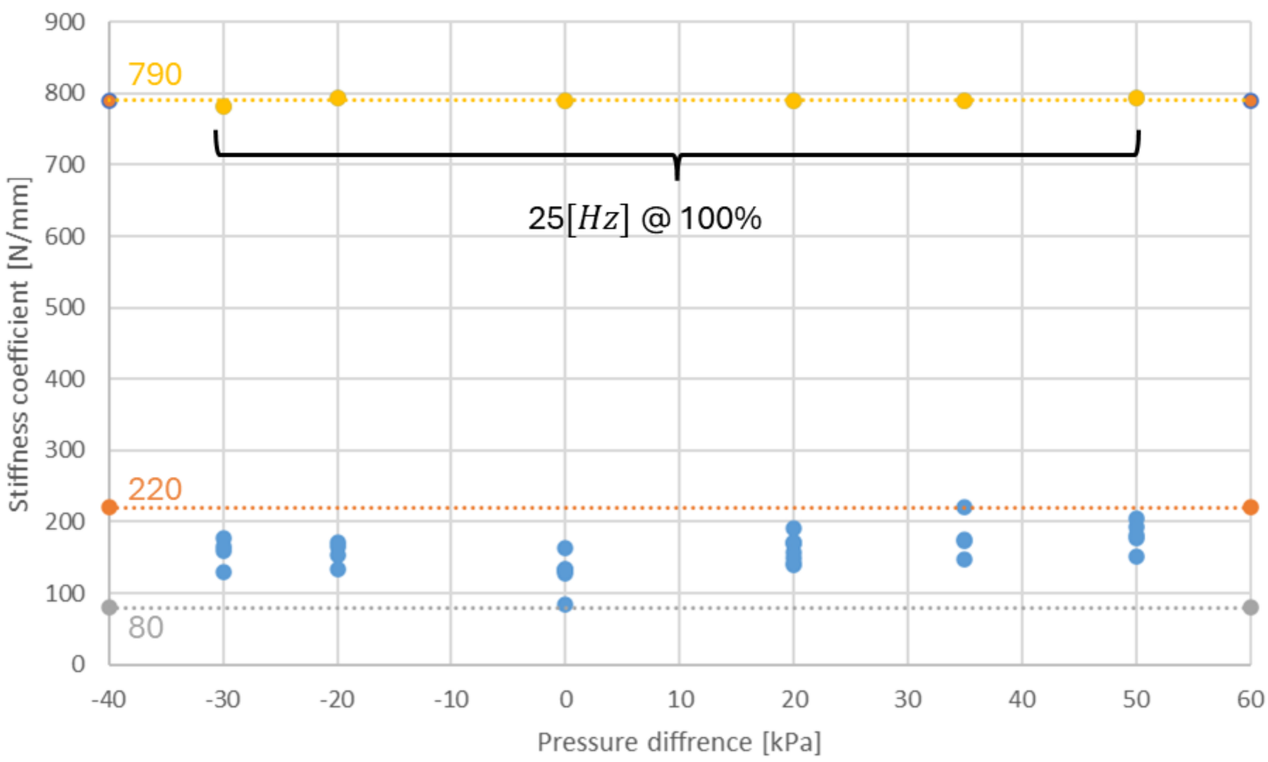

Figure 7-5: Stiffness coefficient vs pressure (experimental)

Figure 7-6 shows the pressure dependency for the damping ratio of the bellow system. Due to the strong correlation between the operating frequency and damping ratio, as discussed in Section 7.3.2, the results were grouped in different operating frequencies to better isolate the change in damping ratio due to a change in pressure. From the figure below there is a slight increase in damping ratio when there is no differential pressure in the system.

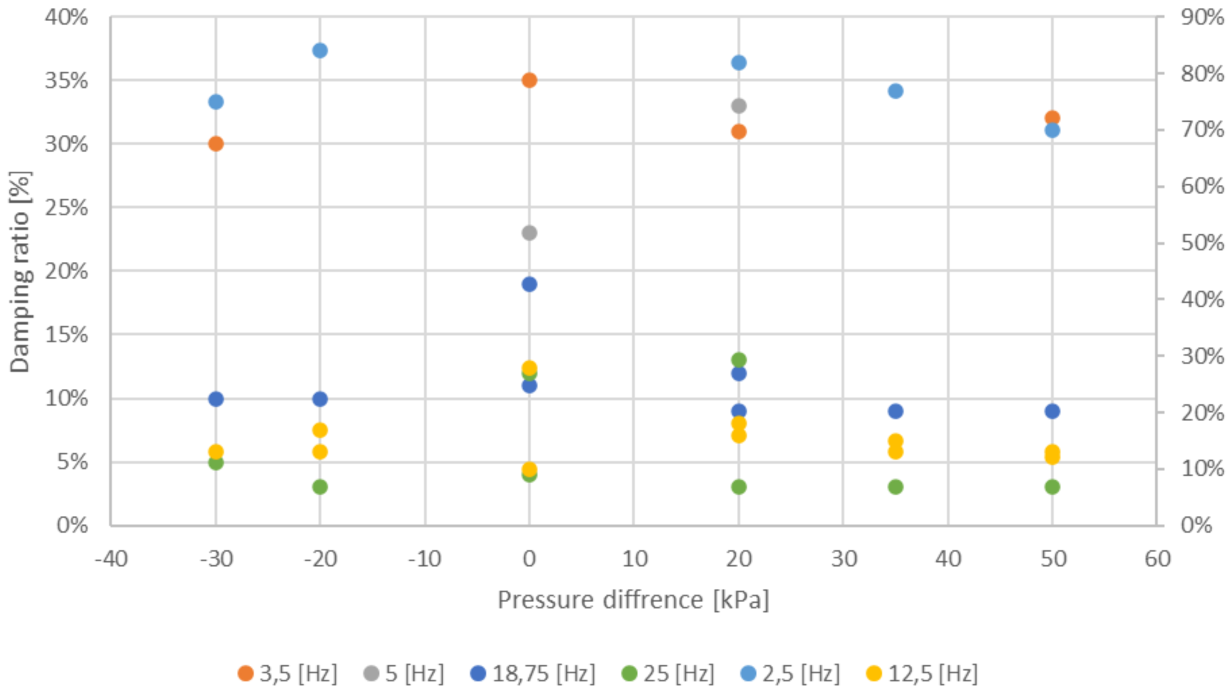

Figure 7-6: Damping ratio vs. pressure (experimental)

To better understand the pressure dependence of the damping ratio, the damping ratio of the rubber bellow system was plotted at a change in absolute pressure difference, as seen in Figure 7-7. Although there is no clear correlation between the damping ratio and the absolute pressure difference of the system, it is seen from the figure below that the damping ratio of the system decreases with an increase in pressure difference. If the pressure range was increased in a future study, this decrease in damping ratio could be confirmed.

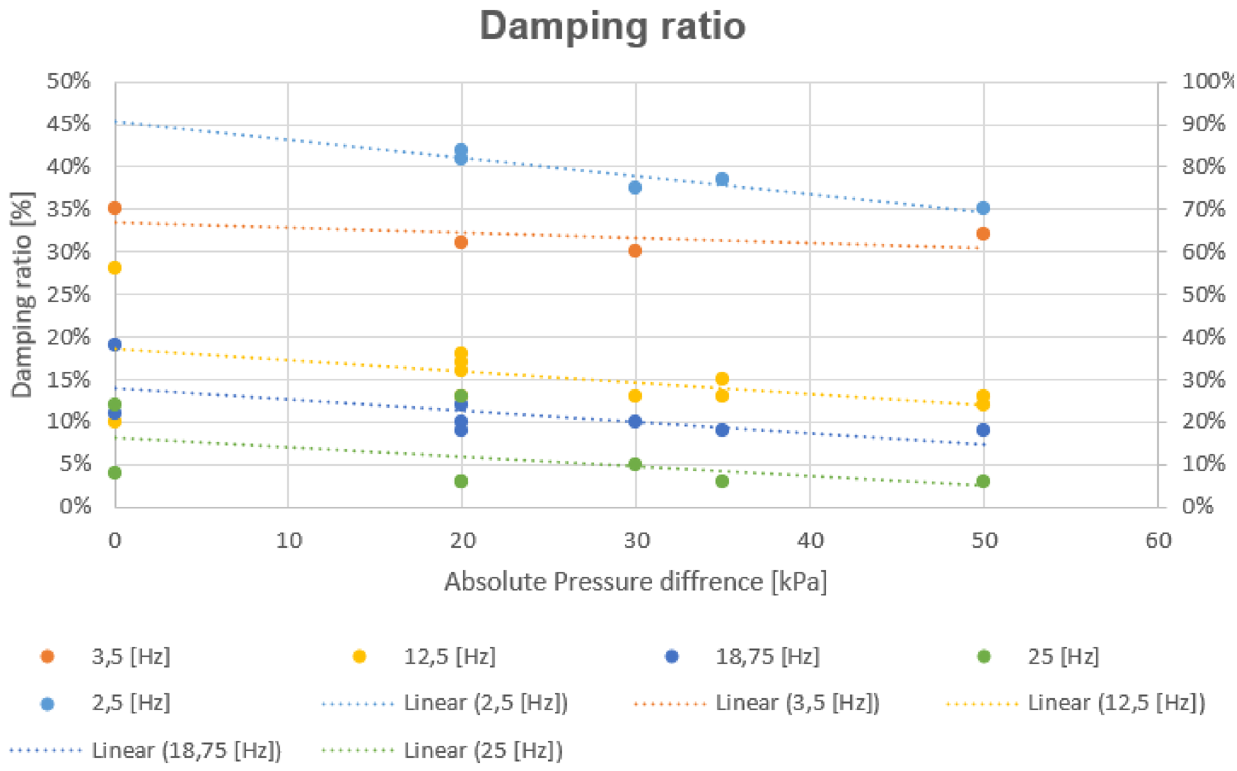

Figure 7-7: Damping ratio vs. absolute pressure (experimental)

7.4 Vibration Power Evaluation

In this Section the vibrational energy transfer was evaluated in terms of a change in amplitude, frequency and pressure. From Section 4.3, it is clear that the average power that is transferred to the bellow is due to the damping power element of the system. The only dependency and relation, as seen in Equation (4-22) can be expressed as:

$$\mathbb{P}_v = \frac{1}{2} c_m \omega^2 X^2$$

7.4.1 Amplitude Dependency

From the equation of the vibration power, the vibration power is proportional to the square of the amplitude, if the damping in the system stays constant. From Section 7.3 it is clear that the damping in the system is not constant when there is a change in amplitude. Figure 7-8 shows the vibration power of the system with a change of amplitude. To illustrate the change in vibration power with a change in amplitude, the results were grouped in four categories, lower frequencies (2.5, 3.5 and 5 Hz), 12.5, 18.75, and 25 Hz respectively. From the figure below it is clear that the vibration energy of the system increased with an increase in amplitude at the same frequency. It is also clear that that the rate of increase is less at lower frequencies. The trendline for 12.5, 18.75 and 25 Hz had a high correlation rate of 0.74, 0.93 and 0.84 respectively. The highlighted section of the figure illustrates the lower frequency results that showed minimal correlation between the amplitude and the vibration power since the amplitude range is relatively small. To obtain better characterisation for the amplitude dependencies at lower frequencies, the bellow system should be characterised at a wider range of amplitudes at lower frequencies.

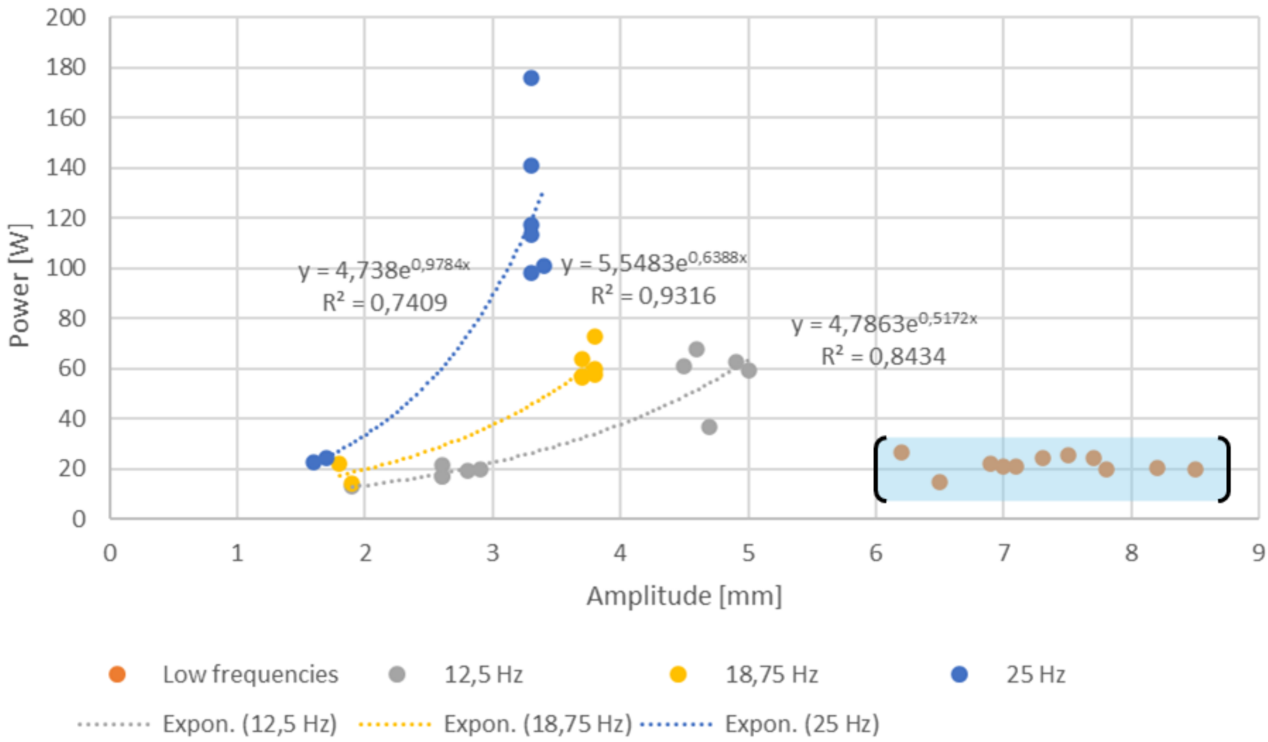

Figure 7-8: Vibration power vs. amplitude (experimental)

7.4.2 Frequency Dependency

From the equation of the vibration power, the vibration power is proportional to the square of the frequency, if the damping in the system stays constant. From Section 7.3 is clear that the damping in the system is not constant when there is a change in frequency. Figure 7-9 shows the vibration power of the system with a change in frequency. To illustrate the change in vibration power with a change in frequency, the results were grouped in three categories, lower frequency ranges, at 50% unbalance and 100% unbalance respectively. From the figure below there is not a significant change in the vibration power with a change of frequency for the lower frequency range or the 50% unbalance results. The 100% unbalance results indicate an increase in vibration power with an increase in frequency.

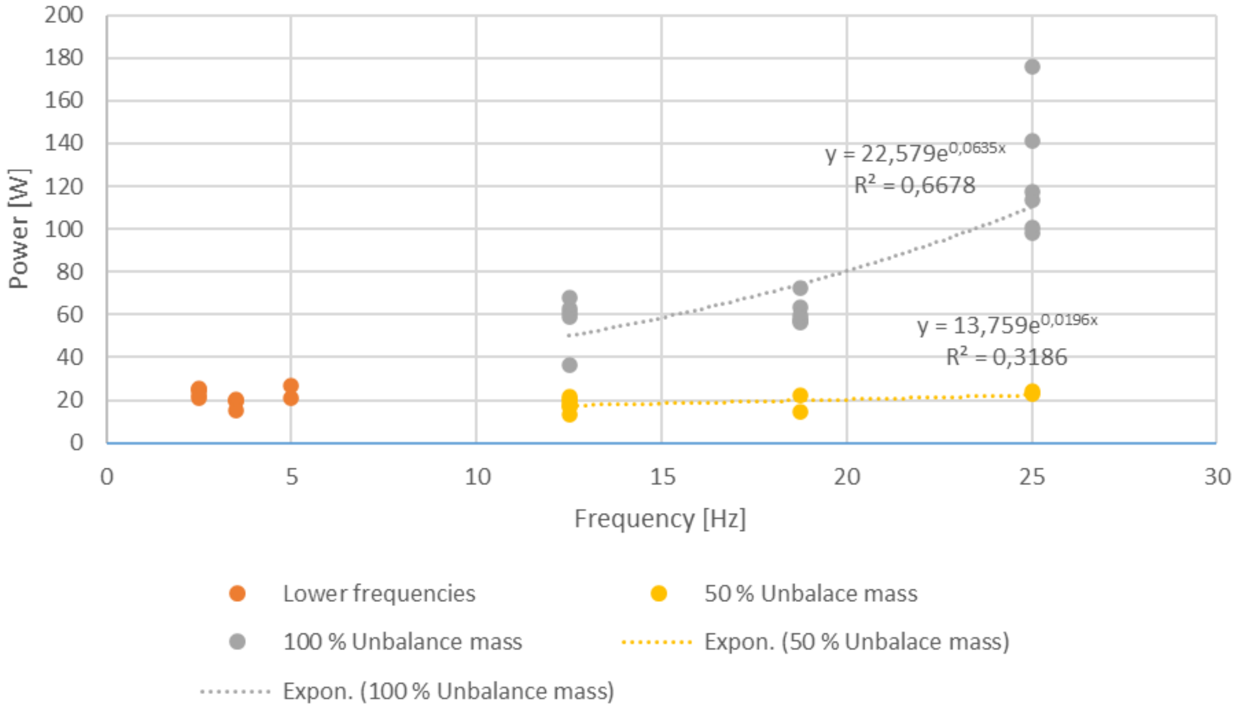

Figure 7-9: Vibration power vs. frequency (experimental)

7.4.3 Pressure Dependency

Figure 7-10 shows the vibration power of the system with a change in pressure for each characterisation condition. From the figure below there it wasn't a clear correlation between the vibration power and the change of pressure, although it is noted that there seems to be a slight decrease in power at higher pressure differences.

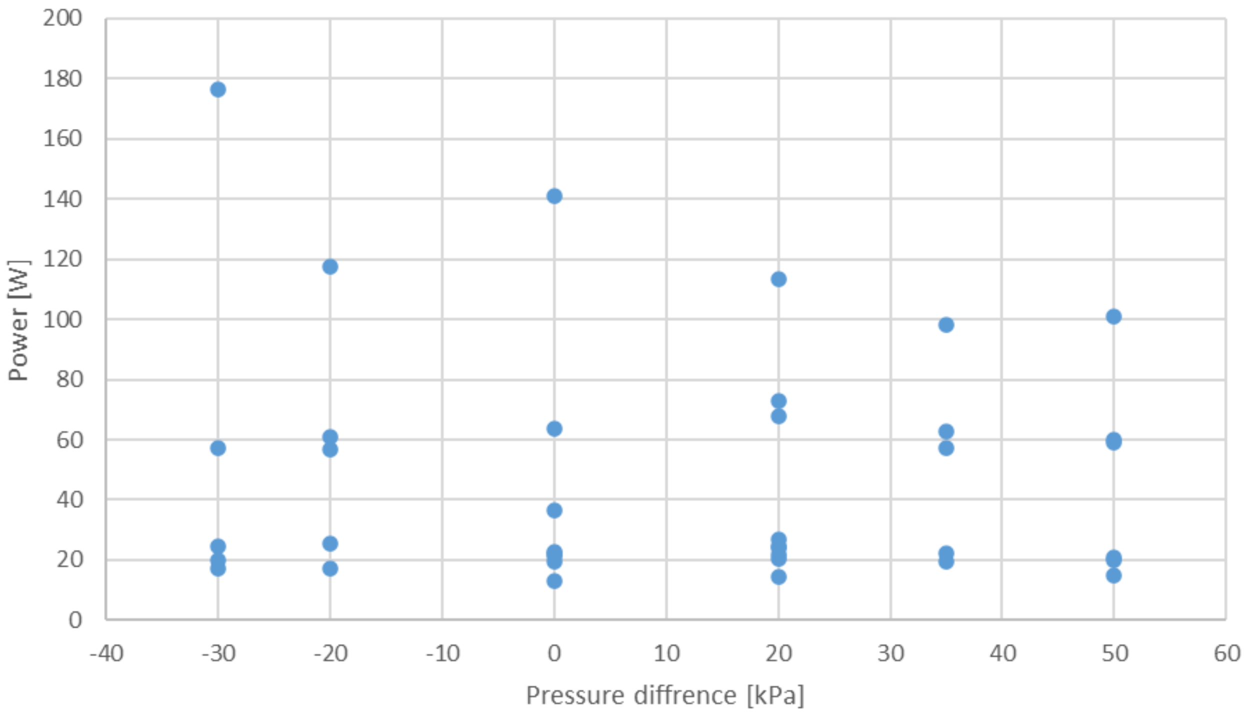

Figure 7-10: Vibration power vs. pressure (experimental)

7.5 Flow Energy Evaluation

In this Section the flow energy is evaluated in terms of a change in amplitude, frequency and pressure. This flow energy gives an indication of the portion of energy transferred to the fluid in the system from the vibration energy of the system (with the remainder of the vibrational energy that is absorbed by the inherent mechanical damping of the components).

7.5.1 Amplitude Dependency

Since the hydraulic power is directly proportional to the vibration energy, a similar amplitude dependency was expected for the hydraulic power as seen in Section 7.4.1. Figure 7-11 shows the hydraulic power of the system vs a change of amplitude. The results were divided in two groups for more clarity, one for higher frequencies, including the characterisation at 12.5, 18.75 and 25 Hz, and at lower frequencies, including 2.5, 3.5 and 5 Hz, to better evaluate the amplitude dependency of the hydraulic power. From the figure below it is clear that the hydraulic power of the system increased with an increase in amplitude at higher frequencies, however the correlation at lower frequencies were not clear to determine. This might be attributed to secondary flow effects inside the bellow caused by increased wall movement and possible energy loss through fluid heating.

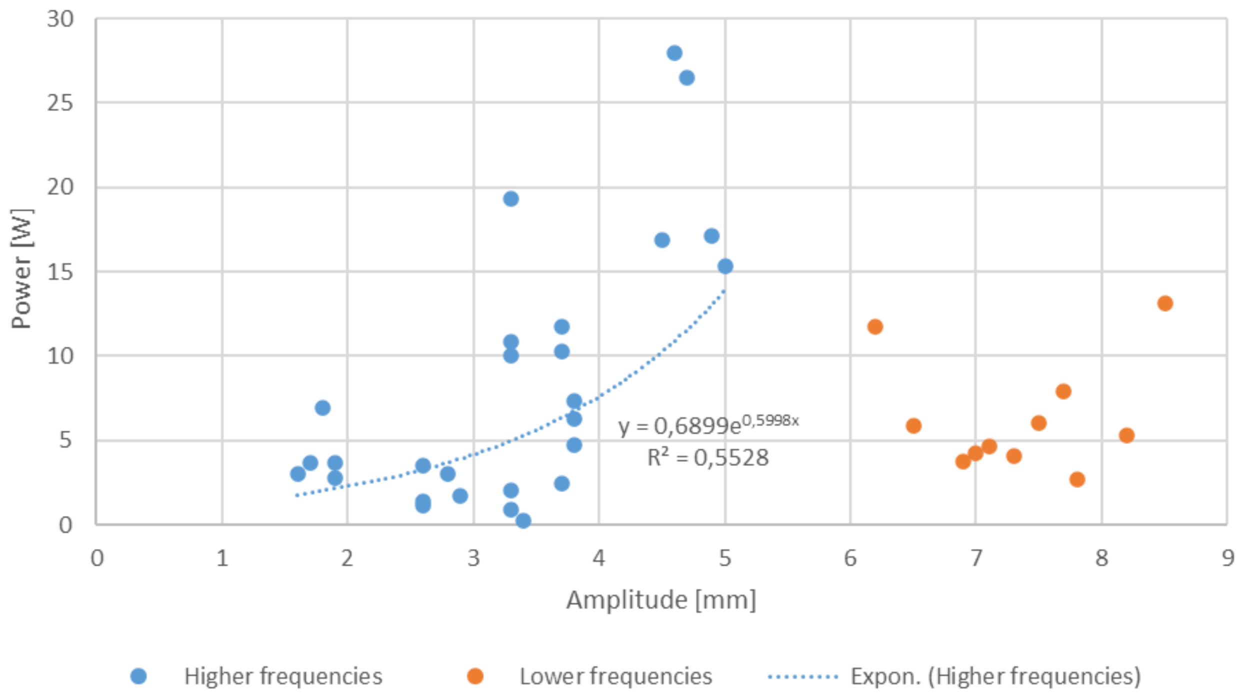

Figure 7-11: Hydraulic power vs. amplitude (experimental)

Figure 7-12 shows the fluid energy transfer ratio of the system vs the change in amplitude. Although it seems that there is an increase in fluid energy transfer ratio with the increase in amplitude, the correlation of this dependency is unclear and could be better defined at higher amplitudes to determine if there is an external effect on the dependency.

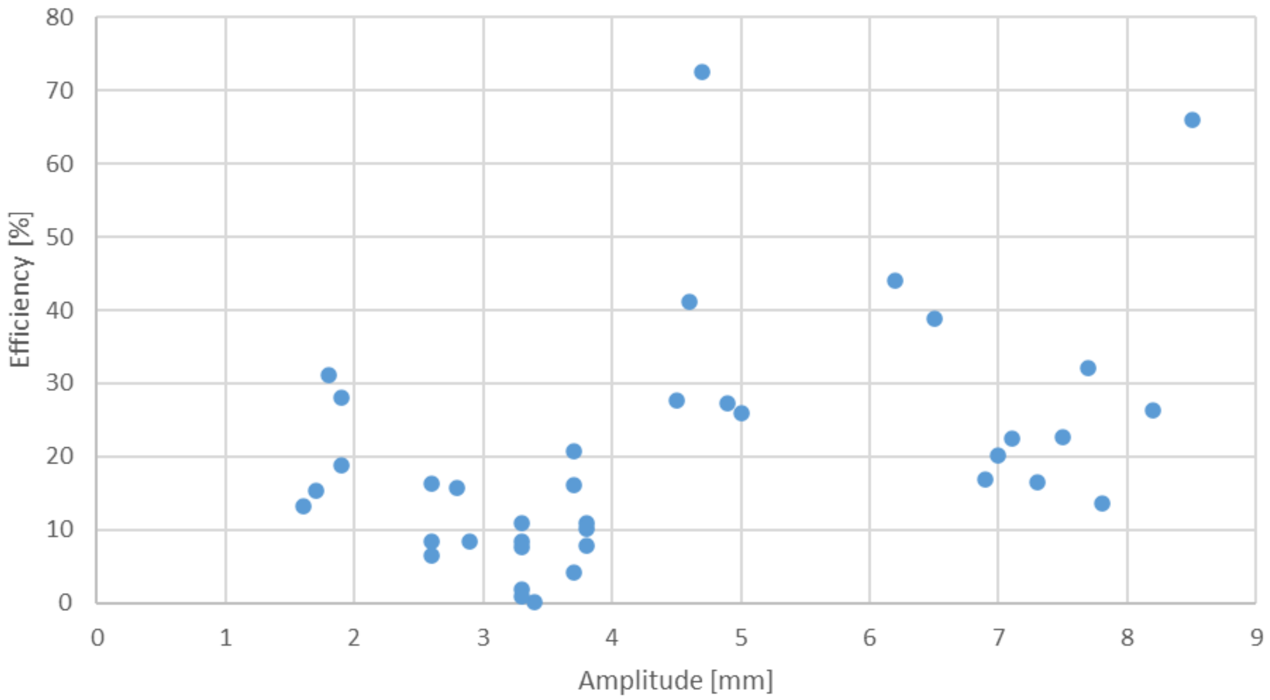

Figure 7-12: Fluid energy transfer ratio vs. amplitude (experimental)

7.5.2 Frequency Dependency

Figure 7-13 shows the hydraulic power of the system vs a change of frequency. From the figure below there is no clear correlation between the hydraulic power of the system and the amplitude since the correlation coefficient is very low, even when the results are considered respectively for different frequency ranges and unbalance masses.

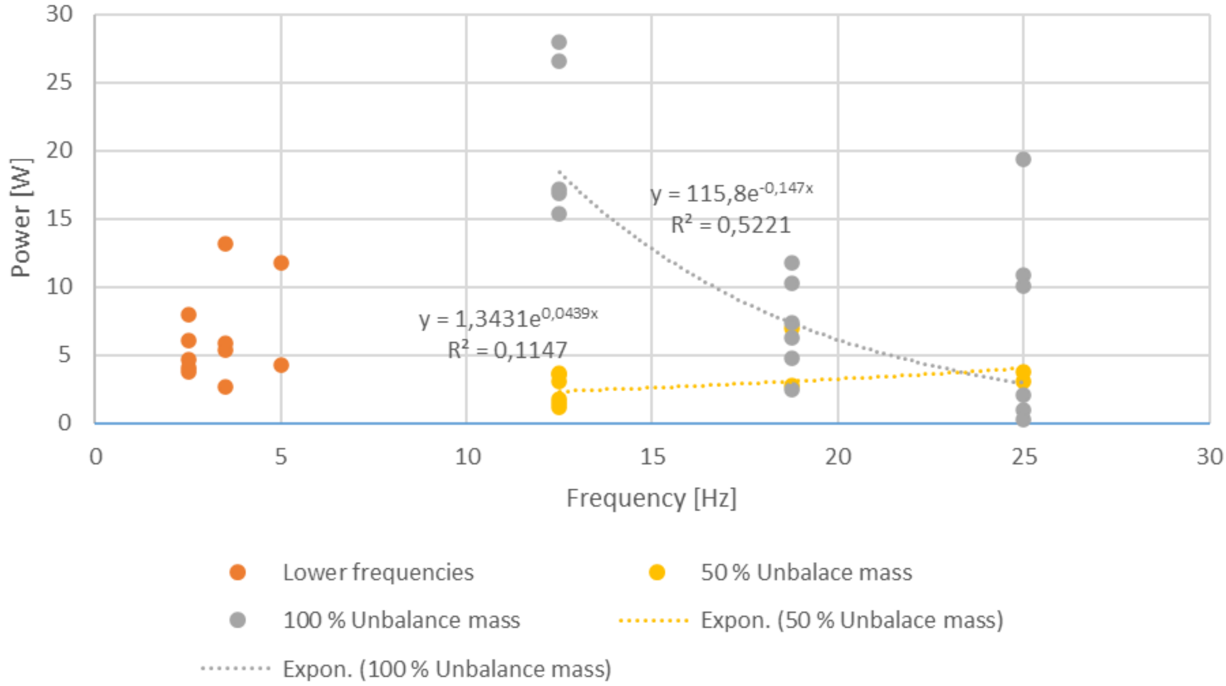

Figure 7-13: Hydraulic power vs frequency (experimental)

Figure 7-14 shows the fluid energy transfer ratio of the system vs the change in frequency. From the figure it is seen that the fluid energy transfer ratio of the system reduces at higher frequencies. This indicates that at higher frequencies, less of the vibration power will be transferred to the fluid. Although the correlation between the increase in frequency and the fluid energy transfer ratio is not great, it is seen in the figure below that the range of fluid energy transfer ratio reduces with an increase in frequency (As indicated by the green trendlines).

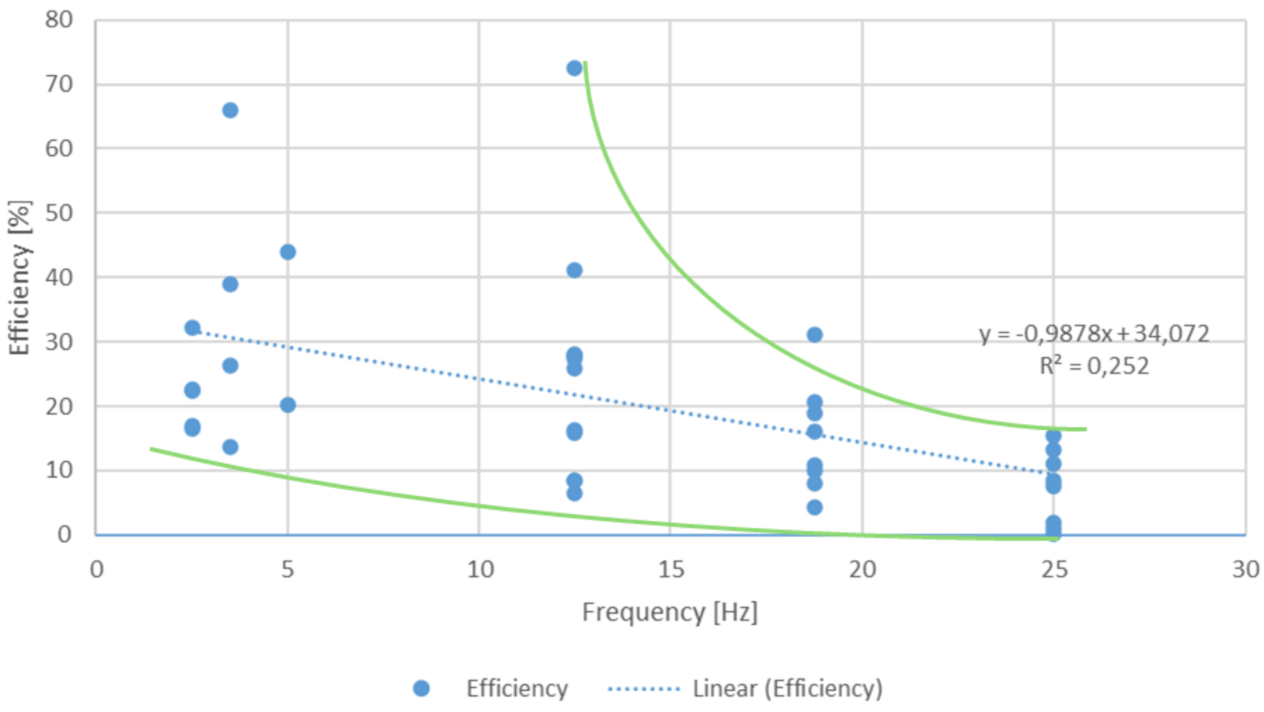

Figure 7-14: Fluid energy transfer ratio vs. frequency (experimental)

7.5.3 Pressure Dependency

Figure 7-15 shows the hydraulic power of the system vs a change of pressure. From the figure below there is a weak correlation between the hydraulic power of the system and the amplitude, although it seems that the hydraulic power of the system decreases with the increase in absolute pressure difference at higher frequencies and increases at lower frequencies.

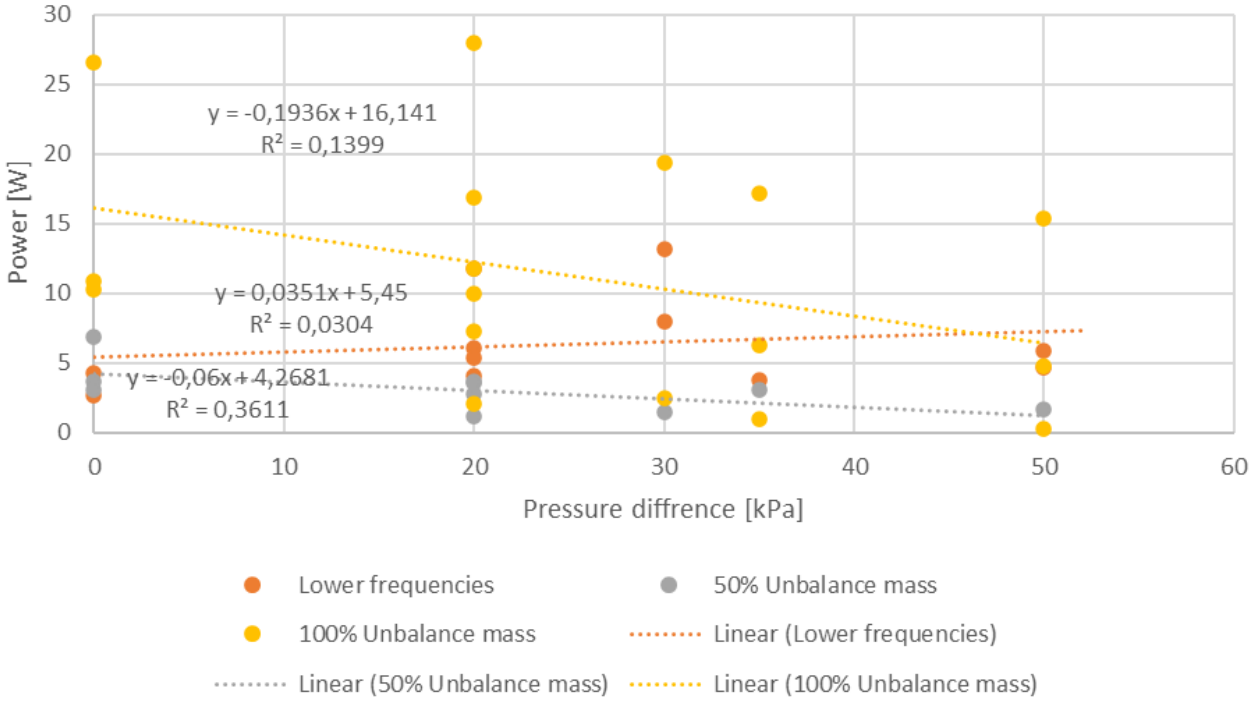

Figure 7-15: Hydraulic power vs. absolute pressure difference (experimental)

Figure 7-16 shows the fluid energy transfer ratio of the system vs the change in pressure. From the figure there is no clear correlation between the fluid energy transfer ratio of the system with a change in pressure delivered, although it is seen that the fluid energy transfer ratio at lower frequencies increases with an increase in pressure of the system.

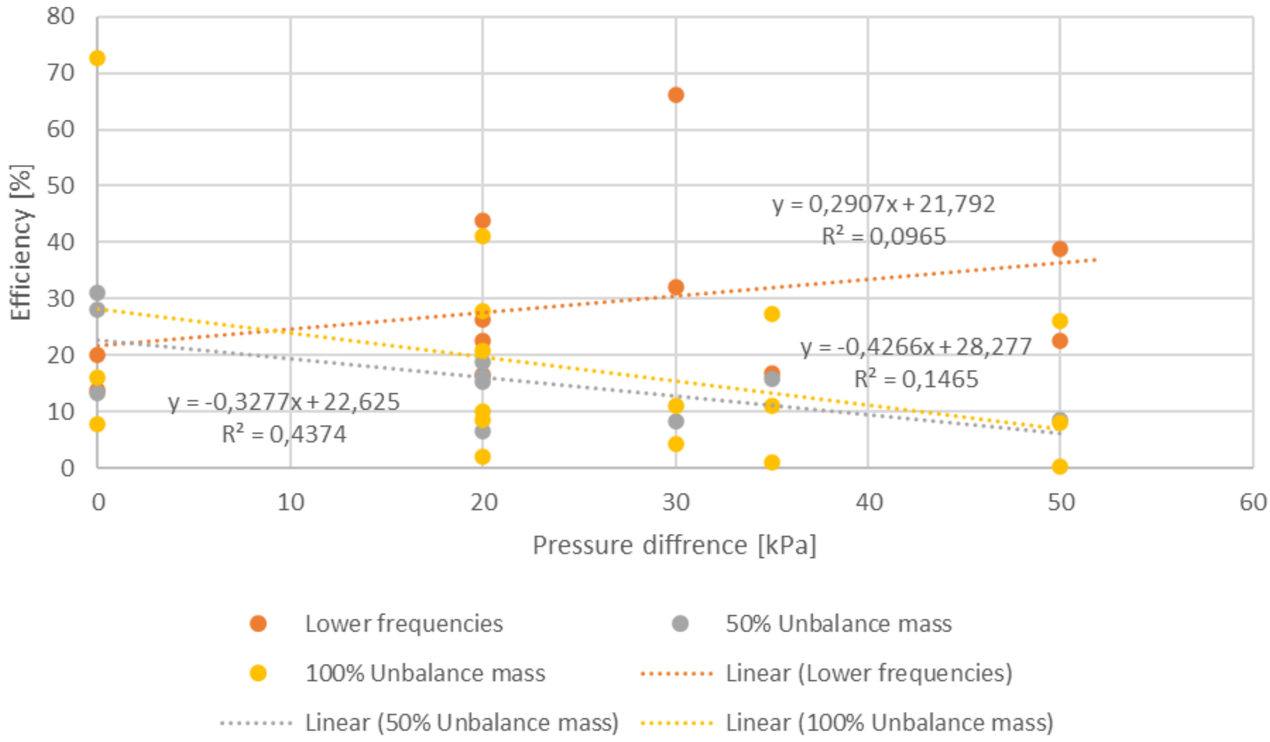

Figure 7-16: Fluid energy transfer ratio vs. pressure (experimental)

7.6 Summary of Results

In Section 7.2 it was seen that the predicted excitation of the bellow during transient behaviour correlated well with the actual excitation, with a correlation of 9.3%. The small difference could be related to the amplitude dependency on the dynamic properties of the rubber bellow (Chai et al., 2014). Therefor the transient modelling of the system can be accepted as accurate for the evaluation of the results.

In Section 7.3 the dynamic properties of the bellow were evaluated in terms of the amplitude dependency of the system. Although the stiffness of the system measured between 150 and 200 N/mm, the damping coefficient of the system increased substantially as seen in Figure 7-2. This is helpful if this bellow's application has a certain amplitude, then the expected damping could be brought into consideration with initial design specifications. If the expected amplitude is less than 5 mm, you can expect a maximum damping ratio of 30%, where if you have an expected amplitude of 6 to 9 mm, the damping ratio of the bellow system could be as high as 80%. Figure 7-17 shows the illustration of the two scenarios discussed.

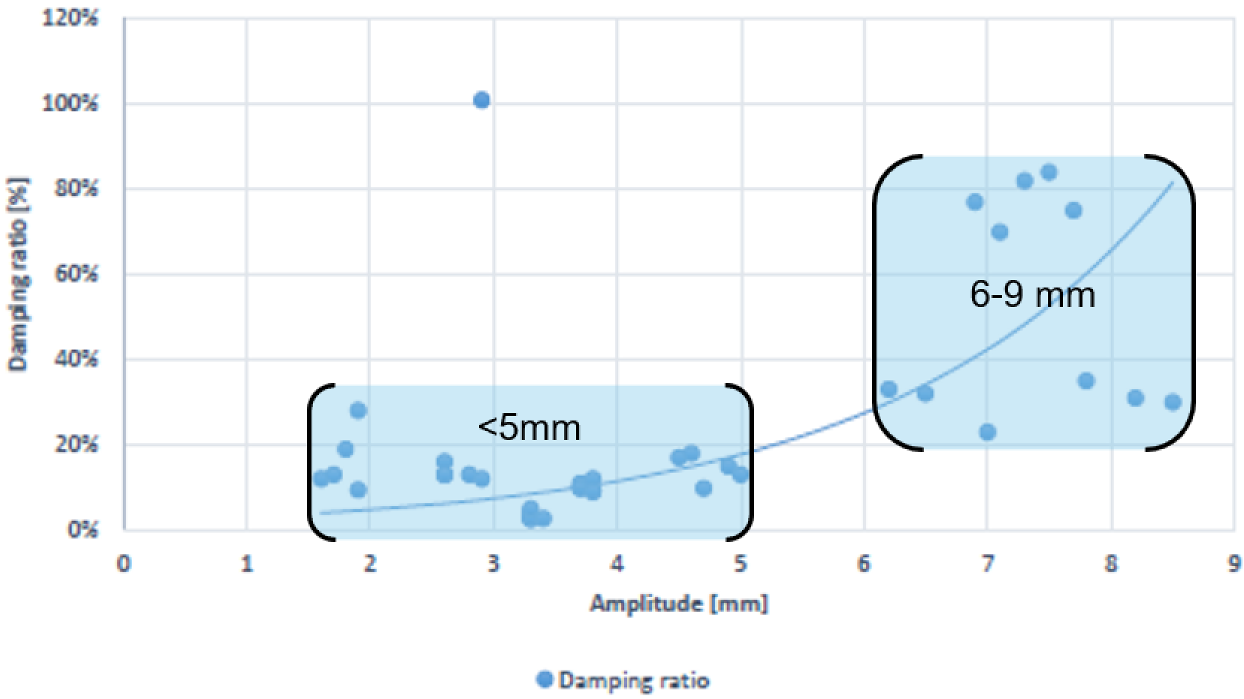

Figure 7-17: Damping ratio vs. amplitude summary

In Section 7.3.2 the dynamic properties of the bellow were evaluated in terms of the frequency dependency of the system. Although there is no clear relation seen between the stiffness and the frequency of the system, the damping coefficient of the system decreased with the increase of frequency. This is helpful if the operating frequency of the system is known, the damping ratio of the system could be anticipated which will help in the design of the system. The trendline used in Figure 7-4 has a strong coefficient of correlation (0.88), which could be used to determine the damping coefficient at different frequencies. Figure 7-18 shows the trendline details and an example of using the trendline equation to determine the damping ratio of the system when the operating frequency is 10 Hz.

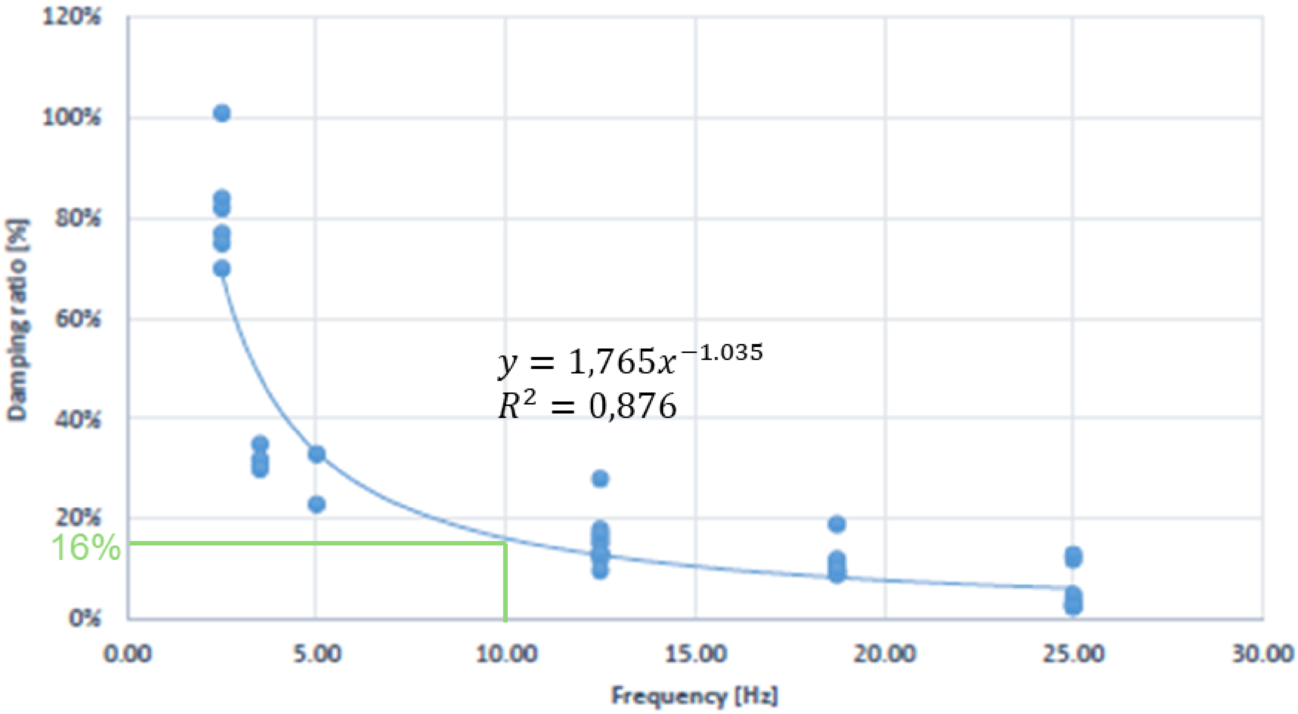

Figure 7-18: Damping ratio vs. frequency with trendline details

In Section 7.3.3 the dynamic properties of the bellow were evaluated in terms of the pressure dependency of the system. No explicit correlation between the operating pressure and the dynamic properties of the bellow was found, implying that the bellow damping properties can be used without adjusting for pressure conditions.

In Section 7.4 the vibration power of the bellow system was evaluated in terms of dependency towards amplitude, frequency and pressure. The only clear indication is that the vibration energy increase with an increase in amplitude, and that the rate of increase is dependent on the operating frequency. As discussed in Section 7.4.1 and seen in Figure 7-8.

In Section 7.5 the flow energy of the bellow system was evaluated in terms of dependency towards amplitude, frequency and pressure. From Figure 7-11 it is seen that the energy transferred to the fluid increases with an increase in amplitude, although the fluid energy transfer ratio or percentage of vibration energy that is transferred to the fluid doesn’t have a clear correlation, as seen in Figure 7-12. From Figure 7-14 it is seen that the fluid energy transfer ratio of the energy transferred to the fluid decreases with an increase in frequency. This indicates that the proportion of vibration energy that is transferred to other equipment and structures will be more at higher frequencies.

In Section 7.5 the fluid energy transfer ratio of the system reaches a maximum of 72%, this is important if the desired application of this bellow system is to transfer energy to the fluid in the system. Possible solutions would be to implement a dual function system, responsible for reducing the transferred vibrations to nearby structures and to circulate fluid as an auxiliary system.

The numerical integration model, implemented in MATLAB, was successfully validated, and the experimental results were successfully evaluated.

In Chapter 8 the conclusion and recommendations from this study are discussed.

8 Conclusions and Recommendations

8.1 Conclusions

Mathematical models were successfully developed and implemented in a MATLAB environment to characterise and investigate the change in dynamic properties of a rubber bellow system under different operating conditions and to provide an indication of the expected transient behaviour in such a system. A single degree-of-freedom mathematical model was developed and used to predict the dynamic properties at steady-state conditions and vibrational behaviour at transient conditions.

The input parameters required for the mathematical model were described and included the mass of the system, the length of the pipes used for in the inlet and discharge sections of the system, the applicable elevation heights, the water lever of the inlet tank, the respective pressure gauges and the height of the one-way valves, and the diameters of the piping.

An experimental setup was designed and manufactured, where a closed-loop hydraulic system was used with an in-line rubber bellow that was excited vertically by means of unbalanced vibration motors. A second setup was used to excite the system at lower frequencies; in this setup a gear-reduction motor was used. An accelerometer, eddy current probe and load cell were used as vibration instruments to characterise the acceleration response, phase angle and excitation force, respectively. To characterise the dynamic properties of the system, the phase angle of the system was calibrated under neglectable mechanical damping conditions and used as a reference for future characterisation. The dynamic properties were experimentally determined, where the stiffness and damping coefficient of the system were characterised at different frequencies, excitation forces, and pressures. The vibration and fluid energy were characterised at these frequencies, excitation forces, and pressures. The fluid energy transfer ratio of the power transferred to the fluid from the vibration energy was also measured, in order to determine the split between vibrational energy absorbed by the bellow material, and that absorbed by the fluid.

The numerical integration model was firstly validated by comparing the predicted transient behaviour with the transient response obtained experimentally. The dynamic properties were evaluated in terms of the change in amplitude, frequency and pressure in the system respectively, where the most significant changes were discussed and analysed. The vibration energy was evaluated in terms of the change in amplitude, frequency and pressure in the system respectively, where the most significant results were discussed.

When evaluating the dynamic properties of the rubber bellow system, there was a clear indication that the damping ratio of the system increased with an increase in amplitude. In applications where the amplitude of the system is known, the damping ratio could be predicted and introduced into the design calculations. Should the amplitude be less than 5 mm, the expected damping ratio can be expected to be less than 30%, where the damping ratio could be up to 80% at amplitudes higher than 6 mm. The damping ratio's dependency with regards to a change in frequency was declining with an increase in frequency, where the evaluated results had a correlating trendline. By using the equation of power, the expected damping ratio could be determined at the operating frequency. Table 8-1 illustrates the damping ratio guideline gathered from the evaluation, which will aid in the correct application design.

Table 8-1: Damping ratio expectation guideline

Known design criteria	Damping-ratio expectation	Notes
Amplitude <5 [mm]	0-30%	See frequency dependence
Amplitude 6-9 [mm]	30-80%	See frequency dependence
Operating frequency	$y = 1.765x^{-1.035}$	y (Damping ratio) x (Frequency [Hz])

The fluid energy and power were evaluated in terms of the change in amplitude, frequency, and pressure, respectively, with the goal of determining how much energy is transferred to the fluid from the system. These evaluations and results were summarised. By simulating the vibration energy and the amount of energy transferred to the fluid in the system, efficiencies of more than 70% were observed. However, no correlation between amplitude, frequency, or pressure was conclusive.

8.2 Recommendations

It is recommended to characterise and investigate higher pressure systems up to differentials of 30 bars, where different rubber bellows are used to fully understand the change in dynamic properties of any rubber bellows when subjected to increased pressure loadings. The current experimental setup for example was restricted to only deliver a maximum pressure difference of 50 kPa where the operating range of the bellow is up to 16 bar. This study is based on an in-line rubber bellow application, although the recommendation is to evaluate higher pressure tests with a rubber bellow that is not in-line with the main flow path. Figure 8-1 shows the experimental setup recommended for higher pressure tests, where the single point flow entry and exit can be seen at the bottom of the bellow, and one-way valves are used for flow control.

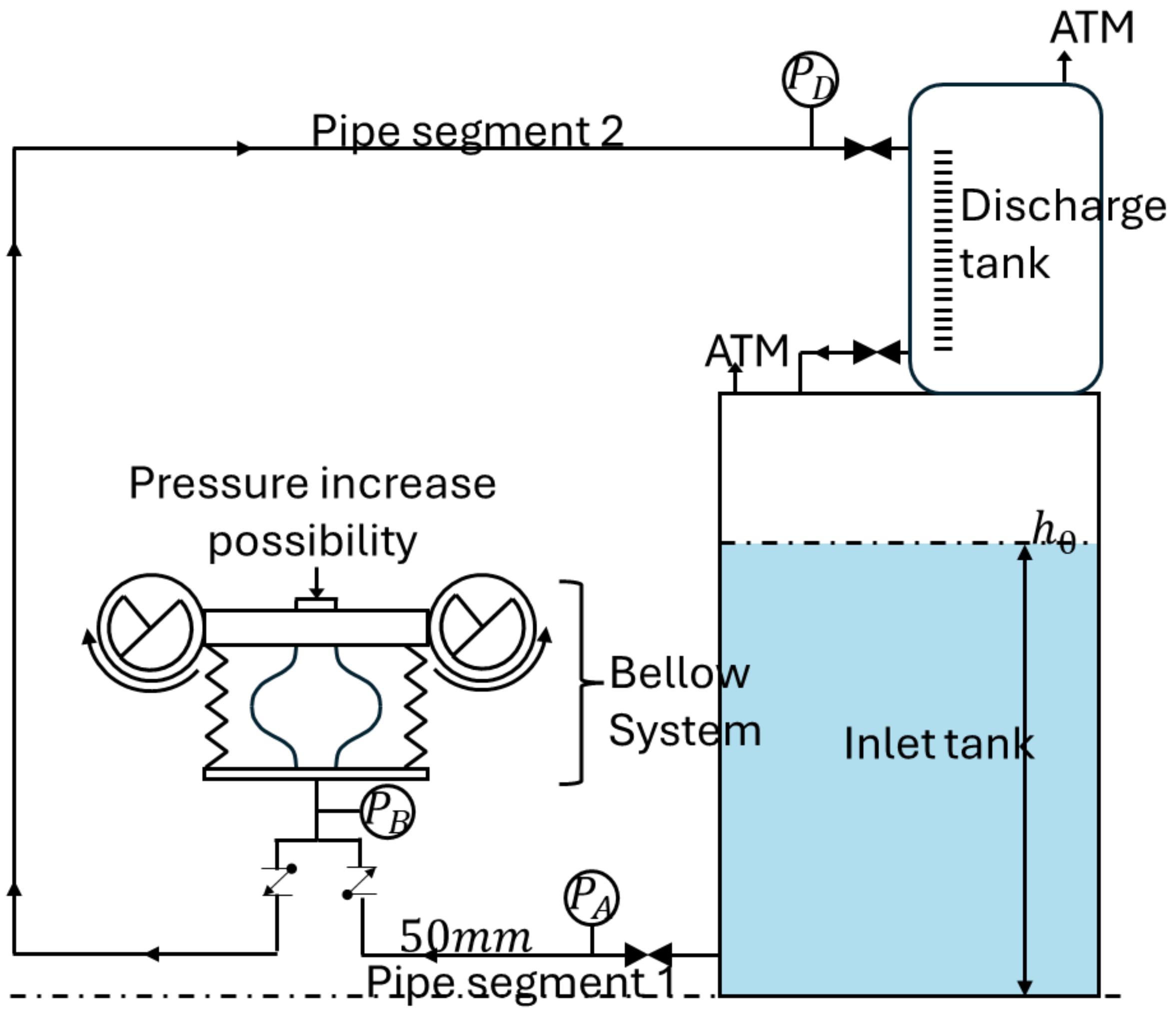

Figure 8-1: High pressure experimental setup recommendation

By removing the in-line application of the bellow, it allows for an additional pressure increasing port as shown in the figure, which will allow for an external increase in pressure in the system.

Another recommendation is to investigate the application of a rubber bellow as a vibration isolator with the function of circulating fluid in an auxiliary system. An example of this is to implement the bellow in a by-pass system that circulates cooling water of a gearbox while implemented as a vibration isolator for the gearbox or surrounding pipelines.

References

Anon. (2016) *Dictionary.com*. Available at: https://www.dictionary.com/browse/fatigue (Accessed: 26 June 2016).

Billcrossland (2009) *Espresso machine Vibration pump*. Available at: https://www.youtube.com/watch?v=we9IZJ5tQFs (Accessed: 29 June 2016).

Blodgett, B. (2015) *The Volumetric Efficiency of Rotary Positive Displacement Pumps*. Available at: https://www.pumpsandsystems.com/volumetric-efficiency-rotary-positive-displacement-pumps (Accessed: 4 June 2016).

Bloem, J. (2015) *Design optimisation and experimental evaluation of a grain vibration screen*. Potchefstroom: North West University of Potchefstroom.

Cai, L.-W. (2016) *Fundamentals of Mechanical Vibrations*. Newark : John Wiley & Sons, Incorporated.

Chai, T., Dreyer, J.T. and Singh, R. (2014) 'Time domain responses of hydraulic bushing with two flow passages', *Journal ofSound and Vibration*, III(333), pp.693-710.

ChangYuanFlex (n.d.) *Installation & Maintenance of Rubber Bellows: A Comprehensive Guide*. Available at: https://changyuanflex.com/technical-articles/expansion-joint/installation-maintenance-of-rubber-bellows-a-comprehensive-guide/ (Accessed: 18 November 2024).

Chen, J. et al. (2013) 'Numerical prediction on volumetric efficiency of progressive cavity pump with fluid-solid interaction model.', *Journal of Petroleum Science and Engineering*, I(109), pp.12-17.

Chennu, V.R. (2016) *Mechanical Engineering*. Available at: https://mechanicalengineering.blog/centrifugal-pump-efficiency/ (Accessed: 13 March 2016).

Cipollone, R. et al. (2015) 'Development of a Sliding Vane Rotary Pump for Engine Cooling', *Energy Procedia*, I(81), pp.775-83.

Douglas, J.F., Gasiorek, J.M. and Swaffield, J.A. (1985) *Fluid Mechanics*. 2nd edn. New York: John Wiley & Sons.

EcosimPro (2014) *Electric_Systems: Electrical, Electronics and Power System Simulation*. Available at: https://www.ecosimpro.com/products/energy-electric-systems/ (Accessed: 5 May 2016).

George, H.F. and George, J.H., (2013) 'The Circulatory system.' *in Schaum's Ouline of Biology*., New York, Chicago, San Francisco, Athens, London, Madrid, Mexico City, Milan, New Delhi, Singapore, Sydney, Toronto: McGraw-Hill Education.

GmbH, g.t. (n.d.) *Impact Hammer WaveHitMAX*. Available at: https://www.gfaitech.com/products/structural-dynamics/impact-hammer-wavehit-max (Accessed: 14 September 2025).

GRI-Pumps (n.d.) *Standard Bellows Metering Pumps - The Pump People*. Available at: https://www.gripumps.com/media/1557/gri-standard-bellows-pumps-overview-0323.pdf (Accessed: 27 November 2025).

Gross, D. et al., (2014) 'Motion of a Point Mass.' *in Engineering Mechanics 3*. Springer, Berlin, Heidelberg., pp.3-86.

Halliday, D., Resnick, R. and Walker, J. (2014) *Principles of Physics*. 10th edn. New York: John Wiley & Sons Inc.

Hausberg, F. et al. (2015) 'Experimental and Analytical Study od Secondary Path Variations in Active Engine Mounts', *Journal of Sound and Vibration*, 340, pp.22-38.

HBM (2017) *U2A Load cell data sheet*. Available at: https://www.hbm.cz/wp-content/uploads/b1000.pdf (Accessed: 9 Sep 2018).

Hibbler, R.C. (2010) *Engineering Mechanics Dynamics*. 12th edn. Singapore: Prentice Hall.

Hosseini, S.S. and Marzbanrad, J. (2017) 'Functional overview of Hydraulic Vehicle Engine mount Classification', *International Journal of Automotive Engineering*, 7(4).

Hutchinsonai (2014) *Hutchinson design consideration*. Available at: https://hutchinsonai.com/testing/ (Accessed: 23 August 2023).

Kim, G. and Singh, R. (1995) 'A study of passive and adaptive hydraulic engine mount system with emphasis on non-linear charaxteristics', *Journal of Sound and Vibration*, 179(3), pp.427-53.

Lin, T.R., Farag, N.H. and Pan, J. (2004) 'Evaluation of frequency dependent rubber mount stiffness and damping by impact test', *Applied Acoustics*, 66(7), pp.829-44.

Lubomirsky, P.I. (2025) *WEIZMANN INSTITUDE OF SCIENCE*. Available at: https://www.weizmann.ac.il/MCMS/igorl/equipment/dma-dynamic-mechanical-analysis (Accessed: 14 September 2025).

Mansour, H. (2010) *Design and development of Active and semi-active engine mounts*. Burnaby BC Canada: Simon Fraser University.

Marscher, W.D. (2020) *TAMU Pump Rotordynamics Tutorial 2020 - Scientific Figure*. Available at: https://www.researchgate.net/figure/Definition-of-Phase-Angle-Figure-3-Relationship-of-Phase-Angle-to-Frequency-of-Vibration_fig1_338458548 (Accessed: 26 October 2026).

Marzbani, H., Jazar, R.N. and Fard, M. (2014) 'Hydraulic engin mounts: a survey', *Journal of vibration and control*, 20(10), pp.1439-63.

Mathworks, i. (n.d.) *Estimating Error, ODE23 | Solving ODEs in MATLAB*. Available at: https://nl.mathworks.com/videos/solving-odes-in-matlab-5-estimating-error-ode23-117536.html (Accessed: 03 October 2024).

Mendia-Garcia, I., Facchinetti , A., Bruni, S. and Gil-Negrete, N. (2023) 'Analysis and modelling of the dynamic stiffness up to 400 Hz of an air spring with a pipeline connected to a reservoir', *Journal of Sound and Vibration*, 557.

Nel, C.B. and Steyn, A.J. (2012) 'Stiffness and Damping Characterisation for a Hydraulic', *Topics in Modal Analysis*, 6(2), pp.129-35.

NETZSCH (2025) *Dynamic Mechanical Analyzers*. Available at: https://analyzing-testing.netzsch.com/en/products/dynamic-mechanical-analysis-dma#:~:text=Dynamic%20Mechanical%20Analysis%20(DMA)%20is%20a%20technique%20used%20to%20measure,Stress%20%3D%20force%2Farea). (Accessed: 14 September 2025).

ORIA (n.d.) *Anti Vibration springs Vs rubber bellow cylinders*. Available at: https://eganagroup.com/oria/en/antivibration-springs-vs-rubber-bellow-cylinders/ (Accessed: 12 October 2025).

Rao, S.S. (2011) *Mechanical Vibrations*. 5th edn. Singapore: Pearson Education Soputh Asia Pte Ltd.

Rubber design B.V. (2021) *Rubber design bellows and compensators*. Available at: https://www.rubberdesign.nl/producs/bellows-compensators/ (Accessed: 8 October 2023).

Sarafrazian, A. (2013) *Model Based Virtual Prototyping for Hydraulic Passive Engine Mount with an Emphasis on Inirtia Track*. Simon Fraser University.

Sjöberg , M. (2002) *ON DYNAMIC PROPERTIES OF RUBBER ISOLATORS*. Stockholm: The Marcus Wallenberg Laboratory for Sound and Vibration Research Department of Vehicle Engineering.

Steyn, A.J. (2011) *Karakterisering en evaluering van 'n hidrouliese enjinmonteerstuk*. Potchefstroom: North West University of Potchefstroom.

Velmurugan, V., Suryakumari, T.S.A., Pandiyan, A. and Jayakumar, V. (2016) 'Modeling and Analysis of Semi-Active Hydraulic Engine Mount Using Finite Element Analysis', *ARPN Journal of Engineering Applied Science*, 11(16).

VENANZETTI-VIBRAZIONI-MILANO (2003) *venanzetti vibrazioni milano srl*. Available at: https://www.bege.nl/downloads/manuals/Venanzetti%20VVC%20Installation%20and%20maintenance%20manual%202003-01%20IT%20EN%20F%20SP%20P%20NL%20D%20DK%20S%20FL%20N%20GR.pdf (Accessed: 27 November 2025).

Vipro (n.d.) *venanzetti-motor_catalogue*. Available at: https://www.vipro.co.za/files/venanzetti-motor_catalogue.pdf (Accessed: 20 November 2024).

Volk, M. (2005) *Pump Characteristics and Applications*. 2nd edn. Taylor & Francis.

Willbrandt-Cummitechnik (n.d.) *Willbrandt.com*. Available at: https://www.willbrandt.com/willbrandt/de/pdf/kompensatoren/typen_gummi_en/Expansion-joints-rubber-Type55_en.pdf?m=1623697684& (Accessed: 11 Augustus 2024).

Yang, B., (2005) 'Vibration Analysis of One-Degree-of-Freedom Systems.' *in Stress, Strain, and Structural Dynamics*., California: Elsevier Inc.., pp.351-435.

Yang, Y., Guang, P., Shaoping, Y. and Ying, Y. (2020) 'Experiment Investigate on the Effectiveness of Flexible Pipes to Isolate Sea-Water Pump Generated Vibration', *Coatings*, 10(1), p.43.

Zheng, Y. et al. (2025) 'Nonlinear frequency response analysis and optimization of vibration systems with air springs and auxiliary chambers', *Journal of Sound and Vibration*, 619.

Appendixes

Appendix A – Bellow Rubber Properties

WILLBRANDT GUMMITECHNIK

WILLBRANDT **Rubber Expansion Joint Type 50**

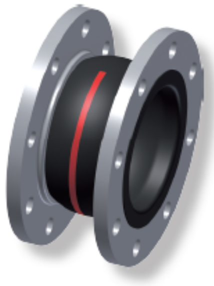

DN 20 - DN 1000

Type 50 is a low-corrugated, highly elastic rubber expansion joint. Its low corrugation helps to achieve very low flow resistance. It reduces up to 70 % of the incoming energy. It is also characterise by very high movement absorption in all directions and variety of rubber qualities, which means that a suitable rubber compound is available for every application.

Type 50 is used in building technology, plant engineering, water and wastewater technology, engine construction, shipbuilding and in solar and and wind plant engineering. It especially used where it is specifically used to absorb expansion and vibration and to insulate sound.

Bellow design	Low-corrugated rubber bellow with reinforcement and shaped sealing bead with core ring, self-sealing (no additional seals required). Suitable for accommodating swiveling flanges.	**Flange version**	Both sides with swiveling flange made of galvanized steel with clearance holes, drilled according to DIN PN 10 (standard). Other materials and dimensions are possible.
		Approvals/Conformity	Similar to DIN 4809 / TÜV approved, drinking water and shipbuilding approval, FDA and EG 1935/2004 conform

Specifications for DN 20 - DN 400

Bellow		Bellow design			up to DN	Permissible operating data									Surface resistance Ro	
Colour code	Colour marking	Core (inner)	Reinforcement	Cover (outer)		°C	bar	°C	bar	°C	bar	°C	bar	Short-term °C	Core Ohm x cm	Cover Ohm x cm
red Sp		EPDM	PEEK	EPDM	400	-40	10	70	16	100	10	130	8	150	4×10^3	4×10^3
red		IIR	Polyamide	EPDM	400	-40	10	50	16	70	12	100	10	120	7 x 10[illegible]	1 x 10[illegible]
red EPDM		EPDM	Polyamide	EPDM	400	-30	10	50	16	70	12	90	10	100	- -	- -
yellow		NBR	Polyamide	CR	400	-20	10	50	16	70	12	90	10	100	2×10^2	1×10^3
white		NBR	Polyamide	CR	400	-20	10	50	16	70	12	90	10	100	7×10^9	1×10^3
green		CSM	Polyamide	CSM	400	-20	10	50	16	70	12	100	10	110	7×10^9	7×10^9
orange		NBR	Polyamide	CR	200	-20	10	50	25	70	20	90	15	100	3×10^3	1×10^3
black EPDM*		IIR	Polyamide	EPDM	150	-40	10	50	10	70	8	90	6	120	7×10^6	1×10^3
black CR	–	CR	Polyamide	CR	400	-25	10	50	16	70	12	90	10	100	7×10^9	5×10^{10}
yellow LT	LT	NBR-LT	Polyamide	CR	300	-40	10	50	16	70	12	90	10	100	1×10^4	4×10^3
yellow St		NBR	Steel cord	CR	400	-20	10	60	16	70	12	90	10	100	2×10^2	5×10^{10}
yellow HNBR		HNBR	Steel cord	CR	300	-35	10	60	16	70	12	100	10	120	$1{,}5 \times 10^5$	$- \; 10^{10}$

Bursting pressure DN 20 - 400 > 48 bar
* Bursting pressure max. 30 bar, max. DN 150

For pressure loss see technical appendix.

Specifications for DN 450 - DN 1000

Bellow		Bellow design			up to DN	Permissible operating data									Surface resistance Ro	
Colour code	Colour marking	Core (inner)	Reinforcement	Cover (outer)		°C	bar	°C	bar	°C	bar	°C	bar	Short-term °C	Core Ohm x cm	Cover Ohm x cm
red Sp		EPDM	PEEK	EPDM	1000	-40	8	70	10	100	7,5	130	6	150	4×10^3	4×10^3
red		IIR	Polyamide	EPDM	1000	-40	8	50	10	70	8	100	6	120	7×10^6	1×10^3
red EPDM		EPDM	Polyamide	EPDM	600	-30	8	50	10	70	8	90	6	100	- -	- -
yellow		NBR	Polyamide	CR	1000	-20	8	50	10	70	8	90	6	100	2×10^2	1×10^3
white		NBR	Polyamide	CR	600	-20	8	50	10	70	8	90	6	100	7×10^9	1×10^3
green		CSM	Polyamide	CSM	1000	-20	8	50	10	70	8	100	6	110	7×10^9	7×10^9
black CR	–	CRN	Polyamide	CR	1000	-25	8	50	10	70	8	90	6	100	7×10^9	5×10^{10}
yellow St		NBR	Steel cord	CR	600	-20	8	60	10	70	8	90	6	100	2×10^2	5×10^{10}

Bursting pressure DN 450 - 1000 > 30 bar

For pressure loss see technical appendix.

Important information

For aggressive media, please see the resistance table (can be requested separately).
The bellows should not be painted or insulated. Please refer to the installation instructions.
++++ We will be happy to send you further information on the individual types and designs. ++++

34

WILLBRANDT **Rubber Expansion Joint Type 50**

Vacuum resistance

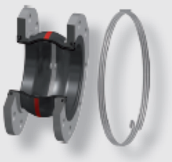

- DN 20 to 50 vacuum-resistant without additional accessories
- DN 65 to 250 without additional accessories to -300 mbar and with vacuum supporting spiral for full vacuum
- DN 300 to DN 1000 only vacuum-resistant with vacuum supporting ring
- Type 50 black EPDM DN 20 to DN 40 without additional accessories to -300 mbar and with vacuum supporting spiral for full vacuum

Accessories

- Guide sleeves
- Potential equalisation
- Flame-resistant protective covers
- Dust and splash protection covers
- Earth cover / sun protection hoods
- Segment tie rods

Application

Type 50 red Sp
For heating installations according to DIN 4809. For many years of operation under constant loading with hot water and heating water at 100 °C/110 °C at 10 bar/6 bar operating pressure. Electrically conductive surface. Not suitable for media with additives containing oil.

Type 50 red
For drinking water, hot water, sea water, cooling water with chemical additives for treating water, saline solutions, weak acids and weak alkaline solutions. Electrically dissipative inner surface and electrically conductive outer surface. Not suitable for oil products or cooling water with additives containing oil.

Type 50 red EPDM
Like Type 50 red, but not for drinking water, shipbuilding and offshore applications. Temperature range max. 90 °C at 10 bar.

Type 50 yellow
For oils, lubricants, fuels, gases, city and natural gas (not liquefied) and DIN EN fuels with an aromatic content up to 50 %. Electrically conductive.

Type 50 white
For foodstuffs containing oil and fat (rubber in food-grade). Not approved for drinking water. Electrically insulating inner surface and electrically conductive outer surface.

Type 50 green
For chemicals, aggressive chemical wastewater and compressor air containing oil. Electrically insulating.

Type 50 orange
Like Type 50 yellow, but also for liquid petroleum gas acc. to DIN EN 589. Electrically dissipative.

Type 50 black EPDM
For drinking water, sea water, cooling water, weak acids and alkali solutions, technical alcohols, esters and ketones. Max. pressure 10 bar. Electrically dissipative inner surface and electrically conductive outer surface.

Type 50 black CR
For hot and cold water, wastewater, swimming pool water, salt water, wastewater, cooling water with anti-corrosive products containing oil, oil mixtures and compressed air containing oil. Electrically insulating.

Type 50 yellow LT
Like Type 50 yellow, but also for liquid gas. Electrically dissipative.

Type 50 lilac
For flue gas desulphurisation systems and bio-diesel. Good resistance to benzene, xylene, toluene, fuels with an aromatic content of more than 50 %, aromatic/chlorinated hydrocarbons and mineral acids. Electrically insulating inner surface and electrically conductive outer surface.

Type 50 yellow St
Like Type 50 yellow with additional flame-resistance for up to 30 minutes at 800 °C. Electrically conductive inner surface, electrically insulating outer surface.

Type 50 yellow HNBR
Like Type 50 yellow St, but for temperatures up to +100 °C. Electrically dissipative inner surface, electrically insulating outer surface.

Note!
Detailed material descriptions on pages 5 - 7.

WILLBRANDT **Rubber Expansion Joint Type 50**

Design A - without tie rods

Can be used for movement absorption in any direction (for combined movements, see the movement diagram in the technical appendix), noise and vibration insulation.

The expansion joint's reaction force must be absorbed via suitable piping.

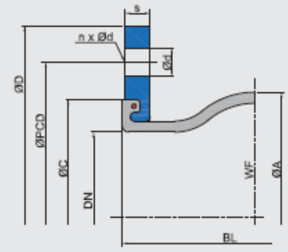

axial -

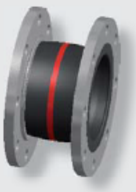

axial +

lateral ±

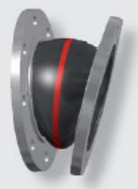

angular ±

Dimensions for Design A

DN	Length	Bellow		Flange PN 10*2						Movement absorption (polyamide cord)				Movement absorption (steel cord)				Weight
	BL	ØA	WF*1	ØD	ØPCD	Ød	n	s	ØC	axial +	axial -	lateral ±	angular ±	axial +	axial -	lateral ±	angular ±	
	mm	mm	mm²	mm	mm	mm		mm	mm	mm	mm	mm	∠°	mm	mm	mm	∠°	kg
20	130	81	1700	105	75	12	4	14	66	30	30	30	30	15	30	15	20	1.5
25	130	81	1700	115	85	14	4	14	66	30	30	30	30	15	30	15	20	1.9
32	130	81	1700	140	100	18	4	15	66	30	30	30	30	15	30	15	20	3.1
40	130	86	1800	150	110	18	4	15	74	30	30	30	30	15	30	15	20	3.5
50	130	96	3200	165	125	18	4	16	86	30	30	30	30	15	30	15	20	3.7
65	130	111	5300	185	145	18	8	16	106	30	30	30	30	15	30	15	20	5.3
80	130	122	8500	200	160	18	8	18	118	30	30	30	30	15	30	15	20	6.8
100	130	142	12800	220	180	18	8	18	138	30	30	30	20	15	30	15	15	7.9
125	130	168	18700	250	210	18	8	18	166	30	30	30	20	15	30	15	15	9.6
150	130	192	25900	285	240	22	8	18	192	30	30	30	20	15	30	15	15	12.9
200	130	252	41000	340	295	22	8	20	252	30	30	30	12	20	15	10	5	16.2
250	130	302	59600	395	350	22	12	20	304	30	30	30	12	20	15	10	5	21.5
300	130	354	82200	445	400	22	12	22	354	30	30	30	12	20	15	10	5	24.5
350	200	420	117600	505	460	22	16	24	412	30	50	30	8	30	30	25	10	38.3
400	200	480	154700	565	515	26	16	25	470	30	50	30	8	30	40	25	5	38.0
450	200	530	204200	615	565	26	20	28	520	30	50	30	8	-	-	-	-	47.2
500	200	580	227900	670	620	26	20	30	570	30	50	30	8	-	-	-	-	56.5
600	200	680	311500	780	725	30	20	30	675	30	50	30	8	-	-	-	-	75.2
700	*3250	800	434200	895	840	30	24	35	780	30	50	30	8	-	-	-	-	127.8
800	250	880	527400	1015	950	33	24	40	887	30	50	30	6	-	-	-	-	161.0
900	300	1038	737900	1115	1050	33	28	40	987	30	50	30	5	-	-	-	-	196.7
1000	300	1138	889400	1230	1160	36	28	40	1087	30	50	30	5	-	-	-	-	234.5

*1 WF = effective area
*2 Other standards/dimensions possible.
*3 Building length 260 mm

Permissible degree of utilisation for movement areas:
- up to 50 °C: Utilisation ~ 100 %
- up to 70 °C: Utilisation ~ 75 %
- up to 90 °C: Utilisation ~ 60 %

Important information

Please note the appropriate f xed point constructions and plain bearings in your piping system!
For more information please refer to our installation instructions.
For information on the tie rods, please see the technical appendix (p. 89 - 92)!
++++ We will be happy to send you further information on the individual types and designs. ++++

WILLBRANDT **Rubber Expansion Joint Type 50**

Length limiters

There is a selection of various length limiters / tie rods to absorb the reaction force and to protect the bellow from overstretching or collapsing:

Design B*
with tie rods

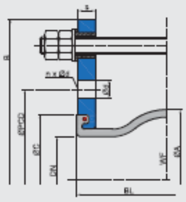

Design C*
with tie rods/thrust limiters

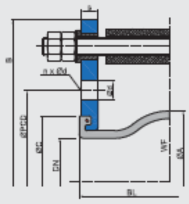

Design E
with tie rods and spherical washers/conical sockets

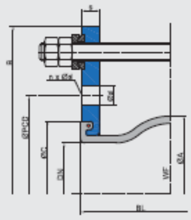

Design M
with tie rods/thrust limiters and spherical washers/conical sockets

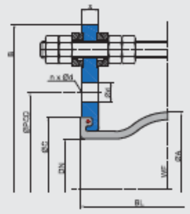

Design F
with hinge

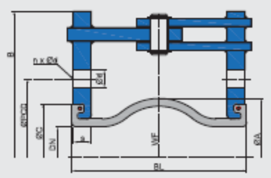

*Note: For Designs B and C
the lateral movement absorption is reduced by around 50 %.

Flange dimensions for Designs with tie rods

DN	Length BL	Flange PN 10 (example dimensions) B	ØD	ØPCD	Ød	n	s	ØC
	mm	mm	mm	mm	mm		mm	mm
20	130	189	105	75	12	4	14	66
25	130	205	115	85	14	4	14	66
32	130	230	140	100	18	4	15	66
40	130	240	150	110	18	4	15	74
50	130	255	165	125	18	4	16	86
65	130	275	185	145	18	8	16	106
80	130	290	200	160	18	8	18	118
100	130	310	220	180	18	8	18	138
125	130	340	250	210	18	8	18	166
150	130	375	285	240	22	8	18	192
200	130	440	340	295	22	8	20	252
250	130	509	395	350	22	12	20	304
300	130	559	445	400	22	12	22	354
350	200	619	505	460	22	16	24	412
400	200	700	565	515	26	16	25	470
450	200	760	615	565	26	20	30	520
500	200	810	670	620	26	20	30	570
600	200	930	780	725	30	20	30	675
700	*250	1045	895	840	30	24	35	780
800	250	1175	1015	950	33	24	40	887
900	300	1285	1115	1050	33	28	40	987
1000	300	1400	1230	1160	36	28	40	1087

* Building length 260 mm

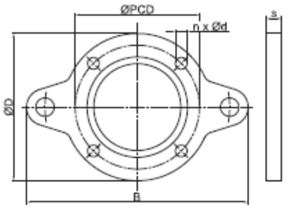

DN 32 - 200

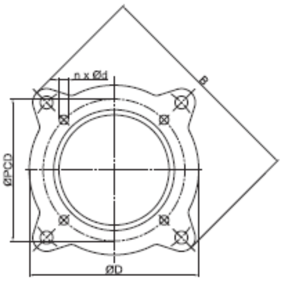

DN 250 - 900

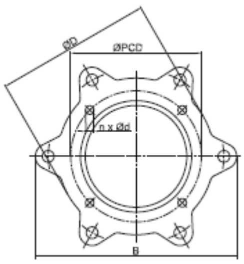

DN 1000

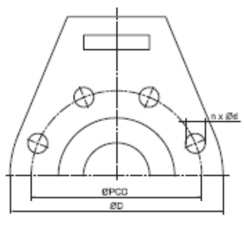

DN 50 - 1000 (Design F)

WILLBRANDT **Rubber Expansion Joint Type 50**

Axial stiffness rates

DN	Overall length BL mm	Stiffness rates (averages value from full way) 0 bar Nm/mm	2,5 bar Nm/mm	4 bar Nm/mm	6 bar Nm/mm	10 bar Nm/mm	16 bar Nm/mm
20	130	31	68	128	192	243	270
25	130	31	68	128	192	243	270
32	130	31	68	128	192	243	270
40	130	30	66	124	186	236	261
50	130	25	51	98	134	173	192
65	130	24	53	100	150	190	211
80	130	28	58	104	148	185	205
100	130	35	71	116	206	274	304
125	130	36	71	137	214	282	313
150	130	49	102	189	293	390	433
200	130	100	180	365	568	735	816
250	130	105	207	388	609	778	864
300	130	123	248	448	658	883	980
350	200	105	177	349	567	753	836
400	200	154	261	516	535	1090	1210
450	200	167	320	581	903	1162	1290
500	200	196	376	686	1060	1364	1514
600	200	208	292	692	1123	1441	1600
700	*250	140	198	521	714	954	-
800	250	180	270	594	975	1258	-
900	300	200	380	690	1080	1395	-
1000	300	225	420	742	1248	1568	-

* Building length 260 mm

Warning: Deviations (+/- 25 %) in the stiffness rates may occur due to use of different materials and manufacturing processes.

Lateral stiffness rates

DN	Overall length BL mm	Stiffness rates (averages value from full way) 0 bar Nm/mm	2,5 bar Nm/mm	4 bar Nm/mm	6 bar Nm/mm	10 bar Nm/mm	16 bar Nm/mm
20	130	64	125	184	240	240	300
25	130	64	125	184	240	240	300
32	130	64	125	184	240	240	300
40	130	62	121	178	233	256	291
50	130	50	65	80	105	145	205
65	130	40	78	115	150	165	188
80	130	35	74	136	155	173	200
100	130	55	88	143	168	192	228
125	130	100	200	261	293	383	518
150	130	120	260	309	366	466	616
200	130	323	723	836	949	1219	1624
250	130	379	806	1022	1173	1479	1938
300	130	392	837	1068	1216	1542	2031
350	200	305	610	762	875	1098	1433
400	200	338	642	817	946	1199	1579
450	200	342	639	821	971	1200	1544
500	200	426	818	1048	1204	1495	1932
600	200	456	834	1062	1295	1586	2023
700	*250	516	939	1191	1449	1775	-
800	250	558	960	1055	1557	1758	-
900	300	800	1480	1984	2248	2560	-
1000	300	960	1824	2361	2736	2976	-

* Building length 260 mm

Warning: Deviations (+/- 25 %) in the stiffness rates may occur due to use of different materials and manufacturing processes.

WILLBRANDT **Rubber Expansion Joint Type 50**

Angular stiffness torque

DN	Overall length BL mm	Stiffness torque (averages value from full way) 0 bar Nm/°	2,5 bar Nm/°	4 bar Nm/°	6 bar Nm/°	10 bar Nm/°	16 bar Nm/°
20	130	0.2	0.5	0.9	1.3	1.7	1.9
25	130	0.2	0.5	0.9	1.3	1.7	1.9
32	130	0.2	0.5	0.9	1.3	1.7	1.9
40	130	0.3	0.6	1.1	1.6	2.0	2.3
50	130	0.3	0.6	1.1	1.6	2.0	2.2
65	130	0.4	0.9	1.7	2.5	3.2	3.6
80	130	1.0	1.0	2.0	3.0	4.0	5.0
100	130	1.0	2.0	4.0	7.0	9.0	10.0
125	130	2.0	3.0	6.0	10.0	13.0	15.0
150	130	3.0	7.0	12.0	19.0	25.0	28.0
200	130	11.0	20.0	41.0	63.0	82.0	91.0
250	130	18.0	35.0	65.0	102.0	130.0	144.0
300	130	29.0	58.0	105.0	154.0	206.0	229.0
350	200	34.0	57.0	113.0	183.0	244.0	270.0
400	200	65.0	110.0	218.0	226.0	460.0	511.0
450	200	87.0	168.0	304.0	473.0	609.0	676.0
500	200	125.0	239.0	436.0	674.0	868.0	963.0
600	200	186.0	261.0	618.0	1004.0	1288.0	1429.0
700	*250	167.0	237.0	861.0	853.0	1140.0	-
800	250	277.0	416.0	914.0	1501.0	1937.0	-
900	300	386.0	733.0	1330.0	2082.0	2689.0	-
1000	300	531.0	991.0	1751.0	2945.0	3700.0	-

* Building length 260 m

Warning: Deviations (+/- 25 %) in the stiffness torque may occur due to use of different materials and manufacturing processes.

Frictional force

DN	Overall length BL mm	For designs E and M Frictional force N/bar	for design F frictional moment Nm/bar
20	130	7	0.2
25	130	7	0.2
32	130	7	0.2
40	130	7	0.2
50	130	12	0.3
65	130	20	0.5
80	130	35	1.0
100	130	51	1.4
125	130	75	2.1
150	130	118	4.4
200	130	167	6.2
250	130	243	11.2
300	130	335	15.4
350	200	120	17.0
400	200	160	22.9
450	200	171	40.5
500	200	266	63.5
600	200	634	138.5
700	*250	662	180.9
800	250	896	326.2
900	250	1105	402.4
1000	250	1357	617.3

* Building length 260 m

Warning: Deviations (+/- 25 %) in the frictional force may occur due to use of different materials and manufacturing processes.

WILLBRANDT **Chemical Expansion Joint Type 50 PTFE**

DN 25 - DN 500

Type 50 PTFE is a low-corrugated, PTFE-lined rubber expansion joint. Its low corrugation helps to achieve very low flow resistance. The PTFE lining gives the expansion joint high chemical resistance or an anti-adhesive property.

The PTFE lining can be used for any rubber compound on Type 50. It is however necessary to ensure that the selected rubber compound achieves the highest possible media resistance, as this is the only way to achieve optimum service life.

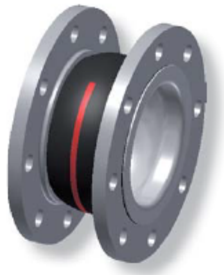

Dimensions for Design A

DN	Length	Bellow		Flange PN 10						Movement absorption				Weight
	BL	ØA	WF*	ØD	ØPCD	Ød	n	s	ØC	axial +	axial -	lateral ±	angular ±	
	mm	mm	mm²	mm	mm	mm		mm	mm	mm	mm	mm	∠°	kg
25	**130**	81	1700	115	85	14	4	14	66	15	15	15	15.0	1.9
32	**130**	81	1700	140	100	18	4	15	66	15	15	15	15.0	3.1
40	**130**	86	1800	150	110	18	4	15	74	15	15	15	15.0	3.5
50	**130**	96	3200	165	125	18	4	16	86	15	15	15	15.0	3.8
65	**130**	111	5300	185	145	18	8	16	106	15	15	15	15.0	5.4
80	**130**	122	8500	200	160	18	8	18	118	15	15	15	15.0	6.9
100	**130**	142	12800	220	180	18	8	18	138	15	15	15	10.0	8.0
125	**130**	168	18700	250	210	18	8	18	166	15	15	15	10.0	9.7
150	**130**	192	25900	285	240	22	8	20	192	15	15	15	10.0	13.1
200	**130**	252	41000	340	295	22	8	20	252	15	15	15	6.0	16.4
250	**130**	302	59600	395	350	22	12	20	304	15	15	15	6.0	21.7
300	**130**	354	82200	445	400	22	12	20	354	15	15	15	6.0	24.8
350	**200**	420	117600	505	460	22	16	24	412	15	15	15	4.0	38.8
400	**200**	480	154700	565	515	26	16	25	470	15	15	15	4.0	38.6
450	**200**	530	204200	615	565	26	20	28	520	15	15	15	4.0	49.3
500	**200**	580	227900	670	620	26	20	30	570	15	15	15	4.0	57.2

* WF = effective area

Permissible degree of utilisation for movement areas:
- up to 50 °C: Utilisation ~ 100 %
- up to 70 °C: Utilisation ~ 75 %
- up to 90 °C: Utilisation ~ 60 %

Pressure resistance	Max. 6 bar operating pressure with polyamide cord reinforcement, max. 9 bar operating pressure with aramid or steel cord reinforcement.
Conformity	FDA and EG 1935/2004
Vacuum resistance	Only limited suitable for vacuum operation. A PTFE vacuum supporting ring, which allows full vacuum for small nominal diameters, can be used from DN 50. The PTFE supporting ring can only be used up to 50 °C. DN 25, DN 32, DN 40 and DN 350 expansion joints are not suitable for vacuum operation.

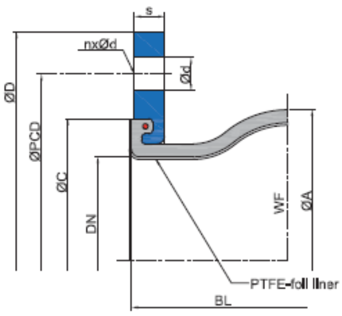

Important information

For aggressive media, please see the resistance table (can be requested separately).
The bellows should not be painted or insulated. Please refer to the installation instructions.
++++ We will be happy to send you further information on the individual types and designs. ++++

Appendix B – MATLAB scripts

The following sub routine programs are listed in the appendix.

B-1 Phase angle calibration, where the phase angle is calibrated.

B-2 Signal FFT, where the FFT signals is extracted, and the phase angle and amplitude are calculated, the expected steady state- (B-2.1) and transient- behaviour (B-2.2) is then plotted.

B-3 Dynamic properties of bellow system, where the dynamic properties of the system are calculated.

B-4 Vibration energy and power, where the energy and power of the system is calculated for steady state- (B-4.1) and transient- behaviour (B-4.2) are calculated.

B-5 Fluid flow energy, where the fluid energy of the system is calculated.

B-6 Fluid energy transfer ratio

B-1 Phase Angle Calibration

```
clear all

%%-----Input values------%%

%%Load of measured data%%

filename1_eik = 'EC503A.dat';                    %Define acceleration file
name for calibration process
filename2_eik = 'EC503B.dat';                    %Define eddy current signal
file name for calibration process

%%---------------------------------------------------------------------------
---------%%
%%                          Phase angle Calibration
%%
%%---------------------------------------------------------------------------
---------%%


tt1_eik = load(filename1_eik);                       %Load acceleration data
from file
t1_eik=tt1_eik(:,2);                                 %Define time array of
data from signal[s]
Ro1_eik=9.81*tt1_eik(:,1);                           %Define acceleration
array of data from signal and convert Gs to [m/s^2]

tt2_eik = load(filename2_eik);                       %Load Eddy current
signal data from file
t2_eik=tt2_eik(:,2);                                 %Define time array of
data [s]
Ro2_eik= tt2_eik(:,1);                               %Define eddy current
voltage array of data [V]
```

```
fs1_eik=1/t1_eik(2);                                    %Sample frequency of
acceleration [Hz]
fs2_eik=1/t2_eik(2);                                    %Sample frequency of
Eddy current signal [Hz]

np1_eik=length(t1_eik);                                 %Sample total time of
data [s]
f1_eik=fs1_eik*(0:np1_eik-1)/np1_eik;                   %Frequency domain [Hz]

np2_eik=length(t2_eik);                                 %Sample total time of
data [s]
f2_eik=fs2_eik*(0:np2_eik-1)/np2_eik;                   %Frequency domain [Hz]

len1_eik = (np1_eik/2.56)+1;                            %Define number of data
points in acceleration signal measured
len2_eik = (np2_eik/2.56)+1;                            %Define number of data
points in Eddy current signal measured

FRo1_eik=fft(Ro1_eik);                                  %Discrete Fourier
transform of acceleration signal
PRo1_eik=abs(FRo1_eik)*2/np1_eik;                       %Determine acceleration
amplitude of fft at each frequency
aRo1_eik=angle(FRo1_eik);                               %Determine phase angle
at each frequency
npl_eik=1:(len1_eik);                                   %Declare range of
frequency

FRo2_eik=fft(Ro2_eik);                                  %Discrete Fourier
transform of Eddy current signal
PRo2_eik=abs(FRo2_eik)*2/np2_eik;                       %Determine Eddy current
amplitude of fft at each frequency
aRo2_eik=angle(FRo2_eik);                               %Determine phase angle
at each frequency
np2_eik=1:(len2_eik);                                   %Declare range of
frequency


%Array data points of FFT%%

datRo1_eik=[2*pi*f1_eik(npl_eik); PRo1_eik(npl_eik)'; aRo1_eik(npl_eik)'];
datRo2_eik=[2*pi*f2_eik(np2_eik); PRo2_eik(np2_eik)'; aRo2_eik(np2_eik)'];


%%Reconstruction of signals%%
for j=1:np1_eik;
Ros1_eik(j)=sum(datRo1_eik(2,:).*cos(datRo1_eik(1,:)*t1_eik(j)+datRo1_eik(3
,:)));
Ros2_eik(j)=sum(datRo2_eik(2,:).*cos(datRo2_eik(1,:)*t2_eik(j)+datRo2_eik(3
,:)));
end

%%Determine dominant frequency, corresponding amplitude and phase angle%%

[sortedX_eik, sortedInds_eik] = sort(PRo1_eik(:),'descend');    %Sort
maximum accelerations
top4_eik = sortedInds_eik(1:4);                                 %Sort top 4
```

```
%List dominant frequencies from 1 to 4
FF1_eik = f1_eik(top4_eik(1));
FF2_eik = f1_eik(top4_eik(2));
FF3_eik = f1_eik(top4_eik(3));
FF4_eik = f1_eik(top4_eik(4));

maxXValue_eik = FF1_eik;                                          %Dominant
frequency [Hz]
phi1_eik = aRo1_eik(top4_eik(1));                                 %Phase
angle at dominant frequency of acceleration [rad]
phi2_eik = aRo2_eik(top4_eik(1));                                 %Phase
angle at dominant frequency of Eddy current probe [rad]

f_dom_eik = maxXValue_eik                                         %Dominant
frequency of eik signals
phi_acc_eik = phi1_eik*180/pi;                                    %Convert
phase angle of acceleration at dominant frequency to [deg]
phi_ec_eik = phi2_eik*180/pi;                                     %Convert
phase angle of Eddy current at dominant frequency to [deg]
deltaphi_eik = phi_ec_eik-phi_acc_eik                             %Eik phase
angle [deg]

X_eik = (max(PRo1_eik(npl_eik))/((maxXValue_eik*2*pi)^2));
%Displacement amplitude of dominant frequency [m]
RosddotX_eik =
(max(PRo1_eik(npl_eik)))*cos(t1_eik*maxXValue_eik*2*pi+phi1_eik);
%Reconstruction of acceleration signal
RosX_eik = -
(max(PRo1_eik(npl_eik))/((maxXValue_eik*2*pi)^2))*cos(t1_eik*maxXValue_eik*
2*pi+phi1_eik);  %Reconstruction of displacement signal

%Plot original signals along with reconstructed signals%%

figure
subplot(2,1,1)
plot(t1_eik,Ros1_eik,t1_eik,Ro1_eik,'g')
title('EIK Acceleration signal vs reconstructed')
xlabel('Time [s]')
ylabel('Acceleration [m/s^2]')
legend('Reconstructed','Acceleration meter')
subplot(2,1,2)
plot(t2_eik,Ros2_eik,'r',t2_eik,Ro2_eik,'g')
title('EIK Eddy current signal vs reconstructed')
xlabel('Time [s]')
ylabel('Volts')
legend('Reconstructed','Optical eye')
```

B-2 Signal FFT

B-2.1 Steady-state

```
clear all

%%-----Input values------%%

%%Load of measured data%%

filename1 = 'VPT105A.dat';                    %Define acceleration file
name of measured signal
filename2 = 'VPT105B.dat';                    %Define eddy current
signal file name measured signal

%%-------------------------------------------------------------------------
----------%%
%%                 Determine phase angle and X
%%
%%-------------------------------------------------------------------------
----------%%

tt1 = load(filename1);                   %Load accelaration data from
file
t1=tt1(:,2);                             %Define time array of data [s]
Ro1=9.81*tt1(:,1);                       %Define acceleration array of
data and convert G to [m/s^2]

tt2 = load(filename2);                   %Load Eddy cunnert signal data
from file
t2=tt2(:,2);                             %Define time array of data [s]
Ro2= tt2(:,1);                           %Define eddy current voltage
array of data [V]

fs1=1/t1(2);                             %Sample frequency of
acceleration [Hz]
fs2=1/t2(2);                             %Sample frequency of Eddy
current signal [Hz]

np1=length(t1);                          %Sample total time of data [s]
f1=fs1*(0:np1-1)/np1;                    %Frequency domain [Hz]

np2=length(t2);                          %Sample total time of data [s]
f2=fs2*(0:np2-1)/np2;                    %Frequency domain [Hz]

len1 = (np1/2.56)+1;                     %Define number of data points
in acceleration signal measured
len2 = (np2/2.56)+1;                     %Define number of data points
in Eddy current signal measured

FRo1=fft(Ro1);                           %Discrete Fourier transform of
acceleration signal
PRo1=abs(FRo1)*2/np1;                    %Determine acceleration
amplitude of fft at each frequency
aRo1=angle(FRo1);                        %Determine phase angle at each
frequency
npl=1:(len1);                            %Declare range of frequency
```

```
FRo2=fft(Ro2);                              %Discrete Fourier transform of
Eddy current signal
PRo2=abs(FRo2)*2/np2;                       %Determine Eddy current
amplitude of fft at each frequency
aRo2=angle(FRo2);                           %Determine phase angle at each
frequency
np2=1:(len2);                               %Declare range of frequency

%Array data points of FFT%%

datRo1=[2*pi*f1(npl); PRo1(npl)'; aRo1(npl)'];
datRo2=[2*pi*f2(np2); PRo2(np2)'; aRo2(np2)'];


%%Reconstruction of signals%%
for j=1:np1;
Ros1(j)=sum(datRo1(2,:).*cos(datRo1(1,:)*t1(j)+datRo1(3,:)));
Ros2(j)=sum(datRo2(2,:).*cos(datRo2(1,:)*t2(j)+datRo2(3,:)));
end

%%Determine dominant frequency and corresponding aplitude and phase angle%%

[sortedX, sortedInds] = sort(PRo1(:),'descend');    %Sort maximum
accelerations
top4 = sortedInds(1:4);                             %Sort top 4

%List dominant frequencies from 1 to 4

FF1 = f1(top4(1));
FF2 = f1(top4(2));
FF3 = f1(top4(3));
FF4 = f1(top4(4));

maxXValue = f1(top4(1));                            %Dominant frequency
[Hz]
phi1 = aRo1(top4(1));                               %Phase angle at
dominant frequency of acceleration [rad]
phi2 = aRo2(top4(1));                               %Phase angle at
dominant frequency of Eddy current probe [rad]

f = maxXValue                                       %Dominant frequency of
signals
phi_acc = phi1*180/pi;                              %Convert phase angle of
acceleration at dominant frequency to [deg]
phi_ec = phi2*180/pi;                               %Convert phase angle of
Eddy current at dominant frequency to [deg]
deltaphi = phi_ec-phi_acc                           %Eik phase angle [deg]

X = (max(PRo1(npl))/((maxXValue*2*pi)^2))           %Displacement amplitude
of dominant frequency [m]
RosddotX = (max(PRo1(npl)))*cos(t1*maxXValue*2*pi+phi1);    %Reconstruction
of acceleration signal
RosX = -(max(PRo1(npl))/((maxXValue*2*pi)^2))*cos(t1*maxXValue*2*pi+phi1);
%Reconstruction of displacement signal

%%Plot original signals along with reconstructed signals%%

figure
subplot(2,1,1)
```

```
plot(t1,Ros1,t1,Ro1,'g')
title('Acceleration signal vs reconstructed')
xlabel('Time [s]')
ylabel('Acceleration [m/s^2]')
legend('Reconstructed','Acceleration meter')
subplot(2,1,2)
plot(t2,Ros2,'r',t2,Ro2,'g')
title('Eddy current signal vs reconstructed')
xlabel('Time [s]')
ylabel('Volts')
legend('Reconstructed','Optical eye')
```

B-2.2 Transient

```
clear all

%%-----Input values------%%

%%Load of measured data%%

filename1 = 'VPT101A.dat';                %Define acceleration file
name of measured signal
filename2 = 'VPT101B.dat';                %Define eddy current
signal file name measured signal

%%--------------------------------------------------------------------------
---------%%
%%                    Determine maximum X
%%
%%--------------------------------------------------------------------------
---------%%

tt1 = load(filename1);                %Load acceleration data from
file
t1=tt1(:,2);                          %Define time array of data [s]
Ro1=9.81*tt1(:,1);                    %Define acceleration array of
data and convert G to [m/s^2]

tt2 = load(filename2);                %Load Eddy current signal data
from file
t2=tt2(:,2);                          %Define time array of data [s]
Ro2= tt2(:,1);                        %Define eddy current voltage
array of data [V]

fs1=1/t1(2);                          %Sample frequency of
acceleration [Hz]
fs2=1/t2(2);                          %Sample frequency of Eddy
current signal [Hz]

np1=length(t1);                       %Sample total time of data [s]
f1=fs1*(0:np1-1)/np1;                 %Frequency domain [Hz]

np2=length(t2);                       %Sample total time of data [s]
f2=fs2*(0:np2-1)/np2;                 %Frequency domain [Hz]

len1 = (np1/2.56)+1;                  %Define number of data points
in acceleration signal measured
```

```
len2 = (np2/2.56)+1;                            %Define number of data points
in Eddy current signal measured

FRo1=fft(Ro1);                                  %Discrete Fourier transform of
acceleration signal
PRo1=abs(FRo1)*2/np1;                           %Determine acceleration
amplitude of fft at each frequency
aRo1=angle(FRo1);                               %Determine phase angle at each
frequency
npl=1:(len1);                                   %Declare range of frequency

FRo2=fft(Ro2);                                  %Discrete Fourier transform of
Eddy current signal
PRo2=abs(FRo2)*2/np2;                           %Determine Eddy current
amplitude of fft at each frequency
aRo2=angle(FRo2);                               %Determine phase angle at each
frequency
np2=1:(len2);                                   %Declare range of frequency

%Array data points of FFT%%

datRo1=[2*pi*f1(npl); PRo1(npl)'; aRo1(npl)'];
datRo2=[2*pi*f2(np2); PRo2(np2)'; aRo2(np2)'];


%%Reconstruction of signals%%
for j=1:np1;
Ros1(j)=sum(datRo1(2,:).*cos(datRo1(1,:)*t1(j)+datRo1(3,:)));
Ros2(j)=sum(datRo2(2,:).*cos(datRo2(1,:)*t2(j)+datRo2(3,:)));
end

%%Determine maximum acceleration of signal%%

ddotX_abs = abs(Ro1);
ddotX_max = max(ddotX_abs)


%%Plot original signals along with reconstructed signals%%

figure
plot(t1,Ro1)
title('Transient acceleration')
xlabel('Time [s]')
ylabel('Acceleration [m/s^2]')
legend('Acceleration meter')

figure
subplot(2,1,1)
plot(t1,Ros1,t1,Ro1,'g')
title('Acceleration signal vs reconstructed')
xlabel('Time [s]')
ylabel('Acceleration [m/s^2]')
legend('Reconstructed','Acceleration meter')
subplot(2,1,2)
plot(t2,Ros2,'r',t2,Ro2,'g')
title('Eddy current signal vs reconstructed')
xlabel('Time [s]')
ylabel('Volts')
legend('Reconstructed','Optical eye')
```

B-3 Dynamic Properties of Bellow system

```
clear all

%%-----Input values------%%

f = 25;                                               %Frequency [Hz]
deg = -20;                                            %Phase angle [deg]
X = 0.0034;                                           %Displacement amplitude [m]


%%Vibration input parameters%%

n = 100;                                              %Persentage unbalance set
[%]
m_p = 58;                                             %Mass on top of bellow [kg]
m_er_e = 0.087;                                       %Unbalance force of 1 motor
[kgm]

%%----------------------------------------------------------------------------
---------%%
%%                       Determine k_p and zeta
%%
%%----------------------------------------------------------------------------
---------%%

%%INPUT CALCULATIONS%%

%deg = deltaphi - deltaphi_eik       %Calculate phase angle [Deg]

phi = deg*(pi/180);                 %Phase angle [rad]
omega= f*2*pi;                      %Frequency [rad/s]
F_e = 2*(n/100)*m_er_e*omega^2;     %Unbalance force of motors [N]

%%Calculate dynamic properties%%

syms k c;                                                   %Declare two
variables

%%Solve two equations simultaneously%%

eq1 = ((F_e)/(sqrt((k-m_p*(omega)^2)^2+(c*omega)^2)))-X ;   %First equation
eq2 = atan((c*omega)/(k-m_p*(omega)^2))-phi;                %Second
equation

[c,k] = solve(eq1,eq2);                                     %Solve
simultaneously with build in function

Styfheid1 = double(k);                                      %List two
senarios for stiffness
Demping1 = double(c);                                       %List two
senarios for damping

%%Damping coefficient must be positive because from eq1 it is seen that c
has a square root relationship to k%%
```

```
c_p = max(Demping1);                                          %Damping
coeficient [Ns/m]

%%Determine stiffness that matched the corresponding damping%%

if Demping1(1) == c_p
    k_p = abs(Styfheid1(1))                                   %Stiffness
coefficient [N/m]
else
    k_p = abs(Styfheid1(2))                                   %Stiffness
coeficient [N/m]
end

%%Test if stiffness and damping coefficient are correct%%

X_test = (F_e)/(sqrt((k_p-m_p*omega.^2)^2+(c_p*omega).^2)) %Test
displacement amplitude from k_p and c_p determined [m]
f_n = (sqrt(k_p/m_p))/(2*pi)                                 %Natural
frequency [Hz]

%%Logic test if calculated amplitude and measured amplitude is equal to
one%%
%%another or at least within 0.1 mm of each other and if natural
frequency%%
%%is a logical lower than 20 [Hz]%%

if (abs(X_test-X)<0.0001 && f_n < 20)
    mb = msgbox('Test match','sucess');                    %Display message
box if test matches
else
    mb = msgbox('k value wrong','Error','error');          %Display message
box if test is failed
end

%%Determine damping ratio and critical damping coefficient%%

c_c = 2*sqrt(k_p*m_p);                                     %Critical viscous
damping [Ns/m]
zeta = c_p/c_c                                             %Damping ratio [-]
```

B-4 Vibration Energy and Power

B-4.1 Steady-State

```
clear all

%%Vibration input parameters%%

n = 100;                                        %Persentage unbalance set
[%]
m_p = 58;                                       %Mass on top of bellow [kg]
m_er_e = 0.087;                                 %Unbalance force of 1 motor
[kgm]
f = 25;                                         %Frequency [Hz]

X = 2e-3;                                       %Displacement amplitude [m]
k_p = 136e3;                                    %Stiffness of bellow [N/m]
zeta = 0.12;                                    %Damping ratio of bellow [-
]
deg = -10;                                      %Phase angle [Deg]

%%---------------------------------------------------------------------------
---------%%
%%                        Power and energy
%%
%%---------------------------------------------------------------------------
---------%%

%%-------------------------------INPUT CALCULATIONS-------------------------
--%%

omega = 2*pi*f;                         %Frequency [rad]
c_c = 2*sqrt(k_p*m_p);                  %Critical viscous damping [Ns/m]
c_p = zeta*c_c;                         %Damping coefficient of bellow
[Ns/m]
F_T = sqrt((k_p*X)^2+(c_p*omega*X)^2);  %Force transmitted [N]
phi = deg*(pi/180);                     %Phase angle [rad]


%%---------------------------FURTHER CALCULATIONS---------------------------
-%%

c = f*50;                               %Time variable size [s]
b = 0.8;                                %Interval size of calculations [s]
a = (1/f)/c;                            %Start time [s]

t = linspace(a,b,c);                    %Declare time domain [s]

x = X*sin(omega*t-phi);                 %Displacement [m]
dotx = omega*X*cos(omega*t-phi);        %Velocity [m/s]
ddotx = -omega^2*X*sin(omega*t-phi);    %Acceleration [m/s^2]

F = k_p*x + c_p*dotx + m_p*ddotx;       %Differential equation of motion
[N]
F_p_k = k_p*x;                          %Stiffness force [N]
F_p_c = c_p*dotx;                       %Damping force [N]
F_p_m = m_p*ddotx;                      %Mass force {N]
P = F.*dotx;                            %Power [Watt]
```

```
P_v_k = F_p_k.*dotx;                    %Stiffness power [Watt]
P_v_c = F_p_c.*dotx;                    %Damping power [Watt]
P_v_m = F_p_m.*dotx;                    %Mass power [Watt]

P_v = (1/2)*c_p*omega^2*X^2             %Mean power delivered [W]
PP_v = mean(P);                         %Mean power delivered determined

DeltaW_v = c_p.*omega.*X^2.*pi          %Energy dissipated in one cycle [J]

%%---------------------------------------Plot signals----------------------
----%%

%%Plot power signals%%

figure
subplot(4,1,1)
plot(t,P,'g',t,P_v_k,'b',t,P_v_c,'r',t,P_v_m,'c',t,mean(P),'g*',t,mean(P_v_
k),'b*',t,mean(P_v_c),'ro',t,mean(P_v_m),'co')
title('Power components')
xlabel('Time [s]')
ylabel('[Watt]')
legend('Power delivered','Spring power','Damper power','Mass power') %
subplot(4,1,2)
plot(t,P,'g',t,P_v_c,'r',t,mean(P),'g*')
title('Compare dissipated Power')
xlabel('Time [s]')
ylabel('Power [W]')
legend('Power delivered','Damping power')
subplot(4,1,3)
plot(t,F,'g')
title('Force delivered')
xlabel('Time [s]')
ylabel('Force [N]')
legend('Force excitation')
subplot(4,1,4)
plot(t,ddotx,'g')
title('Acceleration')
xlabel('Time [s]')
ylabel('Acceleration [m/s^2]')
legend('Acceleration')
```

B-4.2 Transient Behaviour

B-4.2.1 Script File

```
clear all

global k_p zeta m_p f m_er_e n omega F_e c_c c_p phi

%%---------------------------------INPUT VALUES----------------------------
---%%

k_p = 131.81e3;          %Dynamic system stiffness [N/m]
zeta = 0.1713;           %Damping ratio [%]
m_p = 58;                %Mass on top of system [kg]
m_er_e = 0.087;          %Unbalance force of 1 motor [kgm]
n = 20;                  %Persentage unbalance set [%]
f = 25;                  %Frequency

%%-------------------------------INPUT CALCULATIONS------------------------
--%%

omega = f*2*pi();                         %Frequency [rad/s]
F_e = 2*(n/100)*m_er_e*omega^2;           %Unbalance force of motors [N]
c_c = 2*sqrt(k_p*m_p);                    %Critical viscous damping [Ns/m]
c_p = c_c.*zeta;                          %Viscous damping of system [Ns/m]
phi = atan((c_p*omega)/(k_p-m_p*omega^2));  %Phase angle [rad]
deg = phi*180/pi
%%-----------------Declare numerical integration boundary conditions-------
--%%

Y0 = [0 0];                  %Assign boundary conditions for each array

domain = 0:1/(25*100):20/25; %Declare domain of numerical integration

[tt,y] = ode23('RungakuttaMotor_rev5_final',domain,Y0); %Internal numerical
integration MATLAB function

%------------------------Convert to desired variables-----------------%%

x = y(:,1);                                         %Displacement [m]
dotx = y(:,2);                                      %Velocity [m/s]
ddotx = ((F_e*sin(omega*tt)-(k_p)*x-(c_p)*dotx)/m_p);   %Acceleration
[m/s^2]

%-------------------------Power Calculations--------------------------%%

F = k_p*x + c_p*dotx + m_p*ddotx; %Force [N]
F_p_k = k_p*x;                 %Stiffness force [N]
F_p_c = c_p*dotx;              %Damping force [N]
F_p_m = m_p*ddotx;             %Mass force {N]
P = F_e*sin(omega*tt).*dotx;   %Equivalent power [W]
P_v_k = F_p_k.*dotx;             %Stiffness power [Watt]
P_v_c = F_p_c.*dotx;             %Damping power [Watt]
P_v_m = F_p_m.*dotx;             %Mass power [Watt]

%-----------------------Maximum power Calculations-------------------------
-%%
```

```
ddotx_abs = abs(ddotx);
%Determmine absolute values of acceleration [m/s^2]
P_abs = abs(P);                                                   %Determine
absolute values of power [W]

ddotx_max = max(ddotx_abs)                                        %Maximum
acceleration of System [m/s^2]
P_max = max(P_abs)                                                %Maximum
power of system [W]

%-----------------------Plots-----------------------------%

figure                                           %Plot transient
displacement
plot(tt,x,'g')
title('Transient displacement')
xlabel('Time [s]')
ylabel('[m]')
legend('Displacement')

figure                                           %Plot transient velocity
plot(tt,dotx,'g')
title('Transient velocity')
xlabel('Time [s]')
ylabel('[m/s]')
legend('Velocity')

figure                                           %Plot transient
acceleration
plot(tt,ddotx,'g')
title('Transient acceleration')
xlabel('Time [s]')
ylabel('[m/s^2]')
legend('Acceleration')

figure                                           %Plot transient power
plot(tt,P,'g')
title('Transient vibration power')
xlabel('Time [s]')
ylabel('Power [W]')
legend('Power')

figure                                           %Plot power
plot(tt,P,'g',tt,P_v_k,'b',tt,P_v_c,'r',tt,P_v_m,'c')
title('Power')
xlabel('Time [s]')
ylabel('Power [Watt]')
legend('Equivalent','Spring power','Damper power','Mass power')
```

B-4.2.2 Function

```
function r = RungakuttaMotor_rev5_final(tt,y)

global k_p zeta m_p f m_er_e n omega F_e c_c c_p phi


%----------------------------NUMERICAL INTEGRATION--------------------%%

r = zeros(2,1);            %Create array of zeros

r(1) = y(2);               %Integrate velocity to displacement
r(2) = ((F_e.*sin(omega.*tt))-k_p.*y(1)-c_p.*y(2))/m_p; %Integrate
acceleration to velocity


end
```

B-5 Fluid-Flow Power

```
clear all

%%-----Input values------%%

X = 0.0034;                                       %Displacement amplitude [m]
f = 25;                                           %Frequency [Hz]
deg = -20;                                        %Phase angle [Deg]
P_v = 392;                                        %Vibration power [W]

%%Flow input parameters%%

P_A = 0;                                          %Gauge pressure in inlet
pipe [Pa]
P_D = 20e3;                                       %Guage pressure at
discharge end of cycle [Pa]
P_B = 65e3;                                       %Maximum gauge pressure
inside of bellow [Pa]

Q = (10/29.84)*10^(-3);                           %Measured flow rate [m^3/s]

P_Dv = 178e3;                                     %Pressure built up in
discharge pipe with no flow [Pa]
P_Bv = 245e3;                                     %Pressure supplied by the
bellow with no flow [Pa]

h_0 = 0.55;                                       %Height of water level in
inlet tank [m]
h_A = 0.395;                                      %Height of inlet pressure
gauge [m]
h_B = 0.175;                                      %Height of bellow inlet [m]
h_C = 0.590;                                      %Height of bellow outlet
[m]
h_D = 1.28;                                       %Height of outlet pressure
gauge [m]
```

```
D_1 = 0.05;                                    %Bellow inlet steel pipe
diameter [m]
D_2 = 0.05;                                    %Bellow outlet steel pipe
diameter [m]

l_1 = 1.08;                                    %Length of inlet pipe [m]
l_2 = 1.12;                                    %Length of discharge pipe
[m]

epsilon = 0.15*10^(-3);                        %Equivalent roughness of
galvinized iron [m]

P_atm = 86e3;                                  %Atmospheric pressure

g = 9.81;                                      %Gravitational acceleration
[m/s^2]
rho = 1000;                                    %Density of fluid [kg/m^3]
mu = 1.002e-3;                                 %Dynamic viscosity of fluid
[N.s/m^2]


%%---------------------------------------------------------------------------
---------%%
%%                            Flow energy
%%
%%---------------------------------------------------------------------------
---------%%

%%Input Calculations%%

phi = (deg/180)*pi;                    %Phase angle [rad]

c = f*50;                              %Time variable size [s]
b = 0.8;                               %Interval size of calculations [s]
a = (1/f)/c;                           %Start time [s]

t = linspace(a,b,c);                   %Declare time domain [s]

omega = 2*pi*f;                        %Frequency [rad/s]

x = X*sin(omega*t-phi);                %System displacement [m]
dotx = omega*X*cos(omega*t-phi);       %System velocity [m/s]
ddotx = -omega^2*X*sin(omega*t-phi);   %System acceleration [m/s^2]

DeltaV = Q/f;                      %Volume displaced by system per cycle
[m^3]

A_p = DeltaV/(2*X);                %Area of equivalent piston [m^2] where
Vol is the volume displacement
D_p = sqrt((4*A_p)/pi)             %Diameter of equivalent piston


A_1 = (pi/4)*D_1^2;                %Area of inlet pipe [m^2]
A_2 = (pi/4)*D_2^2;                %Area of discharge pipe [m^2]


%%Determine velocity and acceleration of fluid in pipe where v
=(A_p/A)dotx_p as the law of continuety%%
```

```
v_1 = (A_p/A_1)*dotx;                 %Velocity of fluid in suction pipe
[m/s]
v_2 = (A_p/A_2)*dotx;                 %Velocity of fluid in delivery pipe
[m/s]

a_1 = (A_p/A_1)*ddotx;                %Acceleration of fluid in suction pipe
[m/s^2]
a_2 = (A_p/A_2)*ddotx;                %Acceleration of fluid in delivery pipe
[m/s^2]



%%Determine static head required to overcome inertia of fluid

h_i1 = -(l_1/g)*a_1;                 %Acceleration head of inlet stage [m]
h_i2 = -(l_2/g)*a_2;                 %Acceleration head of discharge stage
[m]


%%Determine frictional head loss due to pulsating fluid

Re_1 = rho*Q*D_1/(A_1*mu);           %Reynolds number in suction pipe [-]
Re_2 = rho*Q*D_2/(A_2*mu);           %Reynolds number in delivery pipe [-]


%%Determine friction factor
if Re_1 < 2100                        %For laminar flow
    f_1 = 16/Re_1;                    %Friction factor of inlet pipe [-]
else                                  %For turbulant flow- assume that
transitional are 2100<Re<4000 is also turbulant
    f_i1 = (-1.8*log((((epsilon/D_1)/3.7)^1.11)+6.9/Re_1)); %Equation is
f_i1 = 1/sqrt(f), just rewritten to simplify
    f_1 = (1/f_i1)^2;                 %Friction factor of inlet pipe [-]
end

if Re_2 < 2100                        %For laminar flow
    f_2 = 16/Re_2;                    %Friction factor for discharge pipe [-]
else                                  %For turbulant flow
    f_i2 = (-1.8*log((((epsilon/D_2)/3.7)^1.11)+6.9/Re_2)); %Equation is
f_i1 = 1/sqrt(f), just rewritten to simplify
    f_2 = (1/f_i2)^2;                 %Friction factor for discharge pipe [-]
end

%%Determine frictional head loss

h_f1 = ((4*f_1*l_1)/(2*g*D_1))*(v_1).^2;          %Frictional head loss in
suction pipe [m]
h_f2 = ((4*f_2*l_2)/(2*g*D_2))*(v_2).^2;          %Frictional head loss in
delilvery pipe [m]

%%Determine work to overcome friction in pipes

P_f1 = (2/3)*(((4*f_1*l_1)/(2*g*D_1))*(max(v_1))^2)*rho*g*Q       %Work
done to overcome inlet friction [W]
P_f2 = (2/3)*(((4*f_2*l_2)/(2*g*D_2))*(max(v_2))^2)*rho*g*Q       %Work
done to overcome discharge friction [W]
```

```
%%Determine pressure just before and just after the one-way valve

P_C2 = rho*g*((h_D-h_C)+(P_Dv/(rho*g)))      %Pressure just after one-way
valve [Pa]
P_C1 = rho*g*((h_B-h_C)+(P_Bv/(rho*g)))      %Pressure just before one-way
valve [Pa]

h_v = (((P_C1-P_C2))/(rho*g));                %Head loss over valve [m]

%Determine head delivered to pipe system%%

if P_A == 0                          %Use water level if suction valve is
open to determine head
    h_p = (h_D-h_0)+(P_D/(rho*g))+((rms(v_2).^2)/(2*g))+h_v
%Head delivered to pipe system [m]
else
    h_p = (h_D-h_A)+((P_D-P_A)/(rho*g))+((rms(v_2).^2-
rms(v_1)^2)/(2*g))+h_v    %Head delivered to pipe system [m]
end


h_in = h_p+h_i1+h_i2+h_f1+h_f2;
%Internal pressure of System [W]

P_h = rho*g*Q*(h_p) + P_f1 + P_f2
%Hydraulic power [W]


%%Fluid energy transfer ratio%%
eta_p = P_h/P_v

%%Plot fluid figures%%

%Instantanious head in bellow

figure
plot(t,h_in)
title('Instantanious pressure in bellow')
xlabel('Time [s]')
ylabel('Pressure [m]')
legend('Internal head of bellow')

%Fluid velocity ad acceleration

figure
subplot(2,1,1)
plot(t,v_1,'r',t,v_2,'g')
title('Fluid velocity')
xlabel('Time [s]')
ylabel('Velocity [m/s]')
legend('Velocity of suction fluid','Velocity of delivery fluid')
subplot(2,1,2)
plot(t,a_1,'r',t,a_2,'g')
title('Fluid acceleration')
xlabel('Time [s]')
ylabel('Acceleration [m/s^2]')
legend('Acceleration of suction fluid','Acceleration of delivery fluid')
```

```
%%create points for PV diagram

h_atm = P_atm/(rho*g);       %Atmospheric pressure [m]
h_as = max(h_i1);            %Fluid inertia for inlet pipe [m]
h_fs = max(h_f1);            %Friction head for inlet pipe [m]

if P_A == 0
    h_s = h_0 - h_A;         %Suction head [m]
else
    h_s = (P_A/(rho*g))+h_A %Suction head [m]
end

h_d = h_p-h_s;               %Delivery head [m]
h_ad = max(h_i2);            %Fluid inertia for discharge pipe [m]
h_fd = max(h_f2);            %Friction head for disharge pipe [m]


%%Set data points%%

vv1 = 0.005+0;
vv2 = 0.005+DeltaV/2;
vv3 = 0.005+DeltaV;
vv4 = 0.005+DeltaV;
vv5 = 0.005+DeltaV/2;
vv6 = 0.005+0;
vv7 = vv1;

%%Set matching head points%%

hh1 = h_atm+h_s-h_as;
hh2 = h_atm+h_s-h_fs;
hh3 = h_atm+h_s+h_as;
hh4 = h_atm+h_d+h_ad;
hh5 = h_atm+h_d+h_fd;
hh6 = h_atm+h_d-h_ad;
hh7 = hh1;

%%Array points created in table format for plotting%%

vvv = [vv1,vv2,vv3,vv4,vv5,vv6,vv7];
hhh = [hh1,hh2,hh3,hh4,hh5,hh6,hh7];
h_atmos = [h_atm,h_atm,h_atm];
h_suct = [h_atm+h_s,h_atm+h_s,h_atm+h_s];
h_deliver = [h_atm+h_d,h_atm+h_d,h_atm+h_d];

%Plot PV diagram

figure
plot(vvv(1:7),hhh(1:7),'go',vvv(1:7),hhh(1:7),'g',vvv(1:3),h_atmos(1:3),'b'
,vvv(1:3),h_suct(1:3),'r',vvv(1:3),h_deliver(1:3),'m')
title('PV diagram')
xlabel('Volume [m^2]')
ylabel('Pressure [m]')
legend('Data points','PV diagram','Atmospheric pressure','Suction
head','Delivery head')
```

B-6 Fluid energy transfer ratio

```
clear all

P_h = 7.6526;           %Hydraulic power [W]
P_v = 15.43;            %Vibration Power [W]

eta = P_h/P_v           %bellow fluid transfer ratio[-]
```